DTIC FILE COPY

AD-A955 376

DNA 4353F-1H-SAN

DSCS II COMMUNICATIONS LINK PERFORMANCE IN A MULTIBURST EUROPEAN SCENARIO

Document released under the Freedom of Information Act. FOI Case No. 86-88

F.W. Guigliano
C.L. Knepp
Mission Research Corporation
P.O. Drawer 719
Santa Barbara, California 93102

DTIC
ELECTE
FEB 0 8 1989
S D
D

31 December 1978

Final Report for Period 3 January 1978—31 December 1978

CONTRACT No. DNA 001-78-C-0049

THIS WORK SPONSORED BY THE DEFENSE NUCLEAR AGENCY UNDER RDT&E RMSS CODE B3630784464 O8BCAXBC-18403 H2590D.

DISTRIBUTION STATEMENT A
Approved for public release;
Distribution Unlimited

Prepared for
Director
DEFENSE NUCLEAR AGENCY
Washington, D. C. 20305

89 2 7 023

Best
Available
Copy

[redacted]

[redacted]

ADA955376

REPORT DOCUMENTATION PAGE		READ INSTRUCTIONS BEFORE COMPLETING FORM
1 REPORT NUMBER DNA 4353F-1H	2 GOVT ACCESSION NO.	3 RECIPIENT'S CATALOG NUMBER
4 TITLE (and Subtitle) DSCS II COMMUNICATIONS LINK PERFORMANCE IN A MULTIBURST EUROPEAN SCENARIO [redacted]		5 TYPE OF REPORT & PERIOD COVERED Final Report for Period 3 Jan 78—31 Dec 78
		6 PERFORMING ORG. REPORT NUMBER MRC-R-429 (IR-78-468)
7 AUTHOR(s) F. W. Guigliano D. L. Knepp		8 CONTRACT OR GRANT NUMBER(s) DNA 001-78-C-0049
9 PERFORMING ORGANIZATION NAME AND ADDRESS Mission Research Corporation P.O. Drawer 719 Santa Barbara, California 93102		10 PROGRAM ELEMENT, PROJECT, TASK AREA & WORK UNIT NUMBERS NWED Subtask 099QAXCA104-03
11 CONTROLLING OFFICE NAME AND ADDRESS Director Defense Nuclear Agency Washington, D.C. 20305		12 REPORT DATE 31 December 1978
		13 NUMBER OF PAGES 120
14 MONITORING AGENCY NAME & ADDRESS(if different from Controlling Office)		[redacted] SCHEDULE

16 DISTRIBUTION STATEMENT (of this Report)

17 DISTRIBUTION STATEMENT (of the abstract entered in Block 20, if different from Report)

18 SUPPLEMENTARY NOTES

This work sponsored by the Defense Nuclear Agency under RDT&E RMSS Code B363078464 099QAXCA10403 H2590D.

19 KEY WORDS (Continue on reverse side if necessary and identify by block number)

Defense Satellite Communications System
Multiburst Scenario
Signal Propagation
Signal Scintillation
Communications Receivers
European Communications Links

20 ABSTRACT (Continue on reverse side if necessary and identify by block number)

[redacted] A detailed study of the potential degradation of a military satellite communications link caused by the detonation of two, simultaneous high-altitude nuclear bursts is presented here. The two bursts, which are located in the Mediterranean region [redacted]

DNA (b)(3)

DD FORM 1 JAN 73 1473 EDITION OF 1 NOV 65 IS OBSOLETE

[redacted]

Document released under the Freedom of Information Act, DNA Case No. 86-88

[redacted]

[redacted]

[redacted]

[redacted]

20. ABSTRACT (Continued)

[redacted]

[redacted] Also presented here are comparisons between the detailed MICE/MELT phenomenology calculations and calculations from the fast-running SATL code which uses the RANC IV phenomenology models. Results clearly show the inadequacy of the RANC IV phenomenology models for the estimation of late-time scintillation effects on satellite communications links.

DTIC COPY INSPECTED

Accesion For	
NTIS CRA&I	☑
DTIC TAB	☐
Unannounced	☐
Justification	
By	
Distribution /	
Availability Codes	
Dist	Avail and / or Special
A-1	

UNANNOUNCED

[redacted]

[redacted]

[redacted]

[redacted]

[redacted] PREFACE

The authors would like to express their gratitude to Robert L. Bogusch, Fredric E. Fajen, Ralph W. Kilb, Robert W. Stagat and Willard W. White for advice and suggestions which have aided in the completion of this work.

[redacted]

[redacted]

[redacted]CONTENTS

PREFACE 1

ILLUSTRATIONS 3

TABLES 6

SECTION

1 INTRODUCTION 1-1

1.1 APPROACH 1-2

1.2 OUTLINE AND RESULTS 1-5

2 NUCLEAR ENVIRONMENT DESCRIPTION 2-1

2.1 BACKGROUND 2-1

2.2 NUCLEAR PHENOMENOLOGY CODES 2-4

2.2.1 MICE/MELT Phenomenology 2-4

2.2.2 RANC IV 2-7

2.3 DUAL-BURST EUROPEAN SCENARIO 2-8

3 PROPAGATION DISTURBANCES 3-1

3.1 MICE/MELT—RANC/SATL COMPARISON 3-1

3.2 MICE/MELT SCINTILLATION EFFECTS 3-19

3.2.1 Signal Structures 3-19

3.2.2 Spatial Extent and Fading Rates 3-29

4 LINK PERFORMANCE ANALYSIS 4-1

4.1 DSCS II AN/USC-28 MODEM SIMULATION 4-1

4.2 MODEM PERFORMANCE EXAMPLES 4-6

4.2.1 Example 1: Amplitude Dominated Situation 4-7

4.2.2 Example 2: Amplitude and Phase Both Important 4-17

4.3 LANDSTUHL LINK ANALYSIS 4-22

4.4 MODEM PERFORMANCE SUMMARY—SATURATED SCINTILLATION 4-25

REFERENCES R-1

[redacted]

ILLUSTRATIONS

FIGURE		PAGE
2-1.	Contours of N_e in magnetic meridian planes through the two plumes at a simulation time of 10 minutes (MICE/MELT results).	2-9
2-2.	Contours of N_e in magnetic meridian planes through the two plumes at a simulation time of 20 minutes (MICE/MELT results).	2-10
2-3.	Contours of N_e in magnetic meridian planes through the two plumes at a simulation time of 60 minutes (MICE/MELT results).	2-11
2-4.	Contours of N_e in horizontal planes at altitudes of 400 km and 800 km, at a simulation time of 60 minutes (MICE/MELT results).	2-13
2-5.	Contours of TEC on paths from the DSCS II Atlantic satellite to Europe at 10 minutes (MICE/MELT results).	2-14
2-6.	Contours of TEC on paths from the DSCS II Atlantic satellite to Europe at 20 minutes (MICE/MELT results).	2-15
2-7.	Contours of TEC on paths from the DSCS II Atlantic satellite to Europe at one hour (MICE/MELT results).	2-16
2-8.	Contours of ΔN_e in magnetic meridian planes through the two plumes at a simulation time of 10 minutes (MICE/MELT results).	2-18
2-9.	Contours of ΔN_e in magnetic meridian planes through the two plumes at a simulation time of 20 minutes (MICE/MELT results).	2-19
2-10.	Contours of ΔN_e in magnetic meridian planes through the two plumes at a simulation time of 60 minutes (MICE/MELT results).	2-20

FIGURE		PAGE
3-1.	Contours of phase standard deviation (σ_ϕ) for the MICE/MELT multiburst simulation at 10 minutes.	3-6
3-2.	Contours of phase standard deviation (σ_ϕ) based on RANC phenomenology models at 10 minutes.	3-7
3-3.	Contours of phase standard deviation (σ_ϕ) for the MICE/MELT multiburst simulation at 20 minutes.	3-10
3-4.	Contours of phase standard deviation (σ_ϕ) based on RANC phenomenology models at 20 minutes.	3-11
3-5.	Contours of phase standard deviation (σ_ϕ) for the MICE/MELT multiburst simulation at 30 minutes.	3-14
3-6.	Contours of phase standard deviation (σ_ϕ) based on RANC phenomenology models at 30 minutes.	3-15
3-7.	Contours of phase standard deviation (σ_ϕ) for the MICE/MELT multiburst simulation at one hour.	3-16
3-8.	Contours of phase standard deviation (σ_ϕ) based on phenomenology models at one hour.	3-17
3-9.	Signal amplitude and phase at Landstuhl at 10 minutes.	3-22
3-10.	Signal amplitude and phase at Landstuhl at 20 minutes.	3-23
3-11.	Signal amplitude and phase at Landstuhl at 30 minutes.	3-24
3-12.	Signal amplitude and phase at Landstuhl at one hour.	3-25
3-13.	Signal amplitude and phase for intense, Rayleigh scintillation.	3-30
3-14.	Extent of intense, Rayleigh scintillation and contours of correlation time at 20 minutes.	3-32
3-15.	Extent of intense, Rayleigh scintillation and contours of correlation time at 30 minutes.	3-33
3-16.	Extent of intense, Rayleigh scintillation and contours of correlation time at one hour.	3-34
3-17.	Signal correlation length versus phase standard deviation.	3-36
3-18.	Extent of intense Rayleigh scintillation and contours of correlation time at one hour for a fully striated plume.	3-38
4-1.	Functional diagram of the AN/USC-28 BPSK demodulator with modified Costas phase-lock loop.	4-3
4-2.	Example 1: Signal amplitude versus time, $\tau_0 = 1.0$ sec.	4-8
4-3.	Example 1: Signal phase versus time, $\tau_0 = 1.0$ sec.	4-9

FIGURE		PAGE
4-4.	Example 1: Phase tracking error history, $C/N_0 = 45$ dB-Hz, $\tau_0 = 1.0$ sec.	4-11
4-5	Example 1: Conditional binary error time history, $C/N_0 = 45$ dB-Hz, $\tau_0 = 1.0$ sec.	4-12
4-6.	Example 1: Frequency tracking error time history, $C/N_0 = 45$ dB-Hz, $\tau_0 = 1.0$ sec.	4-14
4-7.	Example 1: AGC gain versus time, $C/N_0 = 45$ dB-Hz, $\tau_0 = 1.0$ sec.	4-16
4-8.	Example 1: Simulated received message for AN/USC-28 modem, $\tau_0 = 1.0$ sec, $C/N_0 = 45$ dB-Hz.	4-17
4-9.	Example 2: phase tracking error history, $C/N_0 = 45$ dB-Hz, $\tau_0 = 0.1$ sec.	4-19
4-10.	Example 2: Frequency tracking error time history, $C/N_0 = 45$ dB-Hz, $\tau_0 = 0.1$ sec.	4-20
4-11.	Example 2: AGC gain versus time, $C/N_0 = 45$ dB-Hz, $\tau_0 = 0.1$ sec.	4-21
4-12.	Example 2: Simulated received message for AN/USC-28 modem, $\tau_0 = 0.1$ sec, $C/N_0 = 45$ dB-Hz.	4-22
4-13.	Landstuhl link: Average binary error probability versus mean C/N_0 and mean E_b/N_0.	4-23
4-14.	Rayleigh fading links: Average binary error probability versus mean C/N_0 and mean E_b/N_0.	4-27
4-15.	Contours of binary error rate at 20 minutes. Dashed contour shows Rayleigh footprint.	4-30
4-16.	Contours of binary error rate at 30 minutes. Dashed contour shows Rayleigh footprint.	4-31
4-17.	Contours of binary error rate at one hour. Dashed contour shows Rayleigh footprint.	4-32
4-18.	Contours of binary error rate at one hour for a fully striated plume. Dashed contour shows Rayleigh footprint.	4-33

TABLES

TABLE		PAGE
3-1	Summ[illegible] of [illegible] [illegible] [illegible]r the Landstuhl link.	3-27
4-1	AN/USC-28 mode[illegible] [illegible]ign parameters.	4-6
4-2	Hypothetical link calculation.	4-34

[redacted]SECTION 1
INTRODUCTION

A detailed study of the potential degradation of a military satellite communications link caused by the detonation of two, simultaneous high-altitude nuclear bursts is presented here. [redacted]

DNA (b)(1)

Detailed demodulation performance results are presented in the form of binary error rate plots, binary error rate contours, and examples of demodulator performance and received demodulated messages.

Also presented here are comparisons between the detailed MICE/MELT phenomenology calculations and calculations from the fast-running SATL code which uses the RANC IV phenomenology models. This comparison is presented in terms of the phase standard deviation (σ_ϕ) which provides a measure of the intensity of the ionization structure on various propagation paths. Results clearly show the inadequacy of the RANC IV phenomenology models for the estimation of late-time scintillation effects on satellite communication links.

The remainder of this section discusses the approach taken in performing this work and summarizes the most important results.

[redacted]

1.1 APPROACH

The goals of this work are twofold; (1) to perform a detailed link analysis in a specified multiburst nuclear scenario; and (2) to compare detailed phenomenology calculations with results from simplified RANC IV models in terms of their impact on link assessments. To accomplish the first goal we have utilized detailed numerical simulations in three key areas. First, the descriptions of the nuclear environment used here are obtained from large magnetohydrodynamic computer simulations of nuclear weapons phenomenology, including effects of plasma instabilities that lead to striation formation. Second, signal propagation disturbances, in particular signal scintillation caused by striated ionization, are calculated using detailed numerical propagation techniques. Third, analyses of modem performance are carried out with realistic digital simulations of the operation of critical receiver functions.

The first step is the description of the nuclear propagation environment in terms of disturbances to the propagation medium. This step is fundamental to the analyses of propagation effects on communications systems. In this analysis, results of a recent, detailed simulation of a dual-burst scenario provide the propagation environment directly. These phenomenology simulations are the results of ongoing work (References 1-1 to 1-9) under the sponsorship of the Defense Nuclear Agency (DNA). Such calculations involve the use of large numerical simulations of the physical and chemical processes that control the formation and evolution of ionization produced by nuclear detonations. Included in these calculations are radiation transport and energy deposition, two-fluid (ions and neutrals) magnetohydrodynamics (MHD), atmospheric chemistry, and plasma instability mechanisms. Section 2 provides a brief summary of the phenomenology codes used for this work and also summarizes the major features of the dual-burst scenario relevant to communications degradation.

The second step is the calculation of the effects of the nuclear environment on signal propagation in order to predict overall regions subject to potential degradation, as well as to obtain representations of the received signal structure at various locations in the degraded regions. To obtain boundaries for degradation, line integrals of certain important quantities (such as absorption, total electron content, and phase standard deviation) are obtained along many propagation paths through the nuclear environment. This type of calculation provides estimates of the spatial extent of significant levels of propagation disturbances. The time evolution of these disturbances is obtained by performing such calculations for various times after the detonations. To obtain received signal structures, a numerical multiple phase screen (MPS) technique is used (References 1-10 and 1-11). Input to the MPS simulation includes the link geometry and ionization location determined from the phenomenology simulation. Outputs of the MPS calculations provide detailed prediction of the signal amplitude and phase caused by nuclear induced electron-density fluctuations (striations). This type of calculation is extemely useful since uncertainties in the nuclear environment description can be handled parametrically. The MPS propagation results for received signal amplitude and phase are used as direct input to the receiver simulation model.

The third step in the analysis is the application of a detailed numerical simulation model of the DSCS II AN/USC-28 PSK receiver. This simulation model is a sampled-data digital implementation of critical receiver elements, including phase-lock loops, automatic gain control (AGC) circuits, coherent data demodulation, differential decoding, and data output. This digital simulation approach is the only practical method of correctly treating the nonlinearities inherent in coherent PSK demodulators. For example, the phase-lock loop (PLL), which is the heart of the AN/USC-28 demodulator, can be described mathematically by a nonlinear stochastic integro-differential equation. This equation can be solved by analytical techniques for only a very few limiting situations. However, the nonlinear

operation of the PLL can be quite accurately represented by straightforward finite difference techniques. Similarly, the nonlinear operation of the AGC and other receiver elements can be readily simulated numerically. Furthermore, the simulation model is applicable to all types of propagation disturbances and places no restrictions on the statistical or deterministic properties of received signal amplitude and phase.

The AN/USC-28 modem simulation used in this analysis is based on material obtained from References 1-12 to 1-15 and is taken from a general PSK simulation model applicable to a number of other DSCS II PSK modems. The interested reader is referred to Reference 1-16 for a complete description of the general coherent PSK modem simulation.

The use of multiple phase screen (MPS) signal structures as direct input to the receiver simulation has two major advantages. First, since all nonlinear functions of the receiver are correctly modeled, the results are quite general. This is in contrast to common analytical treatments where either perfect phase tracking or perfect AGC operation is assumed. Second, the simulation process itself is remarkably efficient in terms of computer time. Thus a large number of simulations can efficiently be made to obtain statistically reliable results or to investigate receiver design modifications.

The second major goal of this work is to assess the importance of differences between phenomenology calculations and simplified models on the link performance results. This assessment takes the form of a comparison of an important propagation parameter (rms phase fluctuations, σ_ϕ) obtained from the detailed MICE/MELT simulation versus contours supplied by Dr. James Marshall (Reference 1-17) from the ESL SATL code. Although not

* SATL utilizes the RANC IV high altitude phenomenology package with a few modifications.

a direct measure of scintillation, these σ_ϕ contours show the extent and severity of the disturbance on various propagation paths and thus are useful for comparing phenomenology calculations from the satellite communications standpoint. In addition to this direct comparison of phenomenology calculations with models for a particular scenario, we have also summarized important features of the RANC IV code and of the MICE/MELT code as they relate to satellite communications studies.

1.2 OUTLINE AND RESULTS

Section 2 of this report describes important features of the dual-burst European scenario which impact satellite communications calculations. Emphasis is placed on the motion and development of the high altitude plume which is found to be poorly modeled by the RANC IV code.

Section 3 presents a comparison between the detailed MICE/MELT phenomenology calculations and calculations from the SATL code which utilizes the RANC IV phenomenology models. It is shown that major differences exist in predictions of propagation disturbances between the detailed calculations and the RANC IV predictions. Substantial differences are noted in the extent, location, and severity of scintillation effects as a function of time in this scenario. These differences are due to inadequacies in several aspects of the RANC IV phenomenology model:

1. Plume modeling. The RANC model is clearly inadequate to represent the late time, field-aligned ionization plume produced by a high-altitude, large yield nuclear detonation, and was, in fact, never intended for this purpose. The late time plume geometry is not modeled in the RANC phenomenology code. Late time nuclear effects, however, are very important to strategic satellite communication systems.

2. Fireball and plume motion. The RANC modeling of fireball expansion and rise across the magnetic field yields results substantially different from the detailed MICE/MELT simulation.

Thus the two calculations predict different locations for the regions of propagation disturbances. Late time motion of the ionized plume is not included in the RANC phenomenology package. This omission is important for the multiburst scenario studied since gravitational forces acting on the late-time high altitude plume cause substantial southward drift of the regions of propagation disturbances.

3. Striation Modeling. Striation formation in the RANC model also differs substantially from the results of the plasma stability analysis in the MICE/MELT simulation. The striation onset time in the RANC model does not agree with the MICE/MELT linear analysis for this case, resulting in predictions of significantly more severe scintillation effects by RANC/SATL at early times. At late times, the striations are confined to the original RANC fireball location, thus the extent and location of disturbed propagation regions is different than predicted by MICE/MELT.

Propagation calculations presented in Section 3 graphically show the extent and severity of the disturbed regions superimposed on a map of Europe. At one hour after the detonation, the region of severe Rayleigh amplitude fading encompasses most of the Mediterranean sea, and all or parts of thirteen countries including Spain, France, West Germany, Italy and Greece. We have found that within this severe Rayleigh fading region the signal correlation time (which is a measure of the fading rate) serves as an excellent parameter to specify the receiver performance. For this reason we show in Section 3 contour plots of the signal correlation time within the Rayleigh fading region.

[redacted]

Section 4 describes the AN/USC-28 simulation and shows detailed examples of the modem operation at a 75 bps data rate. Results are shown for the input signal amplitude and phase, phase and frequency tracking performance, AGC response, and demodulated received messages. More general results are presented for average binary error rate as a function of signal correlation time and mean bit energy-to-noise density ratio. These results may be combined with contour plots shown in Section 3 to obtain bit error rates for any desired terminal location within the Rayleigh fading region. One such example is shown and contour plots of average binary error probability are obtained for a link involving large, fixed uplink and downlink terminals.

[redacted]

[redacted]

[redacted]

[redacted]

DCA (b)(1)

[redacted]

[redacted]

[redacted] SECTION 2
NUCLEAR ENVIRONMENT DESCRIPTION [redacted]

This section contains a general discussion of the nuclear environment and its effects on satellite communications. Techniques currently used to calculate nuclear phenomena of concern for satellite propagation are reviewed. The MICE/MELT phenomenology simulation and RANC phenomenology models are discussed briefly. The results of the MICE/MELT simulation for the dual-burst scenario are then summarized. [redacted]

2.1 [redacted] BACKGROUND [redacted]

[redacted] Ionized plasma caused by nuclear detonations can produce a variety of disturbances to radio signal propagation. These disturbances include attenuation, phase shift, time delay, dispersion, polarization rotation, refraction, multipath, and increased noise levels. In addition, relatively small-scale inhomogeneities in the propagation medium can cause signal scintillation — random fluctuations in received signal amplitude and phase.

[redacted] The severity of these various signal propagation disturbances depends on the magnitude of the electron concentration and the degree to which it is structured. The severity of propagation disturbances is also a strong function of radio wave frequency. Generally, the higher the frequency, the less severe the signal disturbance for a given level of ionospheric disturbance. UHF satellite signals can be significantly affected by naturally-occurring disturbances in the ambient ionosphere, particularly

[redacted]

[redacted]

in the equatorial and auroral regions where strong UHF scintillations are recorded rather frequently. Higher-frequency signals in the SHF band are much less affected by natural disturbances although moderate levels of SHF scintillation are occasionally recorded. When ionospheric disturbances are much more intense than occur naturally, signals in all satellite frequency bands are subject to potentially severe degradation if the links penetrate the disturbed regions of the ionosphere.

[redacted] The most important environmental properties affecting signal propagation at DSCS frequencies are the electron concentration and spatial irregularities in the electron concentration. Nuclear detonations produce greatly increased levels of ionization due to deposition of much of the radiated energy in the atmosphere. The spatial extent, location, and duration of the ionization are sensitive functions of detonation altitude and also depend on weapon yield and other characteristics. At relatively low detonation altitudes, below about 50 km, much of the weapon energy is deposited initially in a fairly localized region around the burst, producing an intensely ionized fireball. At high detonation altitudes, above about 100 km, the weapon energy is deposited in a much larger volume producing less intense but longer-lasting ionization in a widespread region of the ionosphere. Such high altitude detonations can also cause the electron concentration to become structured, or striated, throughout large regions that extend to extremely high altitudes. The striation structure resembles filaments of high electron content aligned with the geomagnetic field.

[redacted] The average electron concentration affects the values of mean propagation disturbances. Absorption (in decibels) is proportional to the integral of the product of electron density and electron collision frequency along the propagation path. Thermal noise is dependent on the levels of absorption inside and outside hot ionized regions, and therefore is a function of electron density and temperature. Phase shift, group delay,

[redacted]

[redacted]

and dispersion are proportional to the integrated electron content along the propagation path, and refraction is dependent on the component of the gradient of electron content normal to the propagation path.

[redacted] The small scale electron density fluctuations (striations) cause scattering of radio waves propagating through the ionized medium. This scattering results in scintillation in received signal amplitude, phase, angle-of-arrival, and group delay.

[redacted] The existence of signal propagation disturbances in a nuclear environment, and the responsible environmental disturbances, have been well known for over two decades. Much information concerning nuclear weapons phenomenology has been obtained from nuclear tests, especially from the 1958 Teak and Orange high-altitude tests and the five high-altitude events of the 1962 Fishbowl series. Experimental data collected during these and other nuclear tests have been extensively and intensively analyzed. [redacted]

[redacted]

DNA (b)(3)

[redacted] Consequently, most of our quantitative information about high-altitude nuclear phenomenology, and especially striation phenomenology comes from "detailed nuclear phenomenology" calculations. Such calculations

[redacted]

involve the solution of large sets of coupled equations derived from the principles of mass, momentum and energy conservation. "Detailed" signifies that all of the physical and chemical processes relevant to high altitude bursts are included and are computed from fundamental equations rather than models (see, for example, References 2-3 through 2-10). Subject only to practical limitations imposed by computer size and speed, these phenomenology simulations provide the most accurate and detailed descriptions of the nuclear environment yet devised.

2.2 [redacted] NUCLEAR PHENOMENOLOGY CODES

The following two subsections summarize the most important features of the MICE/MELT phenomenology simulation and RANC model as they describe particular aspects of the propagation environment relevant to satellite communication systems studies. The MICE/MELT simulation calculates nuclear phenomenology from basic principles of mass, momentum, and energy conservation. The RANC model uses empirically derived scaling laws to estimate the nuclear environment. Section 3 discusses the most important differences in the two phenomenology calculations from the point of view of propagation effects on satellite communications for the dual-burst scenario.

2.2.1 MICE/MELT Phenomenology

For detonations at altitudes above 200 km, nuclear phenomenology can be treated in three time regimes: (1) early time (less than one second) characterized by fireball formation and initial deposition of the burst energy into the atmosphere; (2) late time (one second to about 5-10 minutes) characterized by strong magnetohydrodynamic (MHD) shocks and by subsequent relaxation of the magnetic field to near ambient; (3) very late time (greater than 5-10 minutes) characterized by striation formation and plasma streaming along magnetic field lines to the conjugate region.

Each time region is handled by a different code. The CMHD code (Reference 2-11) simulates the early time phenomena and determines the X-ray, UV, and debris patch depositions used to initiate the MICE code, which then handles the late time phenomenology.

MICE is a general two-fluid magnetohydrodynamics (MHD) code which treats both burst-produced and naturally occurring ionization as an MHD fluid which is coupled to the geomagnetic field, and the neutral air as another fluid, coupled to the first fluid by collisions. A three dimensional geometry is used to properly account for the earth's curvature, and the ambient geomagnetic field is approximated by a geocentric dipole. The MICE code utilizes large sets of finite difference equations to properly treat all the physical and chemical processes relevant to high altitude bursts. These processes include propagation of strong hydrodynamic and magnetohydrodynamic (MHD) shocks through the atmosphere, and buoyant and ballistic rising of heated and ionized regions (fireballs, debris patch regions). MICE is designed to treat strong shocks and high density plasma that produce substantial geomagnetic field distortions.

In principle, the physics incorporated in MICE is adequate to essentially describe all the expected phenomenology at times greater than about one second after detonation, including, for example, elongation of the burst-produced plasma parallel to the earth's magnetic field, and the development of fine-scale structure (striations). In practice, however, because of the limited spatial resolution (imposed by computer running time and storage constraints), a different approach is adopted for the very late time problem.

The MELT code is used to continue the simulation at very late times, when magnetic disturbances have dissipated and the magnetic field can reasonably be assumed to be ambient. The MELT code, because of the ambient geomagnetic field assumption, can calculate very late time field-aligned

ionization motion over a larger spatial volume than would be practical with the MICE code. The geomagnetic field is approximated by a geocentric dipole in MELT, as in the MICE code, and deionization chemistry is treated in a similar manner in both codes.

The MELT phase of the simulation is characterized by plasma streaming along the magnetic field lines to high altitudes. Plasma motion is determined by a complex system of electrical currents induced by gravity, bomb produced and ambient winds, coriolis and other forces. The MELT code tracks plasma motion from the burst region all the way to the magnetic conjugate region and thereby provides nuclear environment descriptions over the extended volumes required for communication systems applications.

The MICE and MELT codes contain all of the basic physics required to compute striation growth. However, because of the large extent of ionization produced by high altitude nuclear detonations, it is not practical with current computer technology to compute effects on a scale fine enough to directly calculate striation formation over the spatial volume of interest. The MELT code therefore calculates striation growth based on linearized field-line averaged plasma stability theory (Reference 2-12). This approach uses a perturbation analysis which incorporates Rayleigh-Taylor, gradient drift, and field-line curvature instability mechanisms, with ion diffusion and viscosity effects to calculate striation growth and decay. The principal result of the analysis is the spatial and temporal description of the electron density fluctuation ($\Delta N_e(x,t)$). A limitation of the theory is that it requires knowledge of the initial electron density fluctuation level ($\Delta N_e(x,t_o)$), which remains as one of the uncertainties in the analysis. Current estimates of the initial fluctuation level range from about 0.1 percent to 1.0 percent. A value of 1.0 percent was used in the MICE/MELT calculation discussed in this report.

[redacted]

2.2.2 RANC IV

According to Reference 2-13:

> "The RANC code is a digital computer program that provides rapid estimates of the effects of a multi-burst nuclear environment on radar propagation."...
> "The code does not include detailed numerical treatment of radiation transport, debris/air coupling, hydrodynamics, MHD, multispecies chemical kinetics, and so on. Other computer programs are available for these purposes; they often contribute to the basis for the simpler RANC models."

The basic approach in the RANC code is to utilize simple phenomenology scaling laws (based on nuclear observations, theory, and more detailed nuclear simulations) in order to achieve the goal quoted above. The primary emphasis in its development was an analysis of ballistic missile defense radar performance. The long history of this code and the large number of users of the RANC model testify to its adequacy in this application. However, adequacy in the solution of the early time radar problem should not be taken to imply adequate treatment of very late time nuclear phenomenology important to satellite communications.

A complete description of the RANC code phenomenology package is contained in Reference 2-13. In brief, simple geometrical shapes are used to model the shape of the high altitude fireball region (sphere, prolate or oblate spheroid). These simple shapes may be altered by truncation planes which cut off the bottom of the fireball region. For high altitude bursts the fireball center rises ballistically until the fireball is trapped by the geomagnetic field, whereupon the fireball center location stays

[redacted]

[redacted]

constant. After magnetic containment the fireball radius perpendicular to the magnetic field stays constant and the fireball may only expand parallel to the magnetic field. The magnetic field direction is assumed constant (magnetic field lines are assumed straight) determined by the local dip angle at the initial burst location. Simple physical models and empirical data are used to estimate properties within the fireball region. Aspects of the models of particular relevance to the comparison of MELT and RANC/SATL results in the dual-burst scenario are discussed further in Section 3.

2.3 [redacted] DUAL-BURST EUROPEAN SCENARIO [redacted]

[redacted] This section summarizes the major MICE/MELT phenomenology simulation results for the dual-burst European scenario (see Reference 2-14 for a more detailed discussion of the nuclear phenomenology of this scenario).

[redacted]

DNA (b)(3)

[redacted] Figures 2-1 to 2-3 show contour plots of the mean electron density $\langle N_e \rangle$ on the scale of the northern magnetic hemisphere at times of 10, 20 and 60 minutes after detonation. Cross-sectional views of the electron density are shown in a magnetic meridian plane drawn through the current center of each plume. Since the plumes have moved since detonation, their centers no longer coincide with the initial burst locations. Electron concentration can be seen to range one to two orders of magnitude higher than

[redacted]

[redacted]

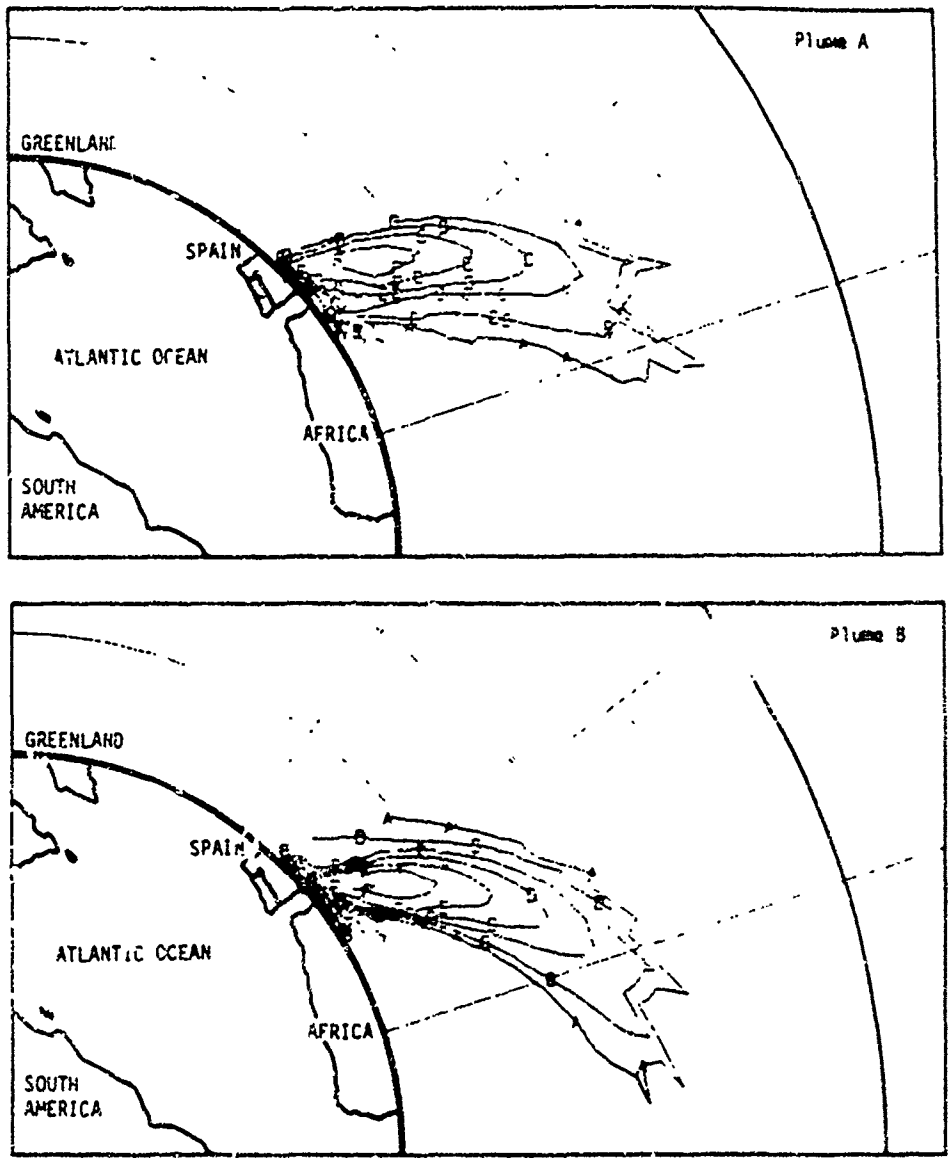

$A = 10^4\ cm^{-3}$, $B = 10^5\ cm^{-3}$, $C = 10^6\ cm^{-3}$, $D = 3 \times 10^6\ cm^{-3}$
$E = 10^7\ cm^{-3}$, $F = 3 \times 10^7\ cm^{-3}$, $G = 10^8\ cm^{-3}$

Figure 2-1. Contours of N_e in magnetic meridian planes through the two plumes at a simulation time of 10 minutes (MICE/MELT results).

[redacted]

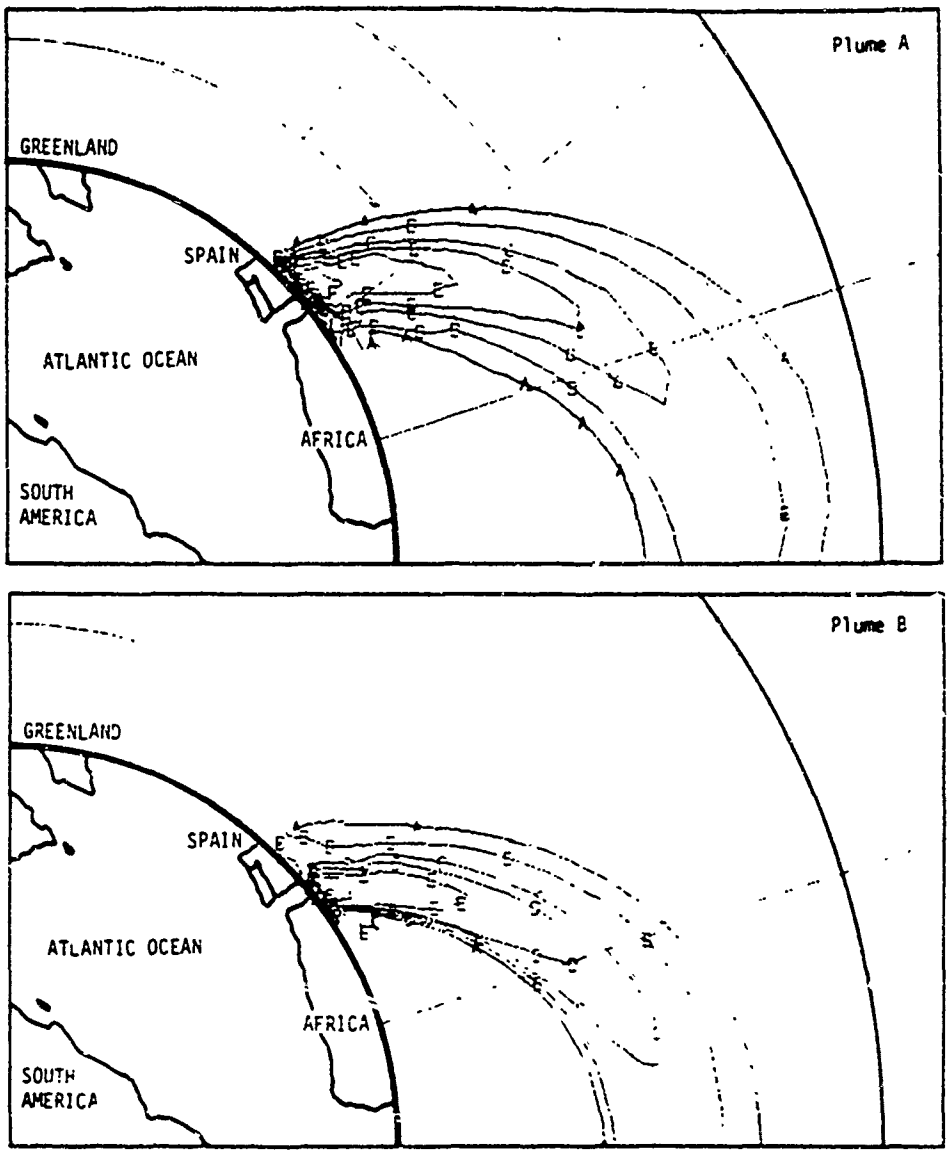

$A = 10^4\ cm^{-3}$, $B = 10^5\ cm^{-3}$, $C = 10^6\ cm^{-3}$, $D = 3 \times 10^6\ cm^{-3}$
$E = 10^7\ cm^{-3}$, $F = 3 \times 10^7\ cm^{-3}$, $G = 10^8\ cm^{-3}$

Figure 2-2. Contours of N_e in magnetic meridian planes through the two plumes at a simulation time of 20 minutes (MICE/MELT results).

[redacted]

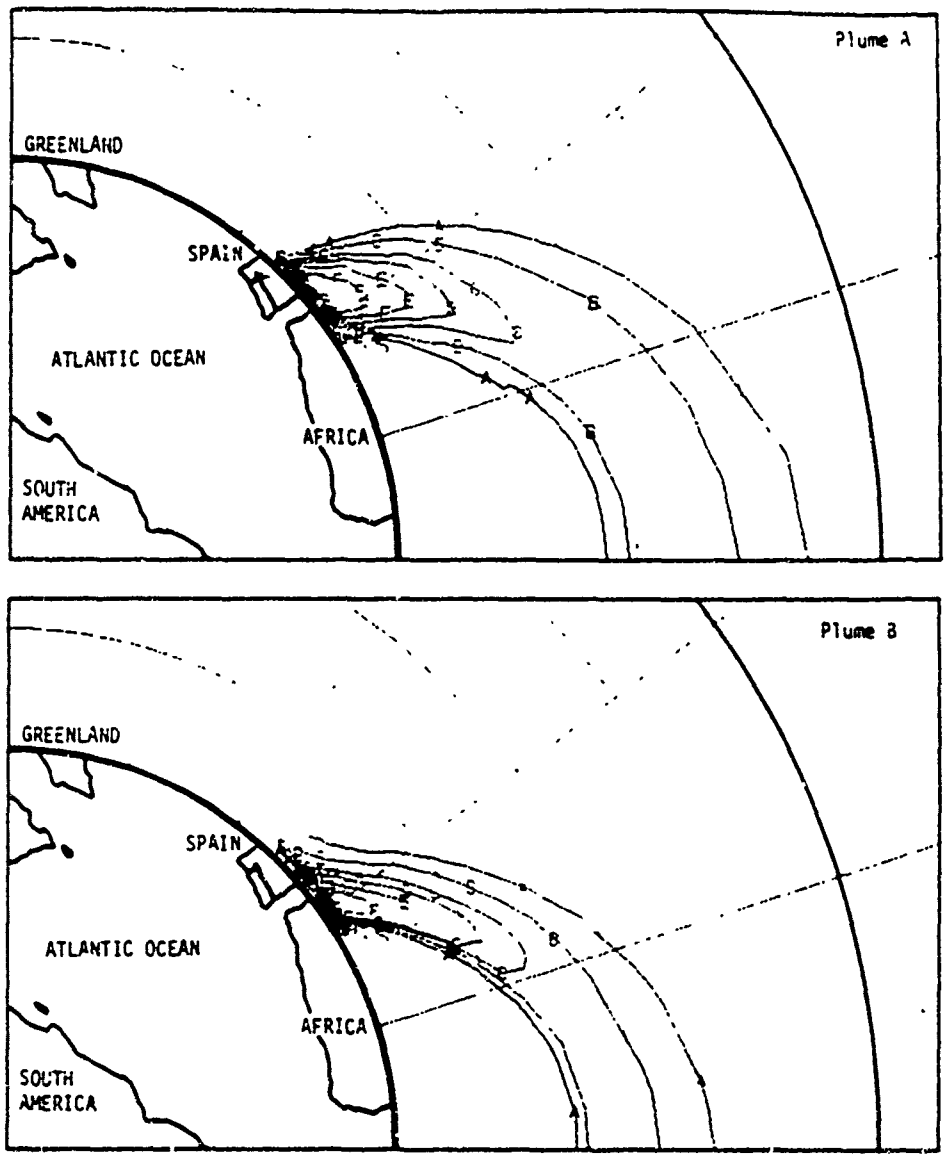

$A = 10^4\ cm^{-3}$, $B = 10^5\ cm^{-3}$, $C = 10^6\ cm^{-3}$, $D = 3 \times 10^6\ cm^{-3}$
$E = 10^7\ cm^{-3}$, $F = 3 \times 10^7\ cm^{-3}$, $G = 10^8\ cm^{-3}$

Figure 2-3. Contours of N_e in magnetic meridian planes through the two plumes at a simulation time of 60 mintes (MICE/MELT results).

[redacted]

ambient over large regions. Also shown is the upward and southward expansions of the plumes along the geomagnetic field lines. By 20 minutes the plasma has already crossed the geographic equator (the bottom boundary of Figures 2-1 to 2-3) reaching an altitude of nearly 7000 km with a thickness of almost 3000 km as shown by the 10^4 cm^{-3} electron density contour of Figure 2-2 (top). Although not visible on plots of this scale, beginning at about 20 minutes, ionization levels at about 750 kilometers altitude are increasing somewhat as the ions fall back down the magnetic field lines, reaching concentrations of up to 10^8 cm^{-3}. A comparison of the location of the 10^5 cm^{-3} electron density contour in the three figures shows that gravity causes a settling of the ionization and thus a southward drift of the plumes as a whole.

[redacted] This southward drift is also shown in Figure 2-4 which presents contours of mean electron density in horizontal planes whose altitudes (at the center of the plot) are 400 and 800 kilometers. The initial burst locations are indicated by asterisks on the plot. At 1 hour after detonation, the 400 km altitude contour on Figure 2-4 indicates that both plumes have moved about 500 km to the south.

[redacted] Figures 2-5 to 2-7 give another view of the size of the region of enhanced electron density. These figures show total electron content (TEC) obtained by integrating the electron density from the DSCS Atlantic satellite to various points in Europe. Contours are then drawn to enclose all regions where the TEC is greater than the contoured value. The effects of the southward movement of the ionization can be seen by comparison of the 10^{15} el/cm^2 contours (C contour) in all three figures. Large regions of TEC one to two orders of magnitude greater than usually obtained in the ambient ionosphere are apparent in all three figures.

[redacted]

[redacted]

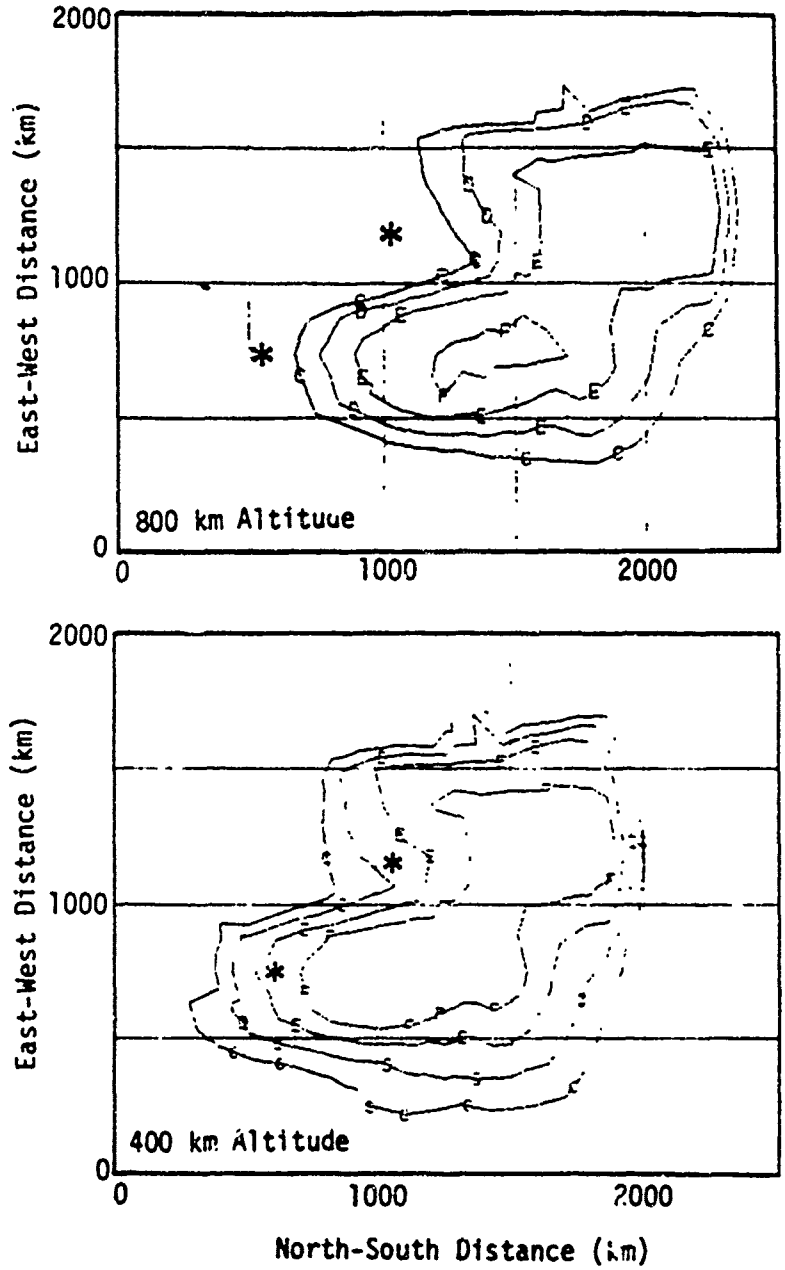

$C = 10^6\ cm^{-3}$, $D = 3 \times 10^6\ cm^{-3}$, $E = 10^7\ cm^{-3}$, $F = 3 \times 10^7\ cm^{-3}$

Figure 2-4. Contours of N_e in horizontal planes at altitudes of 400 km and 800 km, at a simulation time of 60 minutes (MICE/MELT results).

[redacted]

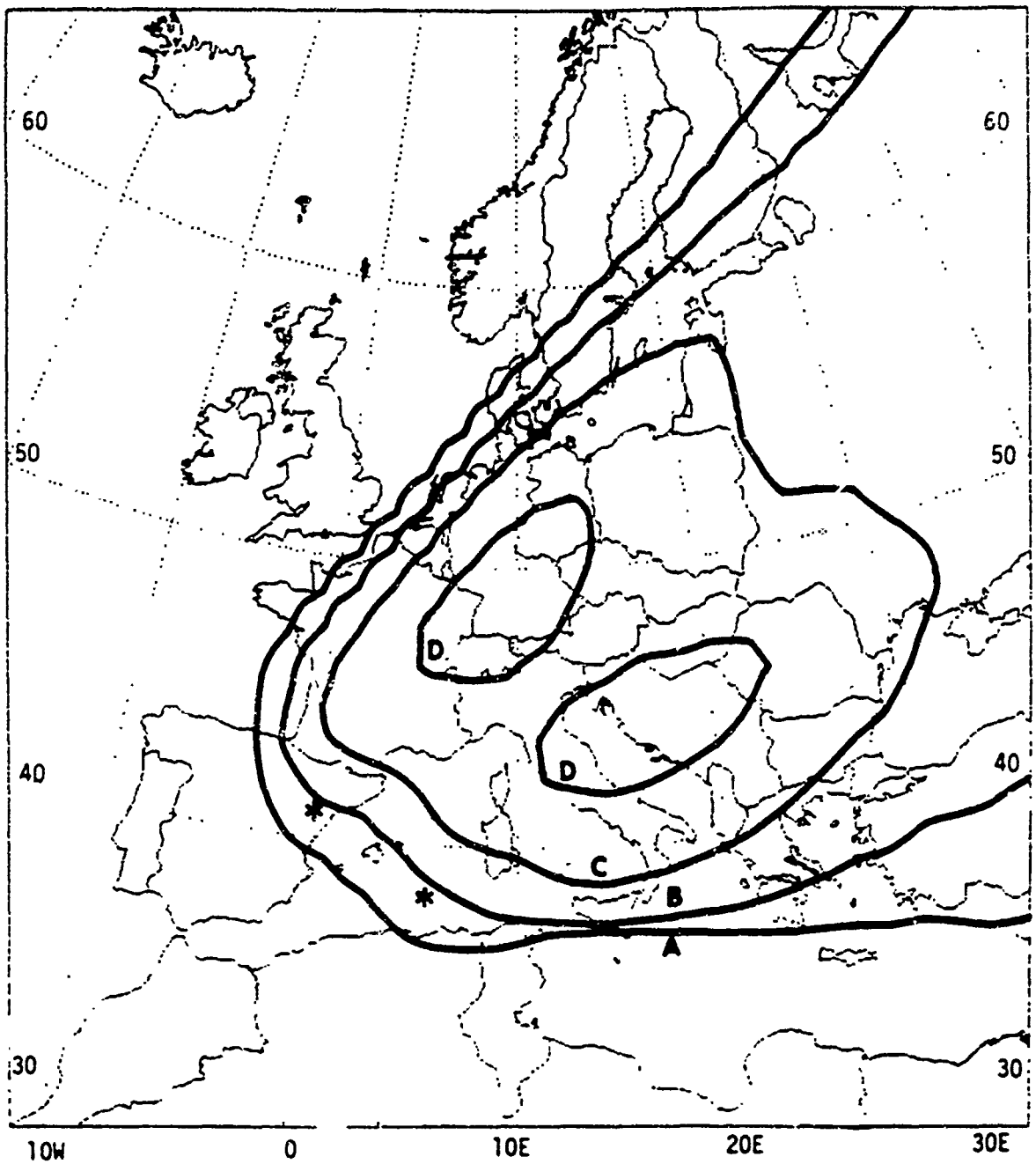

Contour values: A = $10^{14}cm^{-2}$, B = $3 \times 10^{14}cm^{-2}$, C = $10^{15}cm^{-2}$, D = $3 \times 10^{15}cm^{-2}$.

Figure 2-5. Contours of TEC on paths from the DSCS II Atlantic satellite to Europe at 10 minutes (MICE/MELT results).

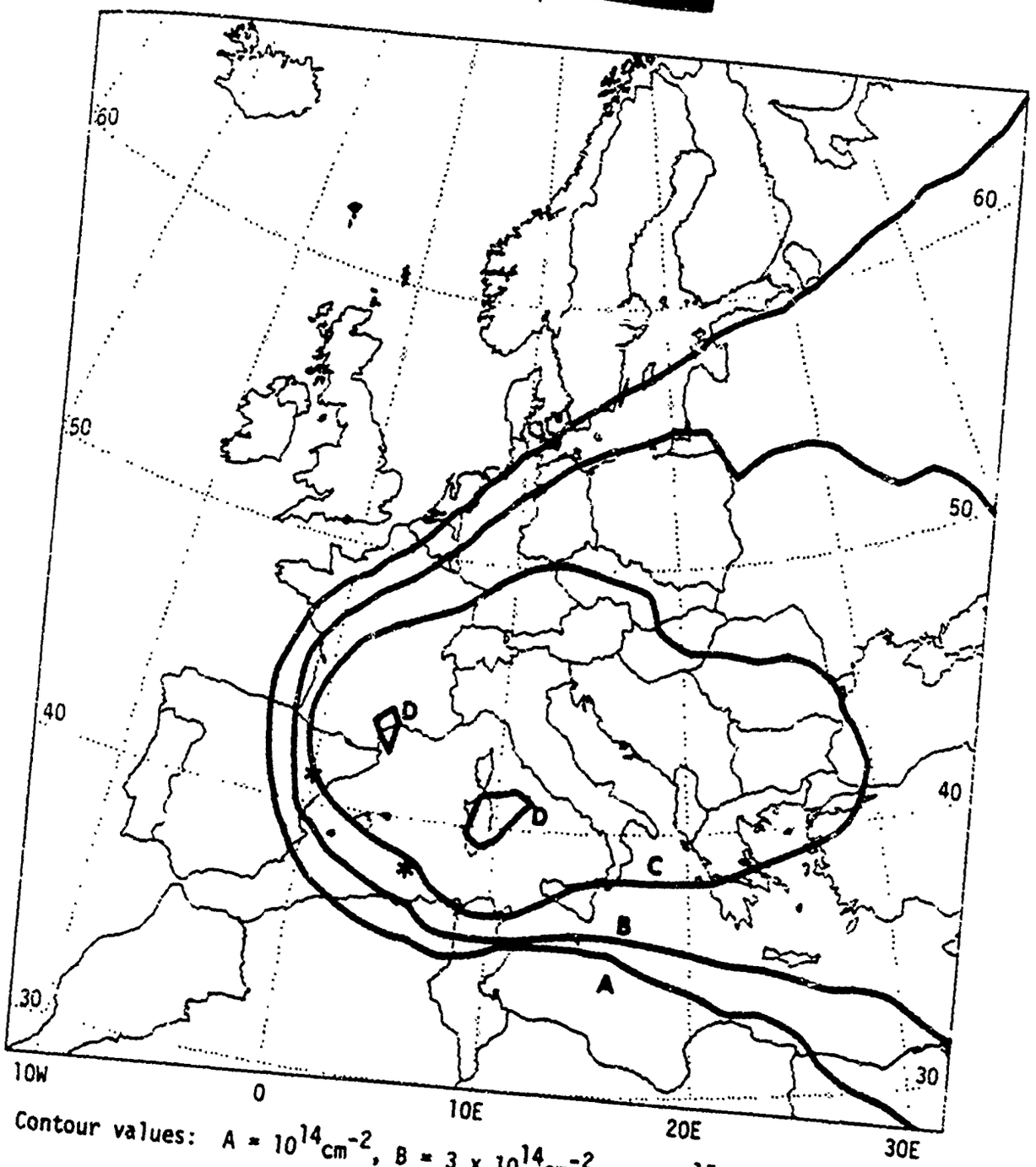

Contour values: A = $10^{14}cm^{-2}$, B = $3 \times 10^{14}cm^{-2}$, C = $10^{15}cm^{-2}$, D = $3 \times 10^{15}cm^{-2}$.

Figure 2-6. Contours of TEC on paths from the DSCS II Atlantic satellite to Europe at 20 minutes (MICE/MELT results).

[redacted]

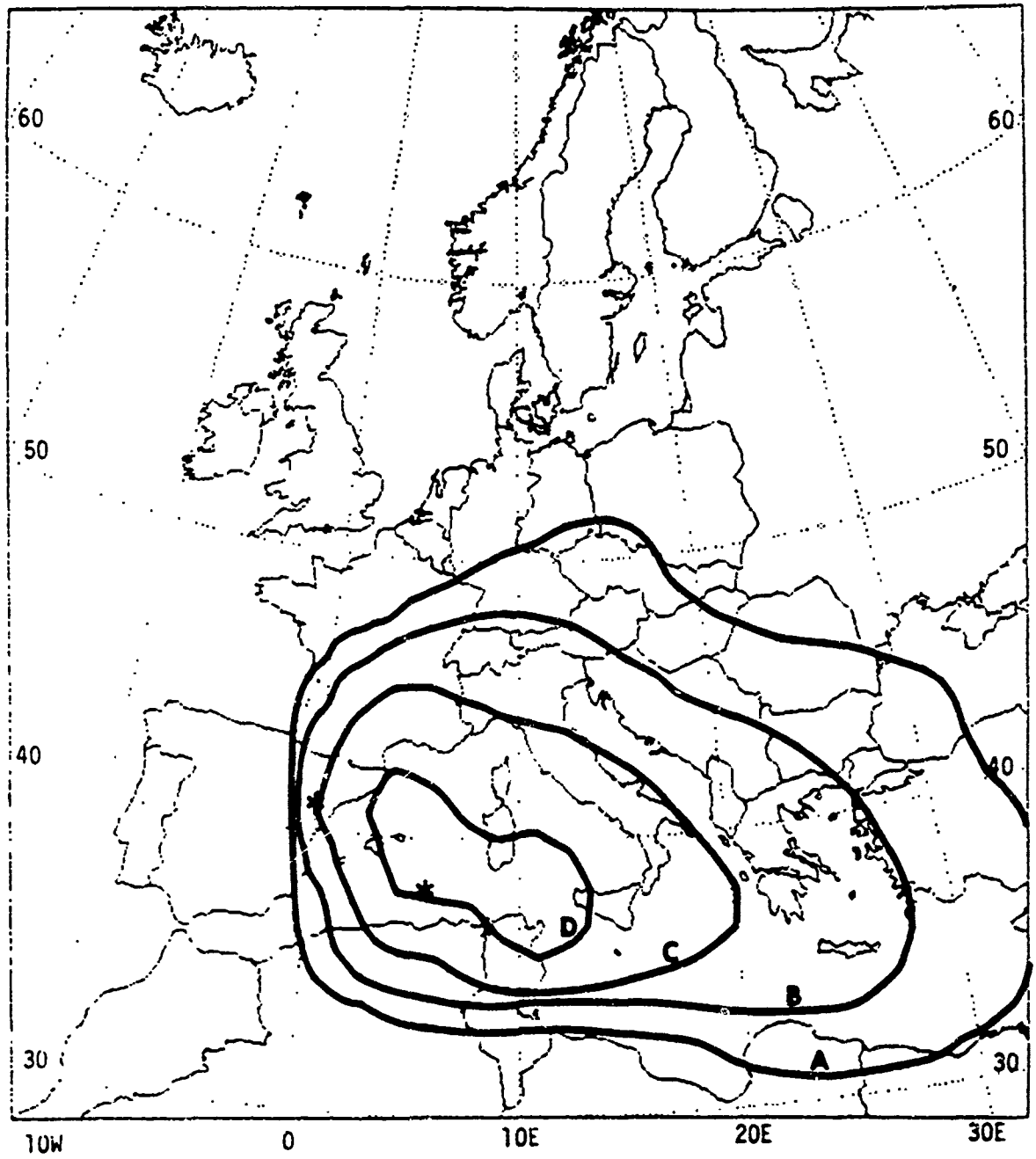

Contour values: $A = 10^{14} cm^{-2}$, $B = 3 \times 10^{14} cm^{-2}$, $C = 10^{15} cm^{-2}$, $D = 3 \times 10^{15} cm^{-2}$.

Figure 2-7. Contours of TEC on paths from the DSCS II Atlantic satellite to Europe at one hour (MICE/MELT results).

[redacted]

The preceding figures in this section show only the mean properties of the disturbed region. However, as discussed earlier, scintillation of a communications signal is caused by plasma striations or fine-scale structure. As discussed in Section 2.2.1, striation effects in the MICE/MELT simulations are based on a linearized, field-line averaged, plasma stability analysis. Figures 2-8 to 2-10 show the resulting electron-density fluctuations ΔN_e at times of 10, 20 and 60 minutes after the bursts. For this problem, an "initial" striation amplitude factor of one percent was assumed and the striation growth was calculated as the problem ran to later times. For times of 5 minutes and earlier, there is little change from the initial condition $\Delta N_e = 0.01 \langle N_e \rangle$ but by 10 minutes after burst the regions of enhanced striation amplitudes are becoming apparent particularly on the southern side of Plume B. At 20 minutes, striated electron densities as high as 3×10^6 cm^{-3} can be seen on the southern side of both plumes, and a small region of 1×10^7 cm^{-3} has appeared on the southern side of Plume B. These striations continue to develop as the problem runs to later times, until at one hour after the bursts, it is clear that the entire southern sides of the plumes are heavily striated.

The use of linear theory in the striation calculation introduces uncertainties in the analysis which are difficult to quantify. Under the linear theory, the core region of the plume (where the electron density is highest) has a tendency to remain unstriated at late times when the rest of the plume is almost entirely striated. This behavior of the central core region is considered to be unrealistic and to be contrary to that expected with nonlinear analysis techniques (Reference 2-15). The current linear striation analysis thus somewhat underestimates the effects of striations in the inner core of the plume at late times. Some quantification of this effect may be obtained by assuming that the plume is fully striated ($\Delta N_e = \langle N_e \rangle$) everywhere to obtain a worst-case estimate of plasma striation. Results illustrating the differences in propagation effects which result from this assumption are presented in Section 3.2.2.

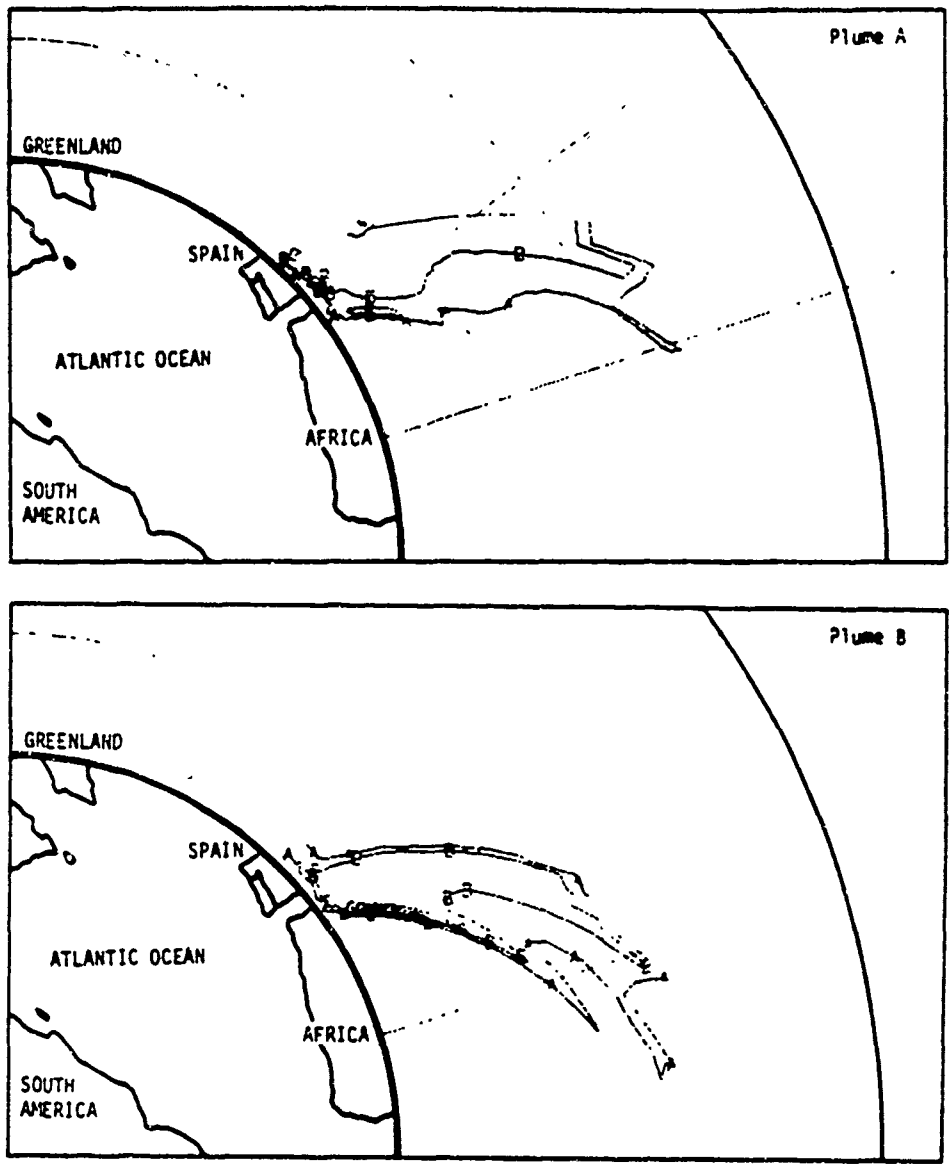

$A = 10^4\ cm^{-3}$, $B = 10^5\ cm^{-3}$, $C = 10^6\ cm^{-3}$, $D = 3 \times 10^6\ cm^{-3}$
$E = 10^7\ cm^{-3}$, $F = 3 \times 10^7\ cm^{-3}$, $G = 10^8\ cm^{-3}$

Figure 2-8. Contours of ΔN_e in magnetic meridian planes through the two plumes at a simulation time of 10 minutes (MICE/MELT results).

[redacted]

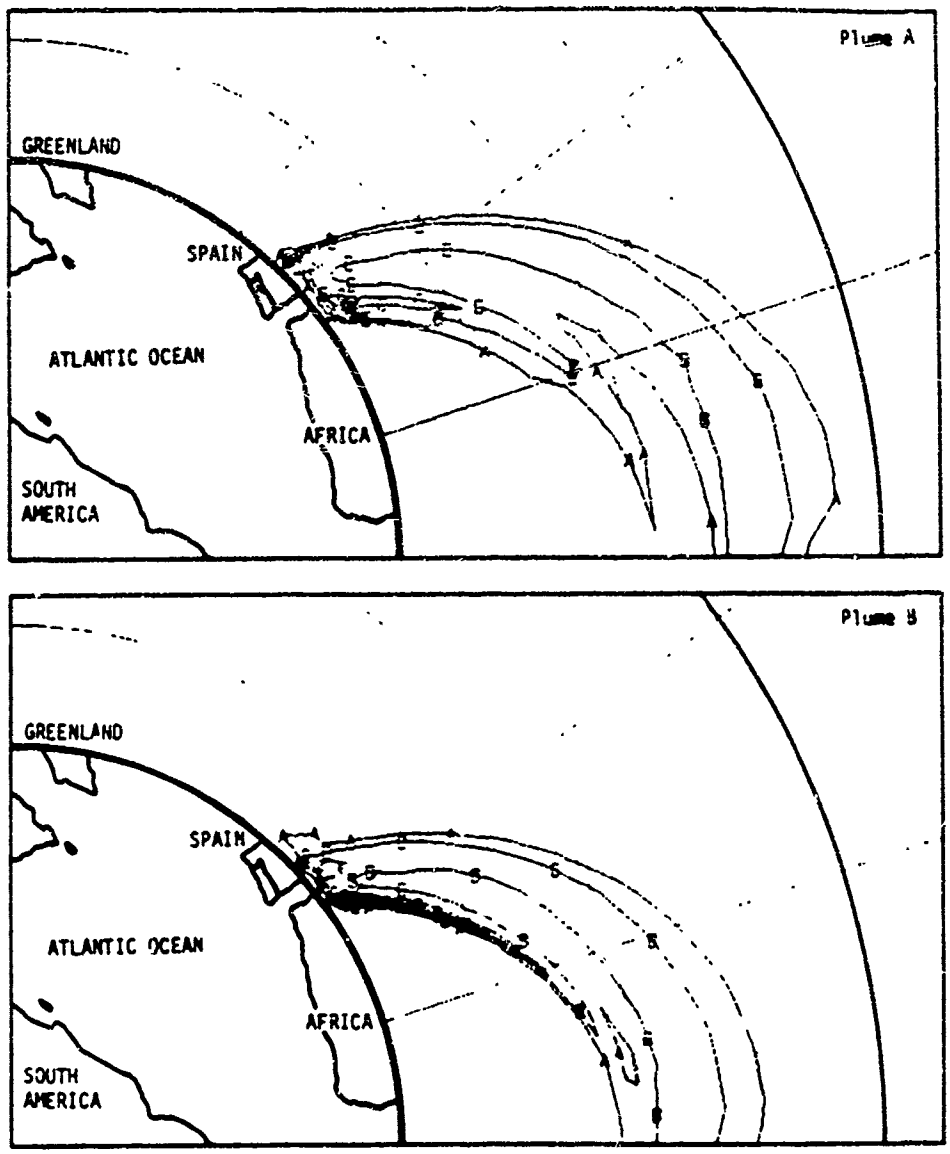

$A = 10^4\ cm^{-3}$, $B = 10^5\ cm^{-3}$, $C = 10^6\ cm^{-3}$, $D = 3 \times 10^6\ cm^{-3}$
$E = 10^7\ cm^{-3}$, $F = 3 \times 10^7\ cm^{-3}$, $G = 10^8\ cm^{-3}$

Figure 2-9. Contours of ΔN_e in magnetic meridian planes through the two plumes at a simulation time of 20 minutes (MICE/MELT results).

[redacted]

[redacted]

[redacted]

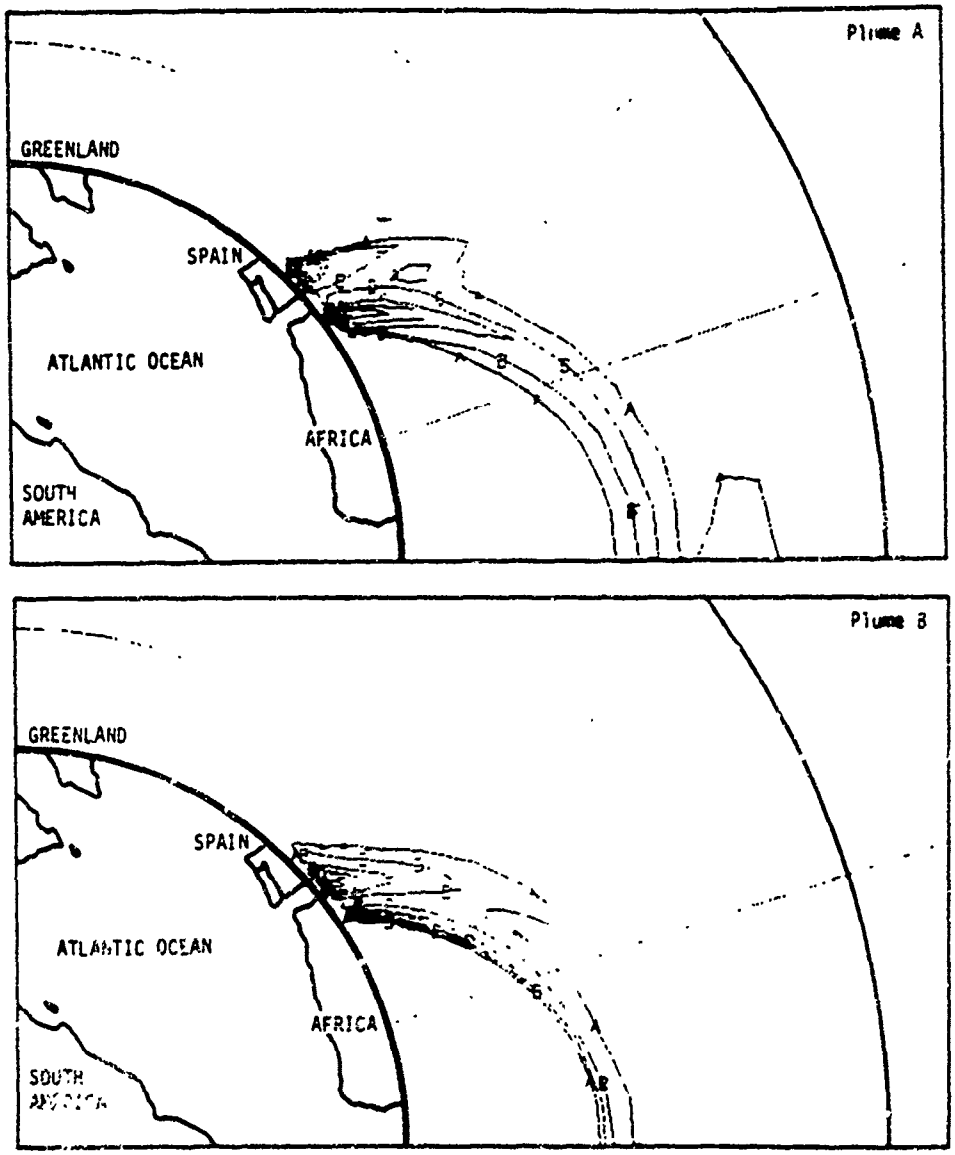

$A = 10^4\ cm^{-3}$, $B = 10^5\ cm^{-3}$, $C = 10^6\ cm^{-3}$, $D = 3 \times 10^6\ cm^{-3}$
$E = 10^7\ cm^{-3}$, $F = 3 \times 10^7\ cm^{-3}$, $G = 10^8\ cm^{-3}$

Figure 2-10. Contours of ΔN_e in magnetic meridian planes through the two plumes at a simulation time of 60 minutes (MICE/MELT results).

[redacted]

[redacted]

[redacted]SECTION 3

PROPAGATION DISTURBANCES

The results of the MICE/MELT, dual burst nuclear phenomenology simulation described in Section 2.3 are used in this section to provide estimates of propagation disturbances at DSCS SHF frequencies. Contour maps of phase standard deviation (σ_ϕ), a parameter which indicates the intensity of ionization irregularity structure along the propagation path, are presented and compared to similar plots calculated with RANC phenomenology models. Results of detailed multiple phase screen (MPS) calculations of received signal amplitude and phase based on the MICE/MELT environment simulation are also described in this section. Maps are presented which show the predicted geographical extent of severe scintillation effects, and which display contours of signal correlation time, a measure of scintillation rate important for modem performance evaluation.

3.1 MICE/MELT — RANC/SATL COMPARISON

This subsection provides a comparison of MICE/MELT and RANC/SATL late time propagation disturbances in terms of predicted phase standard deviation (σ_ϕ). Contour maps are presented which illustrate the geographical extent of specified values of σ_ϕ based on the MICE/MELT and RANC phenomenology descriptions. Phase standard deviation is a parameter which provides a measure of the intensity of the ionization structure on the propagation path and is useful for comparison purposes. The values of phase standard deviation alone, however, do not completely define the resulting scintillation effects. More detailed propagation calculations are required and are discussed in Section 3.2.

[redacted]

The principal properties of striation structure needed to calculate signal scintillation are the rms electron density fluctuation $\langle \Delta N_e^2 \rangle^{1/2}$ and the spatial power spectral density (PSD) of the electron density fluctuations in the propagation medium. The MICE/MELT phenomenology simulation discussed in Section 2 provides estimates of $\langle \Delta N_e^2 \rangle$, but lacks the spatial resolution to calculate the PSD. Nuclear test data provide some information (Reference 3-1), but photographic data resolution is a limiting factor at small spatial wavelengths.

In situ measurements of natural ionospheric irregularity structure very often exhibit a power-law form for the spatial PSD (References 3-2, 3-3). Numerical simulations of nonlinear striation formation have produced similar results (Reference 3-4). Thus, there is a growing body of evidence that the following K^{-2} in situ electron density spatial PSD provides a reasonable representation of striation structure:

$$S_{N_e}(K) = \frac{\langle \Delta N_e^2 \rangle}{\pi} \frac{L_o}{1 + L_o^2 K^2} \quad , \tag{3-1}$$

where $\langle \Delta N_e^2 \rangle$ is the local variance of electron density fluctuations, L_o is the outer scale size, and K is the spatial wavenumber. The corresponding one-dimensional phase PSD is

$$S_\phi(K) = \frac{\langle \Delta\phi^2 \rangle}{2} \frac{L_o}{(1 + L_o^2 K^2)^{3/2}} \quad , \tag{3-2}$$

where $\langle \Delta\phi^2 \rangle$ is the local phase variance. The phase variance along an incremental path segment Δz perpendicular to the field-aligned striation axes is given by

$$\langle \Delta\phi^2 \rangle = 2(r_e\lambda)^2 \langle \Delta N_e^{\ 2} \rangle L_o \Delta z \quad , \tag{3-3}$$

where λ is the RF wavelength, and r_e is the classical electron radius (2.818×10^{-13} cm).

The expression for the incremental phase variance can be generalized for the case of different scale sizes in the crossfield and longitudinal directions and for propagation at arbitrary angles with respect to the geomagnetic field (Reference 3-5). The integrated phase variance along a propagation path through the MICE/MELT environment description is then calculated by

$$\sigma_\phi^{\ 2} = 2(r_e\lambda)^2 \int \frac{a\ L_o \langle \Delta N_e^2 \rangle}{(a^2 \sin^2\psi + \cos^2\psi)^{1/2}}\ dz \ (\text{radians}^2) \tag{3-4}$$

where a is the striation axial ratio (ratio of characteristic length along the field-aligned striation axes to transverse scale size), and ψ is the angle between the propagation path and the geomagnetic field ($\psi = 90°$ for propagation perpendicular to the field). For most geometries where the propagation path is at least 5 to 10 degrees from parallel with the field, the standard deviation of phase (σ_ϕ) is essentially independent of the striation axial ratio. Therefore this is not an especially critical parameter in the calculation. A value of 10 was assumed for the axial ratio for the MICE/MELT propagation calculations presented in this report.

The outer scale L_o is an important parameter, and is currently subject to some uncertainty. For the ionosphere, current estimates of the outer scale range from hundreds of meters (Reference 3-6) to the order of 10 kilometers (Reference 3-2). From Equation 3-4 it is seen

that the calculated value of σ_ϕ increases in proportion to $\sqrt{L_o}$. However, for the PSD form of Equation 3-2 it is actually the ratio $\langle \Delta N_e^2 \rangle / L_o$ that is the critical parameter in determining scintillation intensity. Thus larger values of L_o are found to decrease the predicted spatial extent of intense scintillation somewhat for a given spatial distribution of electron density variance.

The RANC/SATL formulation (Reference 3-7) for integrated phase variance employs a distribution of striation sizes based on an analysis of Checkmate photographic data by Chesnut. As pointed out in Reference 3-1 this spectrum may underestimate the amount of small scale striation structure due to resolution in the photographic data base. In recent work ESL has used the RANC model for rms phase fluctuations, but has assumed a K^{-3} power-law form for the phase PSD with parameters chosen to match the Chesnut distribution at 1 km scale size (Reference 3-8). This results in a corresponding scale size in our formulation of slightly more than 1 km.* Therefore for comparison purposes in this report we have used $L_o = 1$ km in the MICE/MELT phase standard deviation contours.

Contour maps of phase standard deviation for the dual burst scenario are presented in Figures 3-1 through 3-8 for times from 10 minutes to 1 hour after detonation. Results based on the MICE/MELT phenomenology simulation and RANC/SATL models are shown at each calculation time. The DSCS II Atlantic satellite location at 13 deg west longitude is used for these calculations. The radio frequency is 7.5 GHz, the center of the DSCS II downlink frequency band. The burst ground zero locations are indicated by the asterisks on the maps.

---

* After accounting for a factor of 2π difference in definition of the scale size.

The MICE/MELT contours are obtained by integrating the phase variance along many paths from the satellite to a set of ground points. The locations of specified values of σ_ϕ are found by interpolation between computed values and the resulting contours are plotted on a map of the affected region as shown. The contours enclose the spatial regions at each calculation time within which the phase standard deviation on links to or from the DSCS Atlantic satellite equal or exceed the indicated value. Contour values are presented in degrees for comparison with similar contour maps based on RANC phenomenology models provided by Dr. J. Marshall of ESL, Incorporated (Reference 3-9).

The MICE/MELT and RANC/SATL results calculated at 10 minutes after detonation are shown in Figures 3-1 and 3-2 respectively. The plasma stability analysis in the MELT simulation predicts relatively little striation development at this time. The contours in Figure 3-1 based on the MELT results show an extensive region of weak SHF scintillation effects with maximum σ_ϕ values less than several hundred degrees. In contrast, the RANC models predict much more severe effects at this time. Values of phase deviation in excess of several thousand degrees are shown in Figure 3-2 over large areas of Europe with values greater than 9000 degrees in most of West Germany. These large σ_ϕ values result from the RANC code striation model which turns the striations on relatively early when the electron densities in the fireball are very high.

The dashed line on Figure 3-2 shows the shadow or projection on the earth of the tube formed by the earth's magnetic field lines which enclose the lower portion of the RANC fireball. The RANC phenomenology model uses simple, spheroidal geometries to represent ionized fireballs. Striation effects do not extend to the plume region shown since the striations are confined to the fireball region which expands upward along assumed straight field lines. The fireball ionization region as modeled in RANC

[redacted]

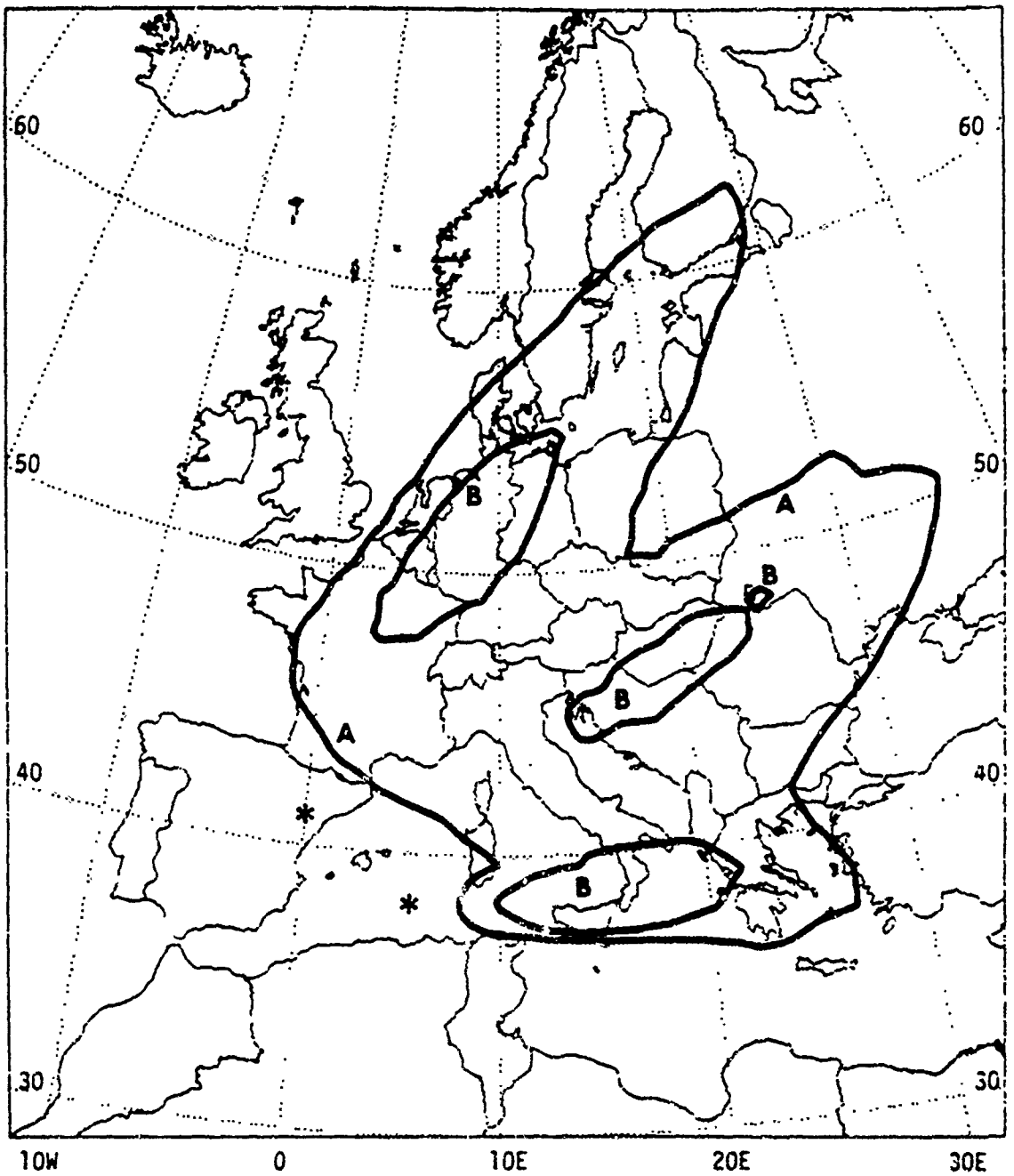

Contour values: A = 100, B = 300 degrees.

Figure 3-1. Contours of phase standard deviation (σ_ϕ) for the MICE/MELT multiburst simulation at 10 minutes.

[redacted]

[redacted]

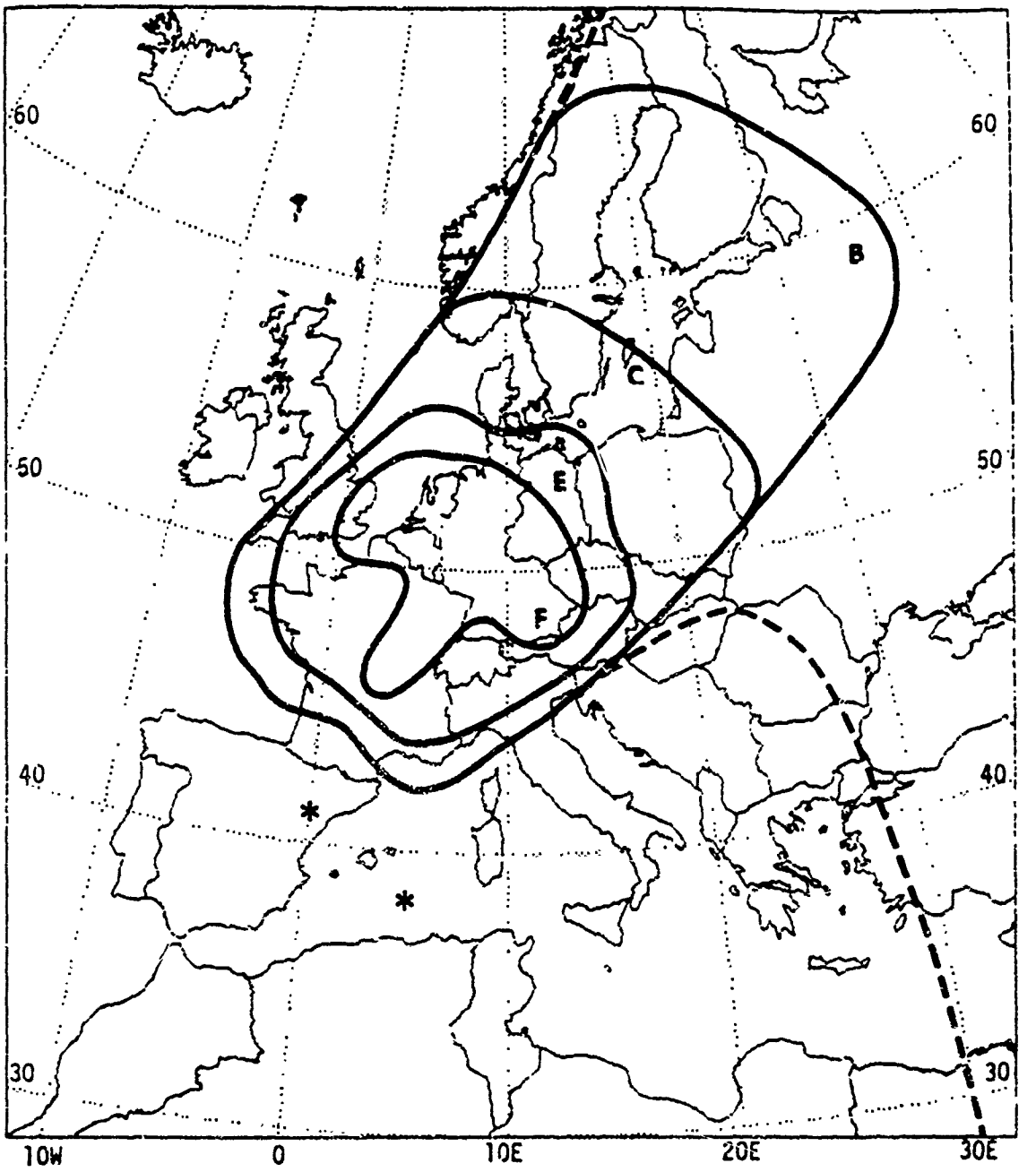

Contour values: B = 300, C = 1500, E = 6000, F = 9000 degrees.

Figure 3-2. Contours of phase standard deviation (σ_ϕ) based on RANC phenomenology models at 10 minutes.

[redacted]

differs substantially at very high altitudes from the field aligned ionization plume expected to occur after a high altitude nuclear detonation.

A second difference in the calculations is the location of the disturbed regions, with the RANC contours projecting farther north than the MELT contours. At this time the difference in contour locations is apparently due primarily to the fireball rise model in the RANC code which allows the fireball to rise ballistically across geomagnetic field lines to a greater extent than predicted in the MICE/MELT simulation. Gravitational forces included explicitly in the MELT code also tend to move the ionization significantly southward at later times, but gravity is not a major effect at this early calculation time.

Contours of σ_ϕ based on MICE/MELT and RANC phenomenology at 20 minutes after detonation are displayed in Figures 3-3 and 3-4 respectively. A substantial increase in striation amplification is apparent in the MELT results at this time as can be seen by comparison of Figure 3-3 with Figure 3-1. By twenty minutes the MELT 300 degree σ_ϕ contour has expanded to cover a very large area. Smaller regions of much larger effects caused by striation development at lower altitudes on the sourthern sides of the plumes are seen at this time. The continuing southward drift of the ionization in the MELT calculation due to gravity and neutral wind forces can be seen by comparison of the σ_ϕ contours at 10 and 20 minutes after detonation. The separation of the plumes in the MELT results is also evident in Figure 3-3.

Comparison of Figure 3-3 with the RANC results in Figure 3-4 shows that the overall extent of scintillation effects is considerably larger in the MELT calculation at this time. The RANC model still predicts substantially more severe effects at lower altitudes in the fireball regions. Values of σ_ϕ in excess of 6000 degrees appear in the RANC results in the interior of the E contour, whereas peak σ_ϕ values in the MELT results

[redacted]

THIS PAGE IS INTENTIONALLY LEFT BLANK.

[redacted]

[redacted]

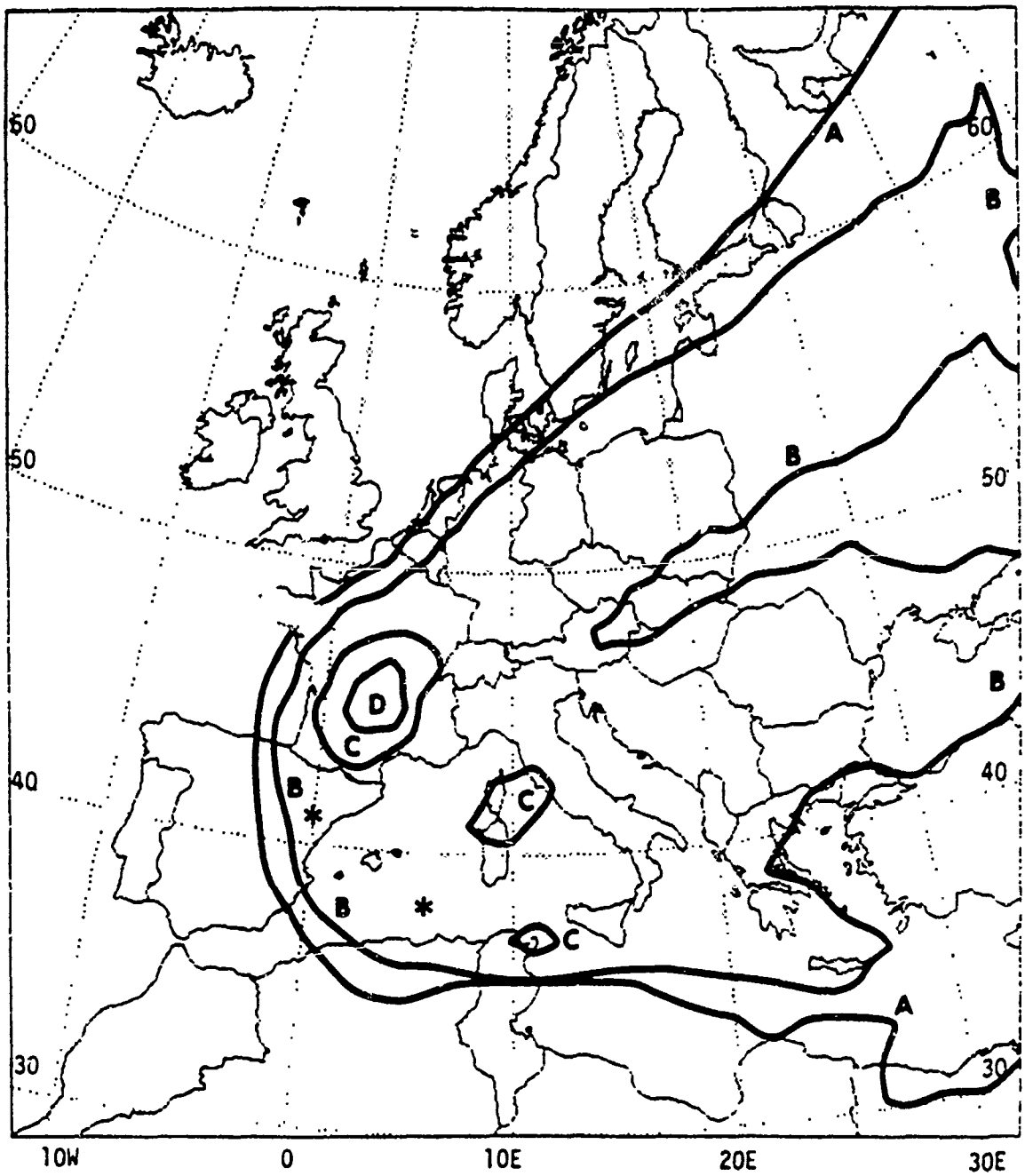

Contour values: A = 100, B = 300, C = 1500, D = 3000 degrees.

Figure 3-3. Contours of phase standard deviation (σ_ϕ) for the MICE/MELT multiburst simulation at 20 minutes.

[redacted]

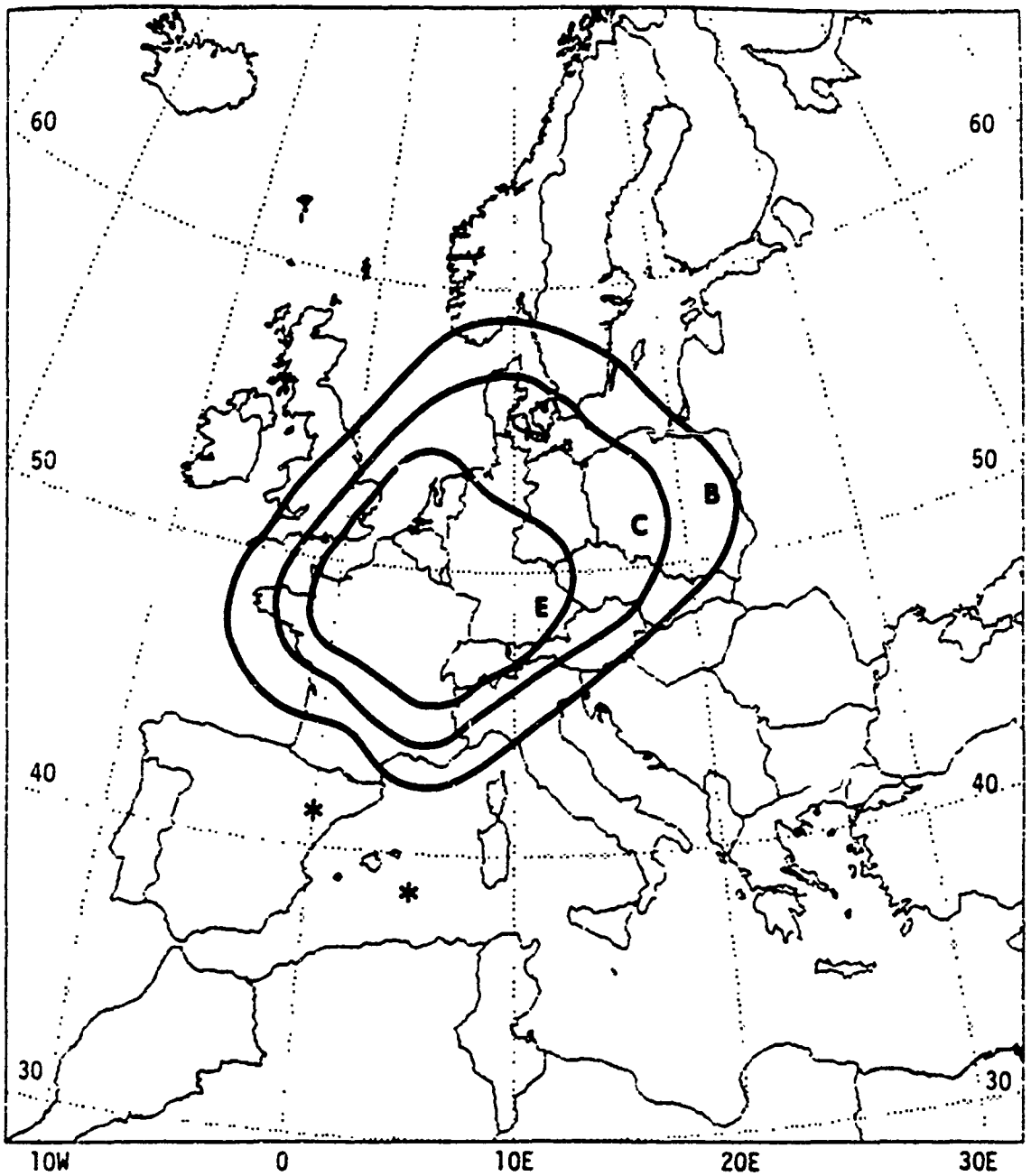

Contour values: B = 300, C = 1500, E = 6000 degrees.

Figure 3-4. Contours of phase standard deviation (σ_ϕ) based on RANC phenomenology models at 20 minutes.

are 3000 to 4000 degrees in a relatively small region. Scintillation effects based on the RANC model, however, are decreasing both in spatial extent and severity with time due to fireball deionization. In contrast, results of the MELT plasma stability analysis predict increasing striation formation and resulting scintillation effects with time. In addition, the region affected by scintillation in the MELT calculation is substantially south of the disturbed region as calculated by the RANC model.

The trends in the comparison of scintillation effects noted above continue to late times. The results at 30 minutes after detonation are shown in Figure 3-5 for MELT phenomenology and in Figure 3-6 for the RANC model. A substantial increase in the extent of severe scintillation effects has occurred in the MELT calculation results at this time. This can be seen by comparison of the C contours (1500 degrees) in Figures 3-3 and 3-5. The extent of intense scintillation effects is now larger in the MELT calculation than in the calculation based on the RANC models, shown in Figure 3-6.

The reader should also note that the present comparisons are for for frequencies at SHF. At lower frequencies used in some satellite systems (e.g., AFSATCOM UHF and GPS L-band frequencies) severe scintillation effects would occur over most of the region bounded by the A contour in the MELT results in Figure 3-5, whereas the RANC effects would still be contained within the projections of the fireballs models, i.e., essentially within the boundaries of the B contour in Figure 3-2. Differences in extent of effects would therefore be considerably more pronounced at lower satellite frequencies.

The final comparison, at a calculation time of one hour, is presented in Figures 3-7 and 3-8. At times of one hour or greater the MICE/MELT phenomenology calculation predicts substantially larger scintillation extent than predicted by the RANC model The regions of most intense scintillation are also larger in the MELT results (compare the C and D contours in Figures 3-7 and 3-8) and are shifted to the south. The plume ionization and resulting scintillation contours would continue to drift southward at

effects
t and

nation
n
ch

above
e
AND
ffects
e seen
The
ulation

for

lation
n the
ntained
in the
ffects
quencies.

pro-
CE
ation
scin-
ntours
ation
l a

THIS PAGE IS INTENTIONALLY LEFT BLANK.

[redacted]

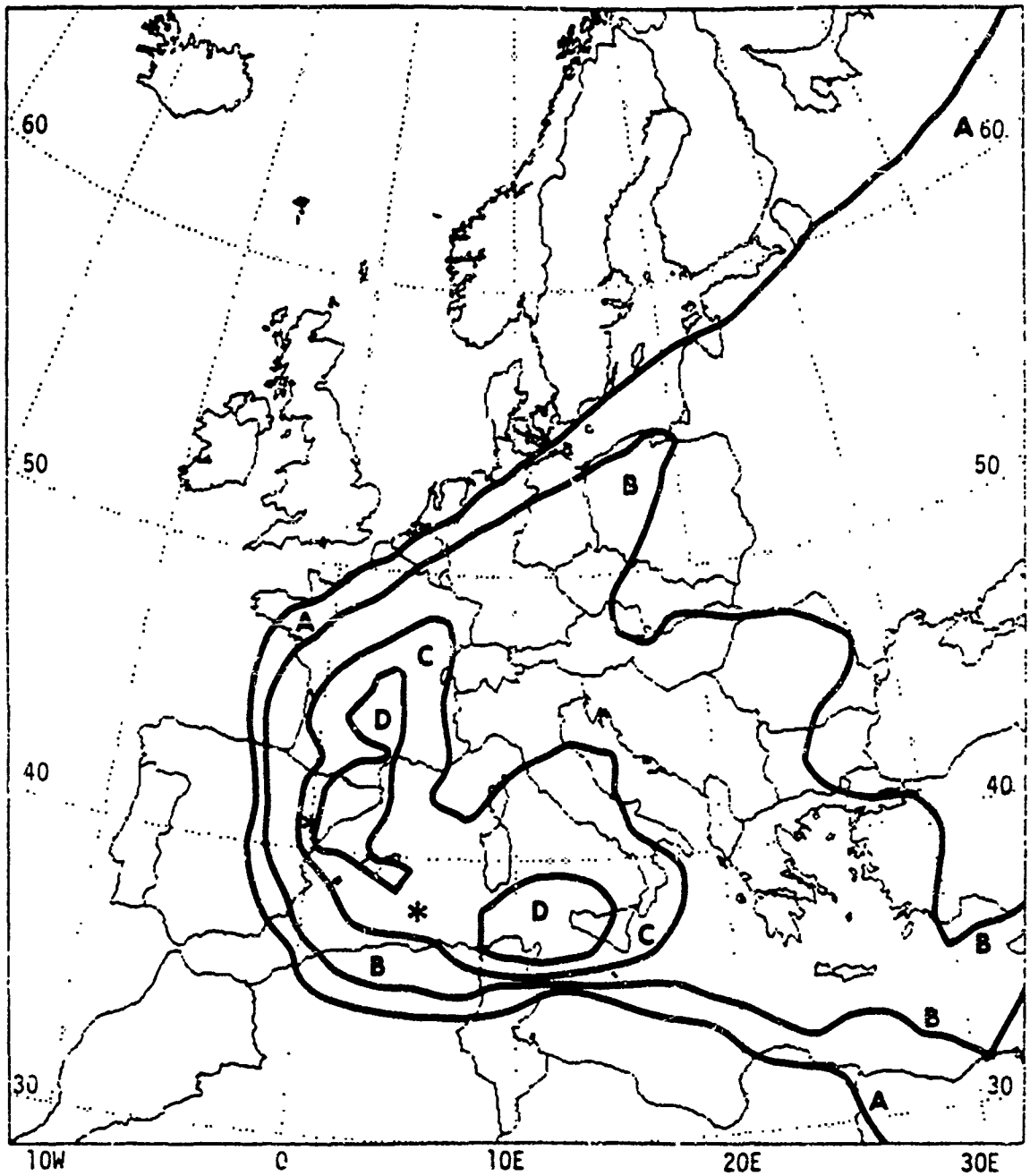

Contour values: A = 100, B = 300, C = 1500, D =3000 degrees.

Figure 3-5. Contours of phase standard deviation (σ_ϕ) for the MICE/MELT multiburst simulation at 30 minutes.

[redacted]

[redacted]

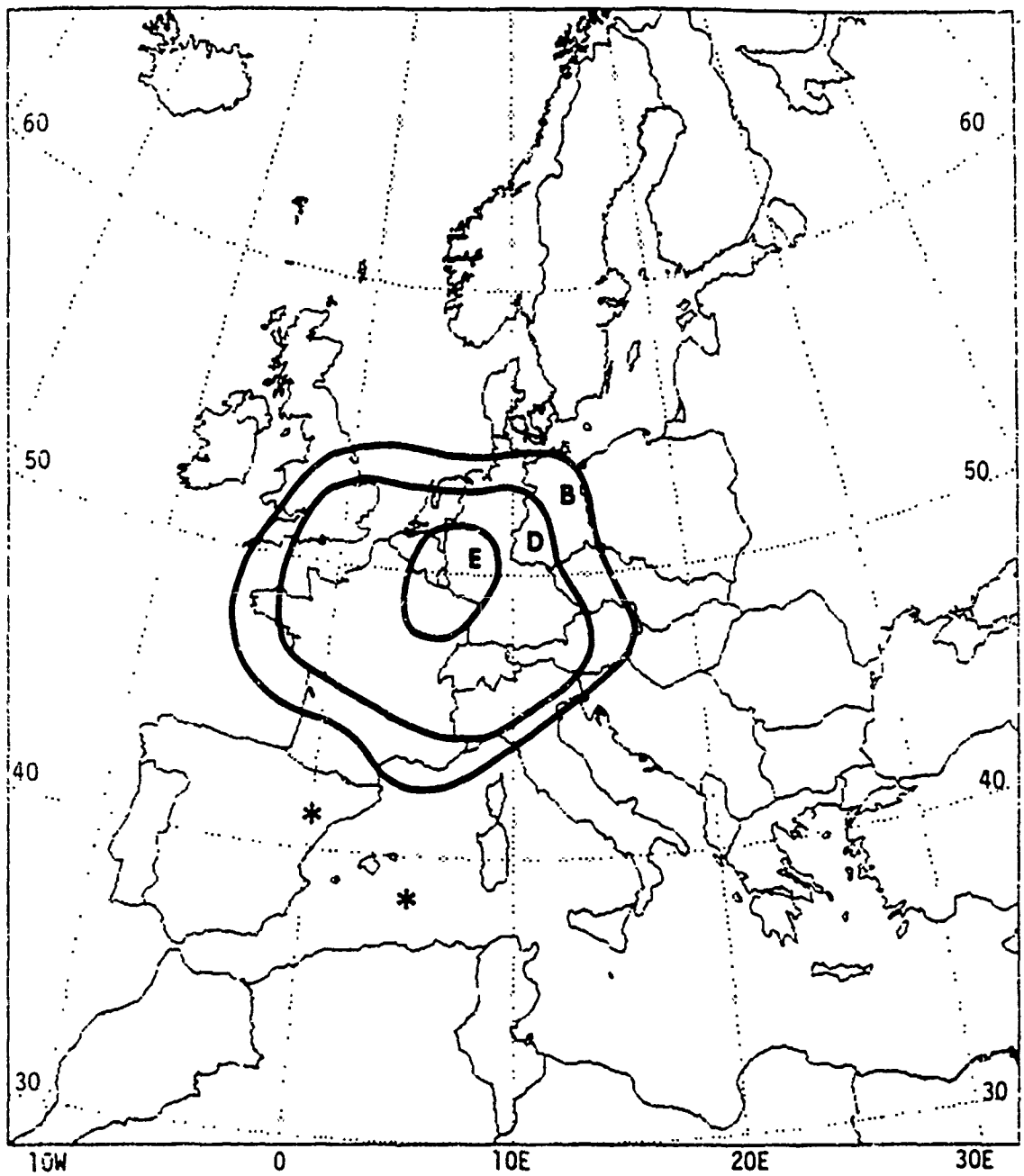

Contour values: B = 300, D = 3000, E = 6000 degrees.

Figure 3-6. Contours of phase standard deviation (σ_ϕ) based on RANC phenomenology models at 30 minutes.

[redacted]

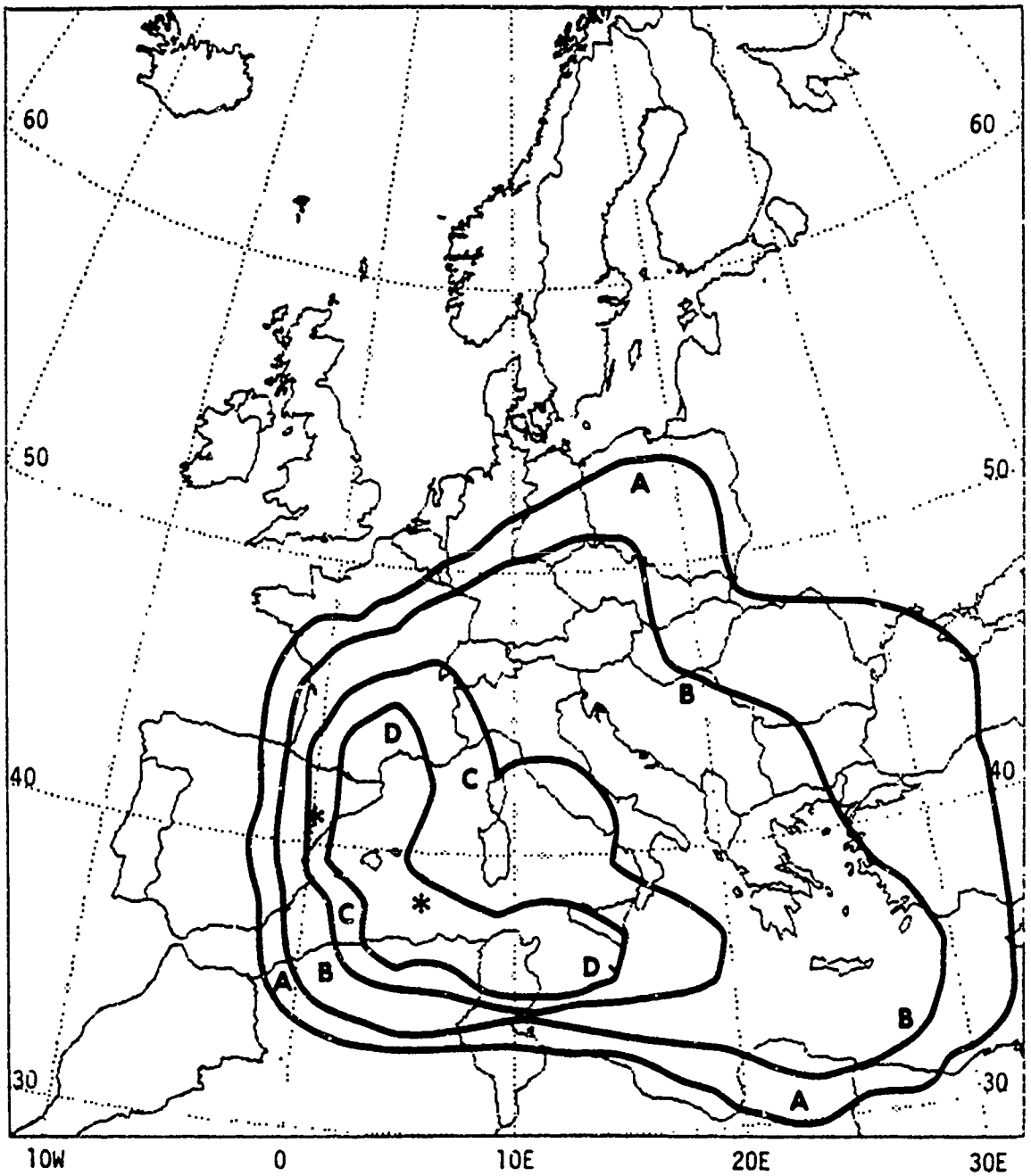

Contour values: A = 100, B = 300, C = 1500, D = 3000 degrees.

Figure 3-7. Contours of phase standard deviation (σ_ϕ) for the MICE/MELT multiburst simulation at one hour.

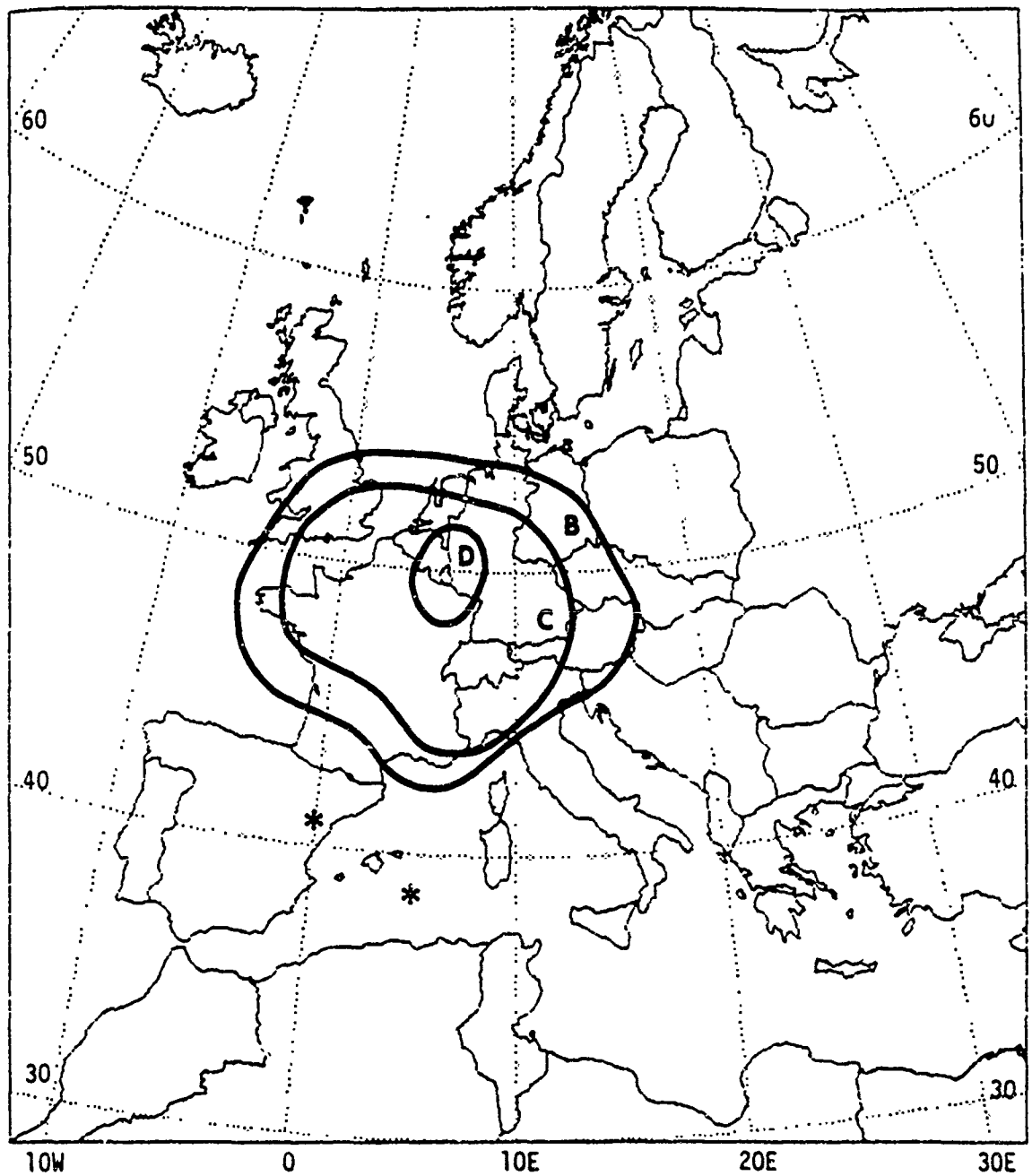

Contour values: B = 300, C = 1500, D = 3000 degrees.

Figure 3-8. Contours of phase standard deviation (σ_ϕ) based on RANC phenomenology models at one hour.

later times causing growing discrepancies between the MELT results and the RANC results which do not include any motion once fireball expansion is completed.

It is clear from the above comparisons that major differences exist in predictions of propagation disturbances between the detailed MICE/MELT phenomenology simulation and the empirical RANC/SATL phenomenology models. Substantial differences are noted in the extent, location, and severity of scintillation effects as a function of time in this scenario. The differences are due to inadequacies in several aspects of the late-time RANC phenomenology model, and possible lack of early-time blast wave turbulence in the MICE/MELT simulation.

The RANC model is clearly inadequate to represent the late time, field-aligned ionization plume produced by a high altitude, large yield nuclear detonation, and was, in fact, never intended for this purpose. The late time plume geometry is not modeled in the RANC phenomenology code. Late time nuclear effects, however, are very important to strategic satellite communication systems.

The RANC modeling of fireball expansion and rise across the magnetic field yields results substantially different from the results of the detailed phenomenology simulation. Thus the location of the region of propagation effects at early times is different. The late time motion of the ionization plume is another effect not included in the RANC phenomenology package. This omission can be very important since substantial southward motion of the northern end of the plume can occur as the high altitude ionization drifts across the magnetic field due to gravitational forces.

Striation formation in the RANC phenomenology code also differs substantially from the results of the plasma stability analysis in the MELT simulation. The striation onset time in the RANC model does not agree with the MELT linear analysis for this case, resulting in predictions of substantially more severe scintillation effects by RANC/SATL at early times. The

linear plasma stability analysis in the MELT code is expected to provide a reasonable estimate of initial wind-driven striation development for very high altitude detonations where blast wave turbulence is not expected to be widespread, as is the case here. At times approaching one hour nonlinear wind-driven and gravitational processes are expected to become significant. This increases the severity of scintillation effects predicted by the MELT code at late times. At the late times, however, the RANC results show less severe scintillation than the MELT linear analysis. This discrepancy is probably due to inadequate modeling of late time ionization in RANC. Potential effects of nonlinear striation formation on the MELT results is discussed further in Section 3.2.2.

3.2 MICE/MELT SCINTILLATION EFFECTS

3.2.1 Signal Structures

A multiple phase screen (MPS) propagation simulation (Reference 3-10) was used to calculate signal amplitude and phase scintillation versus time on a link from the DSCS Atlantic satellite at 13 deg west longitude to a ground terminal at Landstuhl, Germany (49.25° N Lat, 7.35° E Lon). The MICE/MELT dual burst simulation was used to provide the disturbed environment conditions as a function of position along the propagation path. The uplink signal was assumed to be undisturbed. A similar scenario has been investigated previously using RANC phenomenology models (Reference 3-11).

An inverse power-law PSD with a 1 km outer scale size (Equation 3-2) was used to represent the striation structure for these calculations. Due to uncertainties in the scale size, L_o, is it usually treated parametrically in our link evaluations (Reference 3-12). This was not practical within the scope of the present effort. As discussed in Section 3.1, a 1 km value is appropriate for comparison with recent ESL results. This value is currently believed to be near the lower end of the range of appropriate scale sizes and therefore should provide a conservative upper estimate of scintillation effects.

Figures 3-9 to 3-12 display portions of the representations of received signal structure obtained for the Landstuhl link at times of 10, 20, 30 and 60 minutes after detonation. The plots show signal amplitude in decibels relative to the mean signal level. The corresponding signal phase is plotted in a 4π radian interval between $\pm 2\pi$ radians. In the plots of signal phase, 2π has been added to or subtracted from successive values to keep the phase within the plot boundary. The sharp discontinuities observed in the phase plots are a result of the plotting technique and are not real phase changes.

The MPS realizations shown here were computed over a total distance of 30 km with a spatial resolution of 1.83 meters, obtained using 16,384 points in the MPS receiver-plane grid. In all cases the striated region was approximated by ten phase-screens whose location and phase standard deviation were chosen to best match the propagation conditions on the path as determined by the phenomenology simulation.

The MPS distance scales are converted to time scales in the plots of signal structure by dividing by an effective velocity, V_{eff}, obtained by taking into account relative motion of the propagation path and striated plasma. The velocity of concern is the component of the relative velocity between the propagation path and the striated plasma in a direction normal to the path and to the striation axes. In general, the effective velocity is obtained by taking a weighted average of the relative velocity at points along the propagation path including any motion of the transmitter and receiver as well as motion of the plasma. The relative velocity is weighted by the intensity of the ionization structure along the path. For the case being considered, the satellite transponder and receiver are assumed to be fixed and the effective velocity is a function only of plasma motion computed by the MICE/MELT simulation and the propagation path geometry. The velocities at early times are relatively high. An effective velocity of 500 m/sec is used for the 10 minute calculation time (Figure 3-9) based on the MELT results. At later times, up to one hour after detonation, the effective velocities obtained from the MELT data for the Landstuhl link

THIS PAGE IS INTENTIONALLY LEFT BLANK.

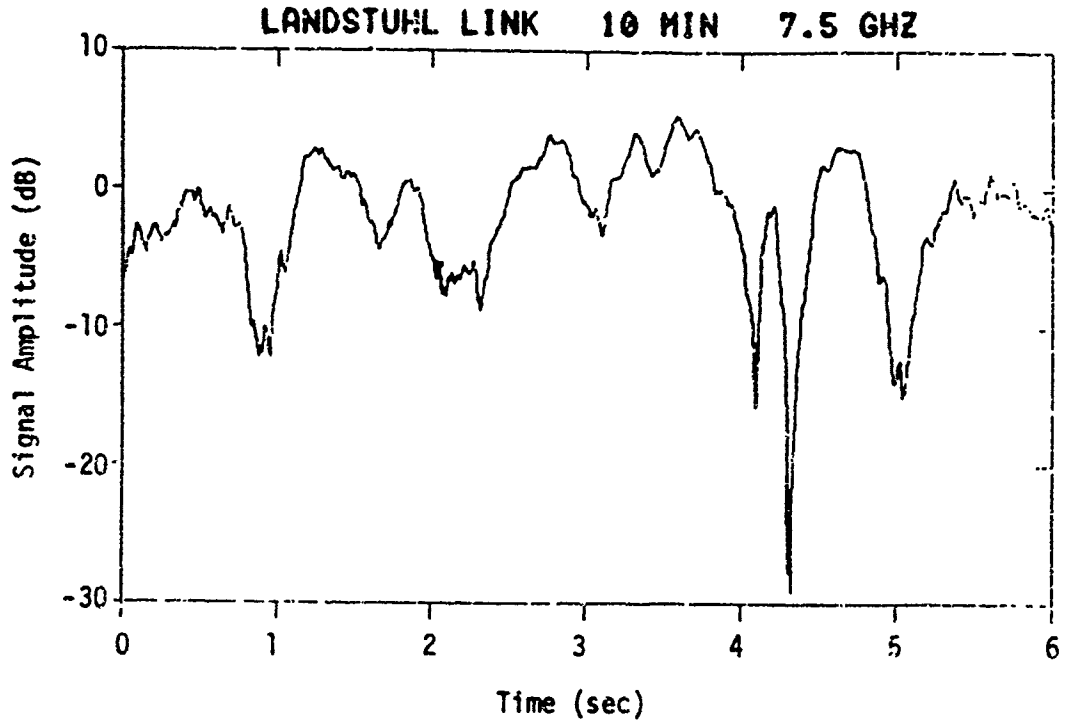

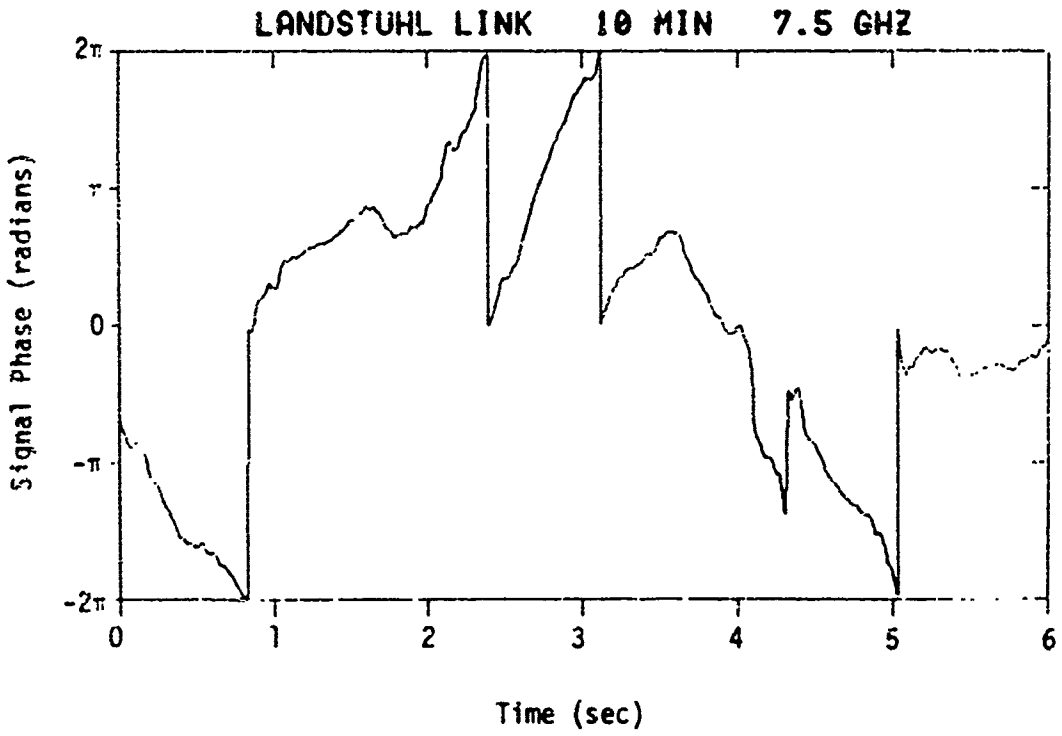

Figure 3-9. Signal amplitude and phase at Landstuhl at 10 minutes.

[redacted]

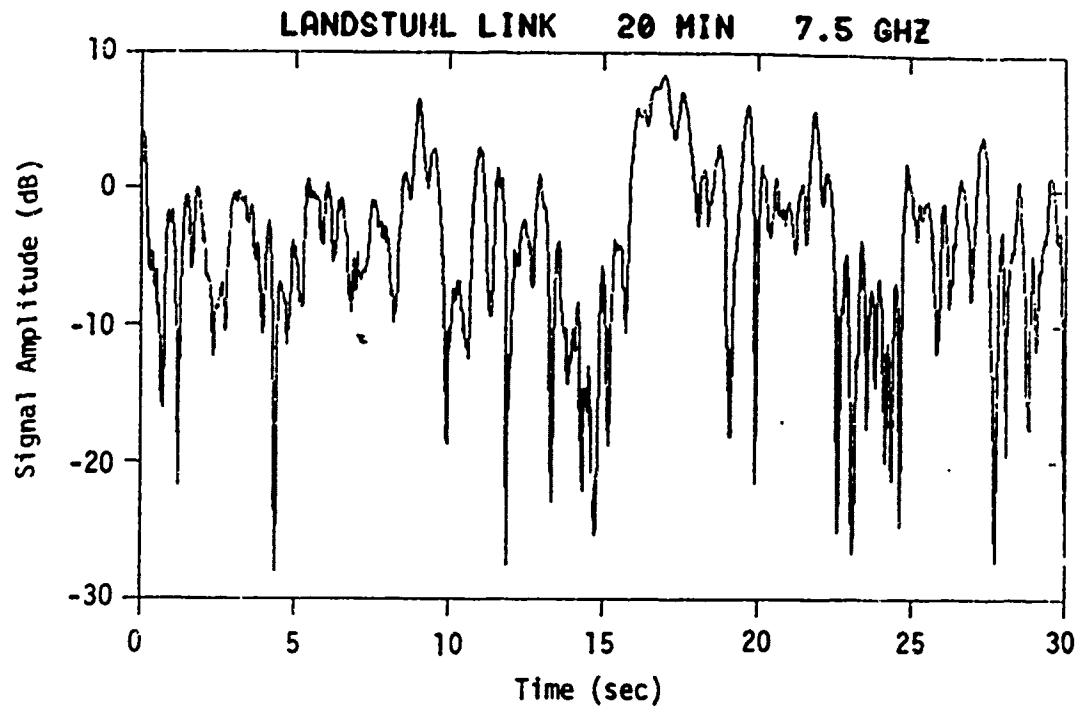

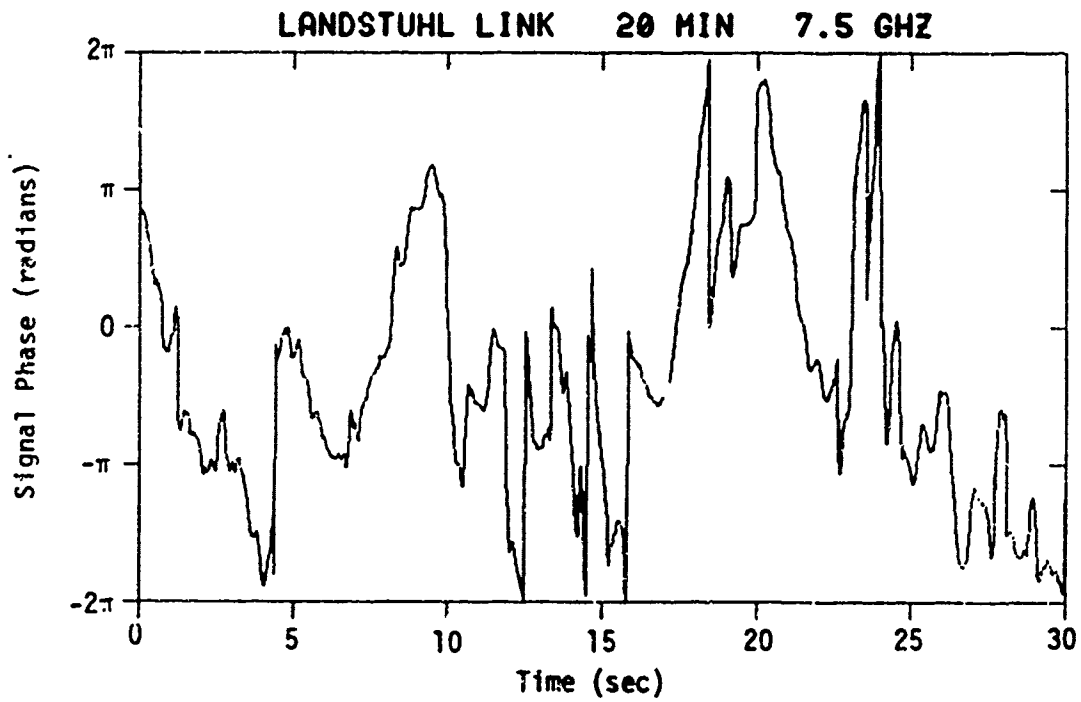

Figure 3-10. Signal amplitude and phase at Landstuhl at 20 minutes.

[redacted]

[redacted]

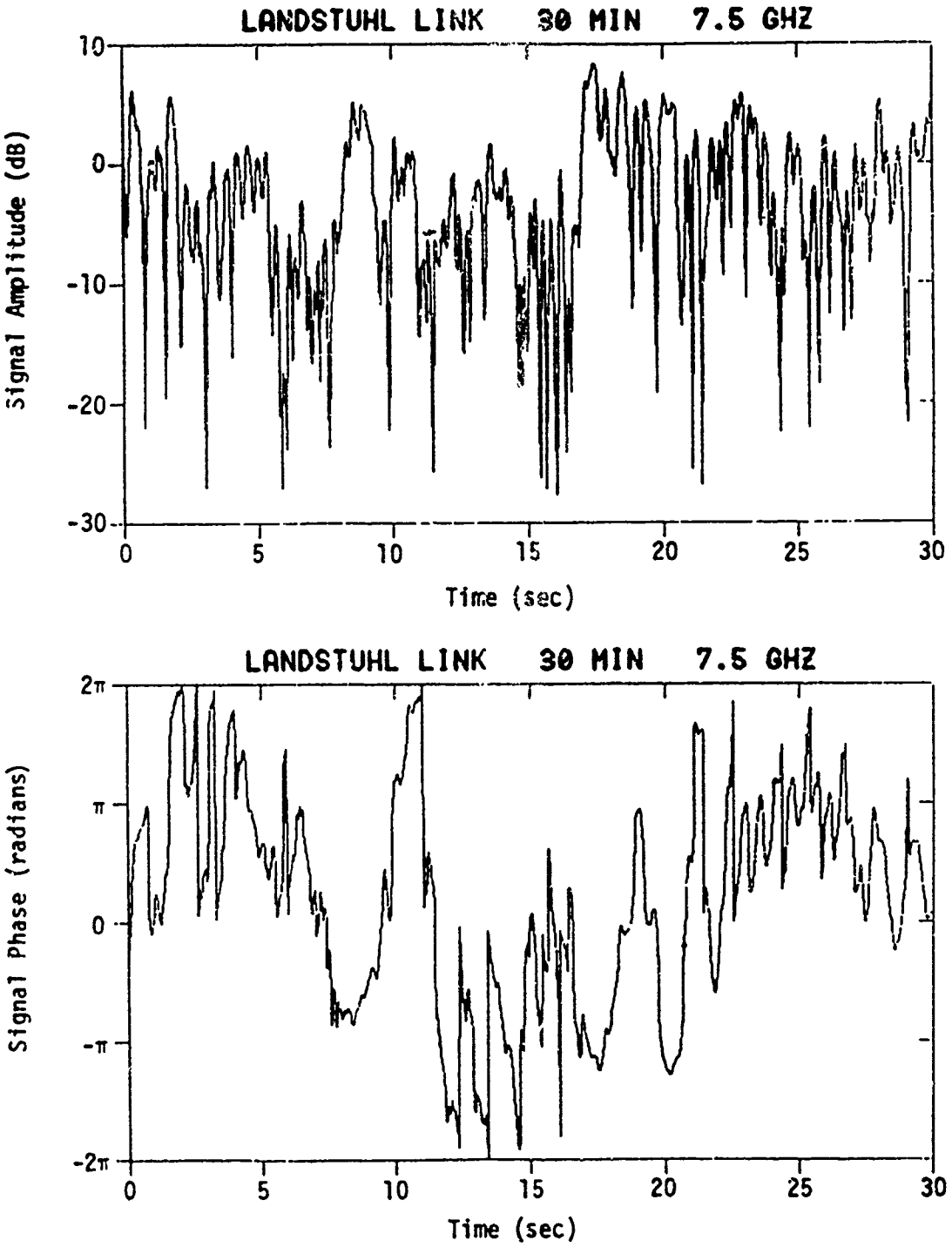

Figure 3-11. Signal amplitude and phase at Landstuhl at 30 minutes.

[redacted]

[redacted]

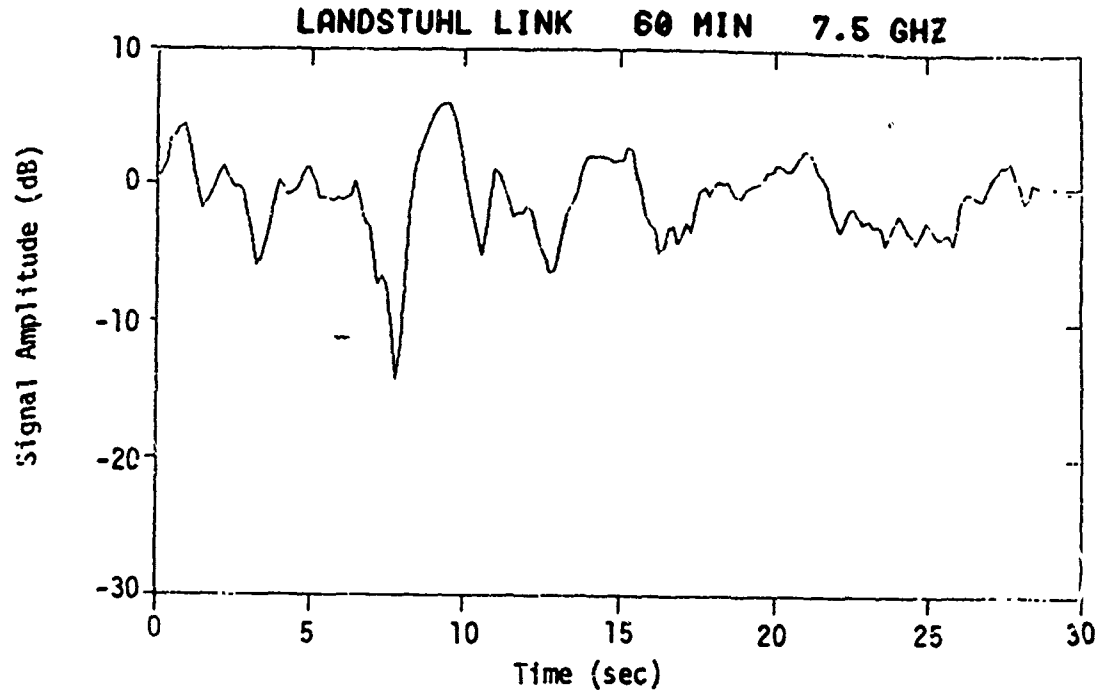

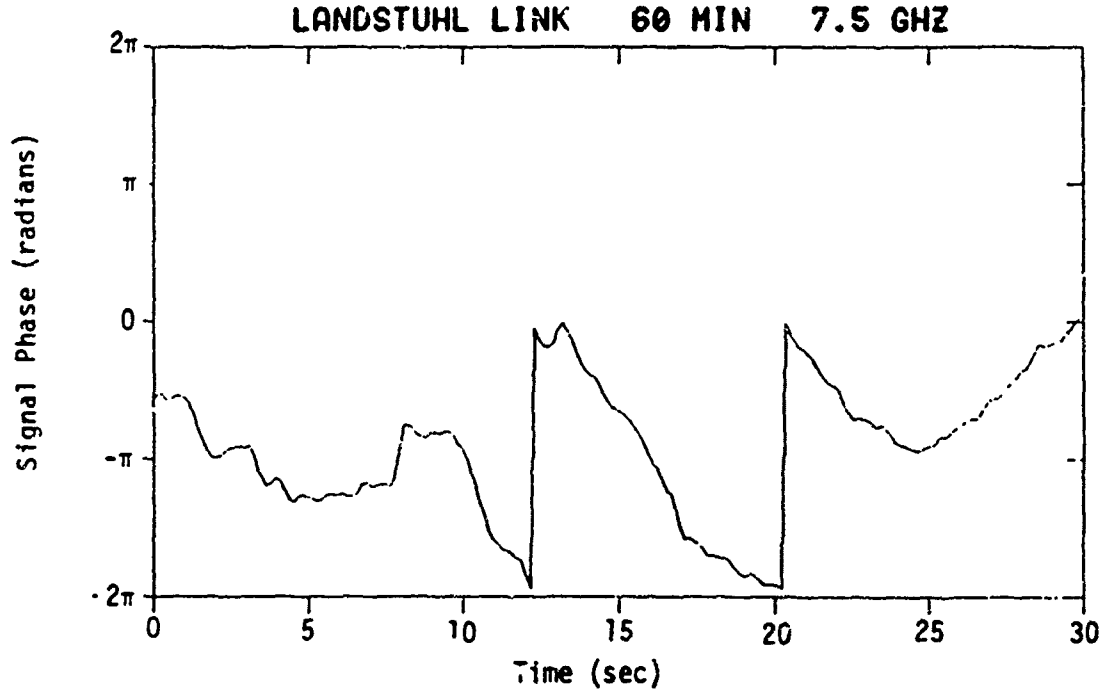

Figure 3-12. Signal amplitude and phase at Landstuhl at one hour.

[redacted]

are on the order of 100 m/sec and this value is used to obtain the time scales at 20, 30, and 60 minutes after detonation. Thus figures 3-9 through 3-12 correspond to likely representations of signal structures received by a ground-based DSCS terminal at Landstuhl based on the MICE/MELT dual burst simulation.

The velocities noted above obtained from the MICE/MELT simulation include effects of gravitational forces and burst induced interactions in an initially stationary ambient atmosphere. Effects due to ambient winds were not included in the simulation. Natural winds vary in both magnitude and direction on a daily and seasonal basis and exhibit substantial fluctuations about mean levels. During periods of normal geomagnetic activity peak winds are on the order of a few hundred meters/sec. During geomagnetic storm periods, which occur relatively infrequently, ambient winds can approach 1 km/sec (Reference 3-13). These winds can cause significant striation east-west drift with the direction depending on the time of day. The winds can similarly affect the north-south motion, although a general southward drift is still expected to occur. Specific results for late time striation motion and effective velocities can therefore depend significantly on ambient wind conditions in the time period following the detonation. Further discussion of late time striation motion can be found in Reference 3-14.

Table 3-1 summarizes the input phase standard deviation and the statistical results of the MPS simulations for the Landstuhl link. The measurements of signal statistics shown were obtained by averaging the results of ten MPS simulations with statistically similar phase screens. The results tabulated include the S_4 scintillation index, the signal correlation length, signal correlation time, and the intensity correlation length. The S_4 scintillation index is defined as the normalized standard deviation of signal power and is thus a measure of the intensity of

Table 3-1. Summary of MPS cases for the Landstuhl link.

Time After Detonation	Phase Standard-Deviation	S_4 Scintillation Index	Signal Correlation Length	Signal Correlation Time	Intensity Correlation Length
10 min	6.1 rad	0.75	145 m	0.3 sec	68 m
20	17.2	1.09	42	0.4	31
30	24.7	1.06	28	0.3	20
60	5.1	0.64	182	1.8	72

amplitude fading.* The signal correlation length is defined as the distance corresponding to the e^{-1} point on the spatial autocorrelation function of the complex electric field measured in the receiver plane. The signal correlation time, τ_o, is the e^{-1} point on the time autocorrelation function of the complex signal at the receiver and is related to the signal correlation length and the effective velocity by

$$\tau_o = \ell_o / V_{eff} \tag{3-5}$$

---

* In terms of signal voltage amplitude A, S_4 is defined as

$$S_4 \triangleq \left[\frac{\langle A^4 \rangle - \langle A^2 \rangle^2}{\langle A^2 \rangle^2} \right]^{1/2} . \tag{3-6}$$

In intense scintillation the S_4 index saturates at unity, characteristic of Rayleigh amplitude statistics. S_4 is zero for no scintillation and may exceed unity prior to saturation.

Another useful measure of signal correlation summarized in Table 3-1 is the intensity or amplitude correlation length, which is defined as the e^{-1} point of the spatial autocovariance function of the signal intensity ($I = EE^*$). For Rayleigh signal statistics (saturated scintillation) these two measures of signal fading rate have a simple relationship. This is discussed further in Section 3.2.2.

The received signals at times of 20 and 30 minutes after detonation shown in Figures 3-10 and 3-11 are characterized by saturated, Rayleigh statistics with scintillation index near unity. At 30 minutes the signal fading is faster, with a value of signal correlation time of about 0.3 seconds. Scintillation is less intense at 10 minutes after detonation as shown in Figure 3-9, because substantial striation growth has not taken place at this time in the MELT simulation. At 60 minutes after detonation scintillation on the Landstuhl link is less severe because the southward motion of the plume has moved the region of intense ionization structure south of the propagation path from the DSCS satellite. The resulting signal structure is shown in Figure 3-12.

Figures 3-10 and 3-11 illustrate an important point — once signal scintillation has saturated at a Rayleigh-like condition, the effect of more intense striation structure is to cause the signal to decorrelate more rapidly in the receiver plane. Larger values of σ_ϕ no longer affect first-order amplitude statistics but continue to decrease the signal correlation length. Both calculations have S_4 scintillation indices of approximately unity. The difference lies in the signal fading rate, as seen by the "noisier" appearance of the signal structure in Figure 3-11. Therefore, in regions of intense Rayleigh scintillation, signal structures

can be characterized by the signal correlation time τ_o* and link performance can be calculated in terms of this parameter.

With the above result in mind, an additional MPS calculation was performed for intense, saturated scintillation conditions. The resulting representations of signal structure were used to evaluate the performance of the DSCS AN/USC-28 modem in severe scintillation. The striations were assumed to be uniformly distributed in a 1000 km thick striated region whose center was located 1500 km from the receiver plane. The outer scale was again taken as 1 km, σ_ϕ was taken as 30 radians, and 16,384 points were used in the 17 km long MPS grid. The resulting scintillation index measured by averaging over all realizations is 1.06. The signal correlation length measured in similar fashion is 24 m.

Figure 3-13 shows a portion of one realization of signal amplitude and phase obtained for this case. The time scale was obtained by using an effective velocity of 24 m/sec. Thus the value of the signal correlation time in this example is 1 sec. This signal realization (and other statistically similar realizations generated by the same MPS calculation) is useful as a representation of a severely disturbed Rayleigh-like signal and may be used with more than one effective velocity to obtain receiver performance results as a function of τ_o. In addition to evaluating performance on the Landstuhl link we have used this approach to provide a more general evaluation of link performance. The results, presented in Section 4, demonstrate that link performance is a sensitive function of the signal fading rate.

3.2.2 Spatial Extent and Fading Rates

The spatial extent of regions of intense scintillation was estimated for DSCS II links based on the calculated values of σ_ϕ and propagation geometry from the MICE/MELT phenomenology simulation for representative

---

* Under very intense scintillation conditions frequency selective effects may become significant. This complicates the characterization of the signal structure. Treatment of frequency selective fading is beyond the scope of the current effort. However, based on other work we do not expect that frequency selectivity would substantially affect the results for the DSCS links considered in this analysis.

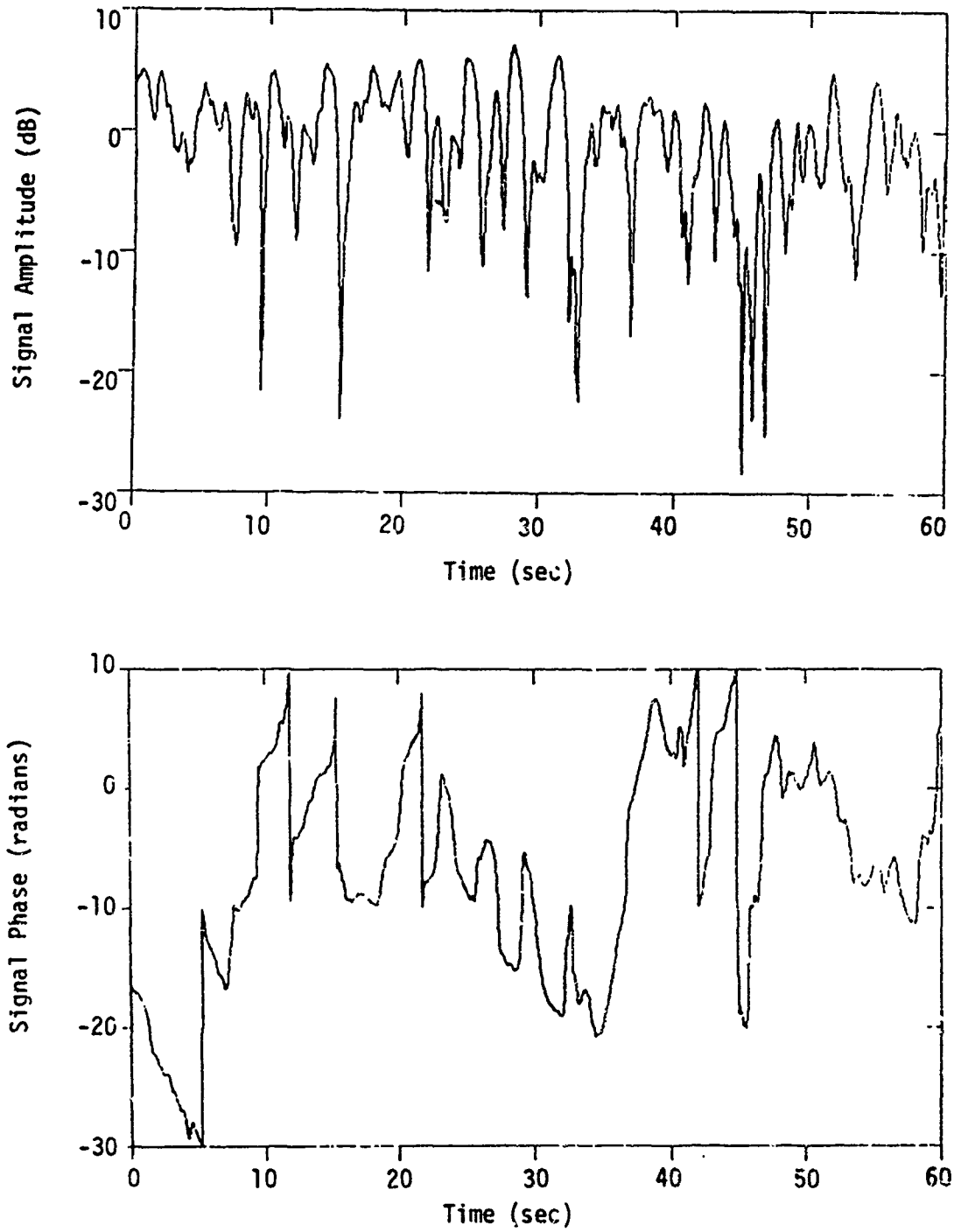

Figure 3-13. Signal amplitude and phase for intense, Rayleigh scintillation.

propagation paths and previously generated, parametric MPS calculations. The results for times of 20, 40, and 60 minutes after detonation are illustrated by the dashed contour on the maps presented in Figures 3-14 through 3-16. Saturated, Rayleigh scintillation is expected to occur on links from the DSCS Atlantic satellite to terminals located within the regions shown.* At 10 minutes after detonation the ionization structure has not developed sufficiently to produce a significant Rayleigh fading region so no figure is shown for this case.

Contours of signal correlation time, τ_o, illustrating scintillation fading rates within the Rayleigh regions are also shown on Figures 3-14 through 3-16. The importance of the scintillation rate was discussed previously and is demonstrated further by the modem performance results in Sections 4.3 and 4.4. The signal correlation time contours shown were calculated using striation structural parameters and effective velocities from the MICE/MELT simulation and analytical expressions for the signal correlation length derived as follows.

For the case of plane-wave propagation in a direction normal to the striation axes, the electric field autocorrelation function is given by

$$R_E(x) = \exp\{-\sigma_\phi^2[1 - R_\phi(x)]\} \quad . \tag{3-7}$$

This relationship is derived in Reference 3-15 for the case of gaussian electron density fluctuations, and also in Reference 3-16 under the Markov assumption and thus appears to be useful in general. The phase autocorrelation function corresponding to the PSD of Equation 3-2 is

$$R_\phi(x) = \frac{x}{L_o} \; K_1\left(\frac{x}{L_o}\right) \tag{3-8}$$

where K_1 is the modified Bessel function (Reference 3-17, p. 374). Thus one can easily solve numerically for the value of the signal correlation length ℓ_o such that $R_E(\ell_o) = e^{-1}$.

* Less severe scintillation occurs outside the Rayleigh boundary.

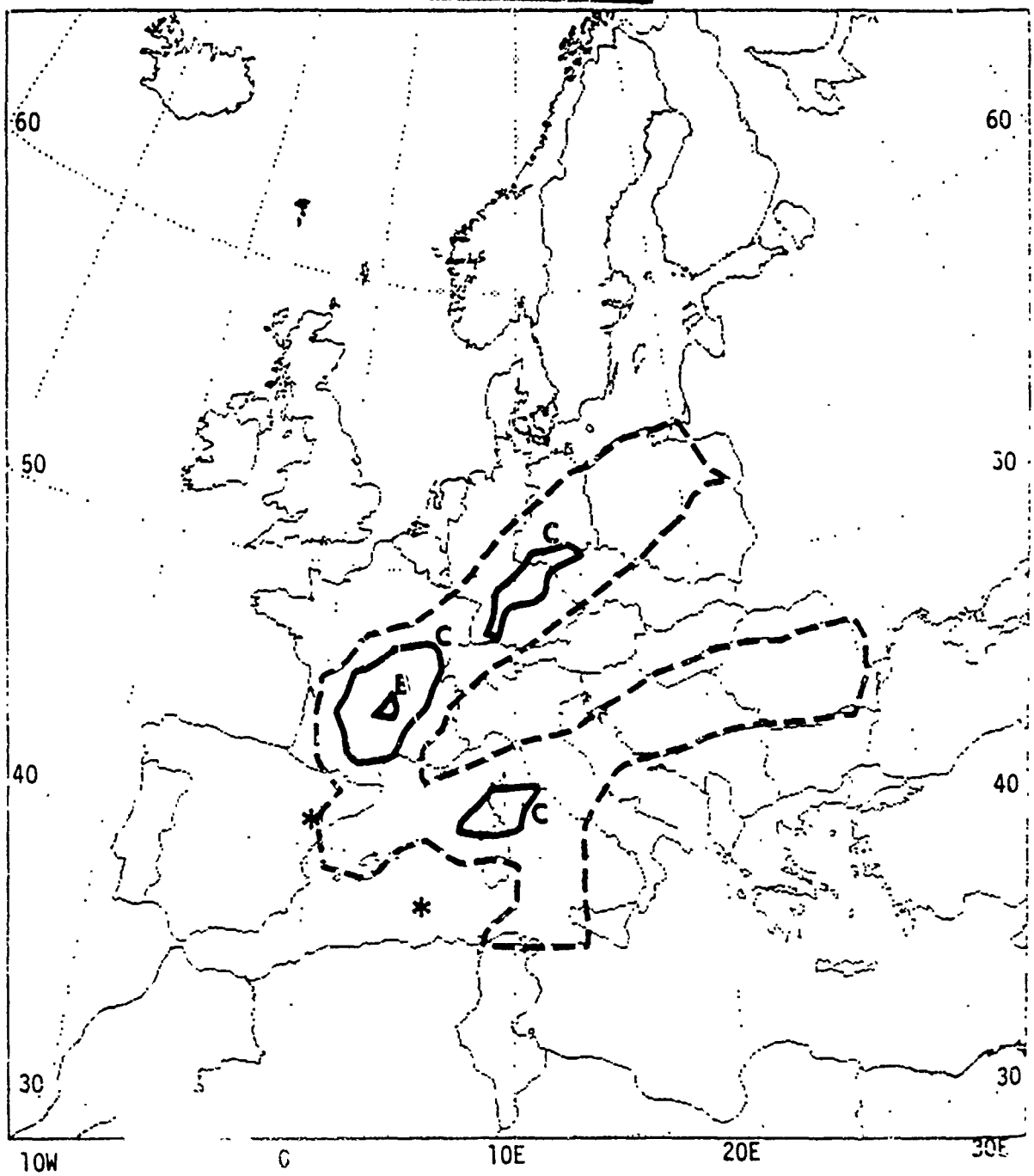

Contour values: B = 0.1, C = 0.3 seconds.

Figure 3-14. Extent of intense, Rayleigh scintillation and contours of correlation time at 20 minutes.

[redacted]

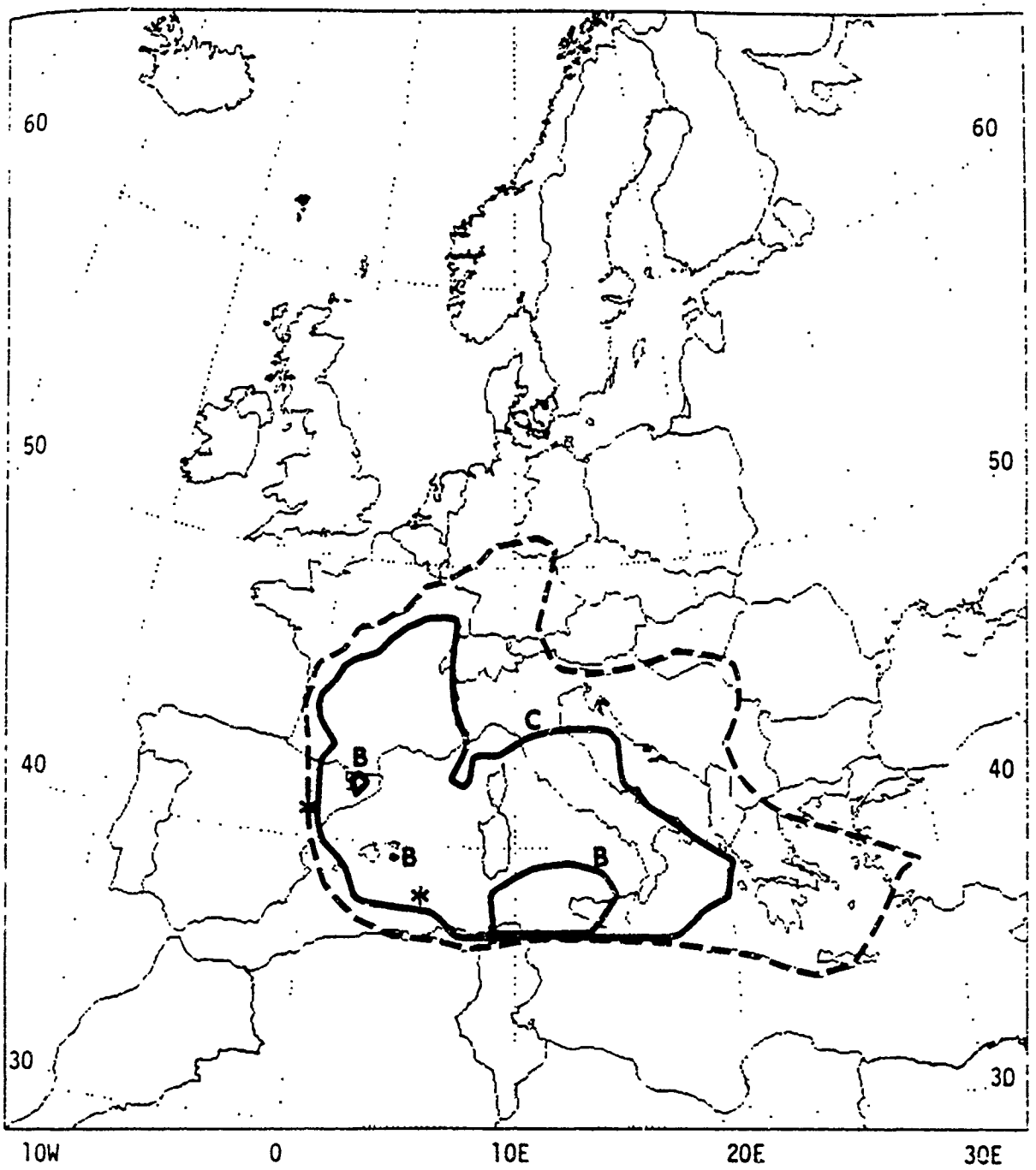

Contour values: B = 0.1, C = 0.3 seconds.

Figure 3-15. Extent of intense, Rayleigh scintillation and contours of correlation time at 30 minutes.

[redacted]

[redacted]

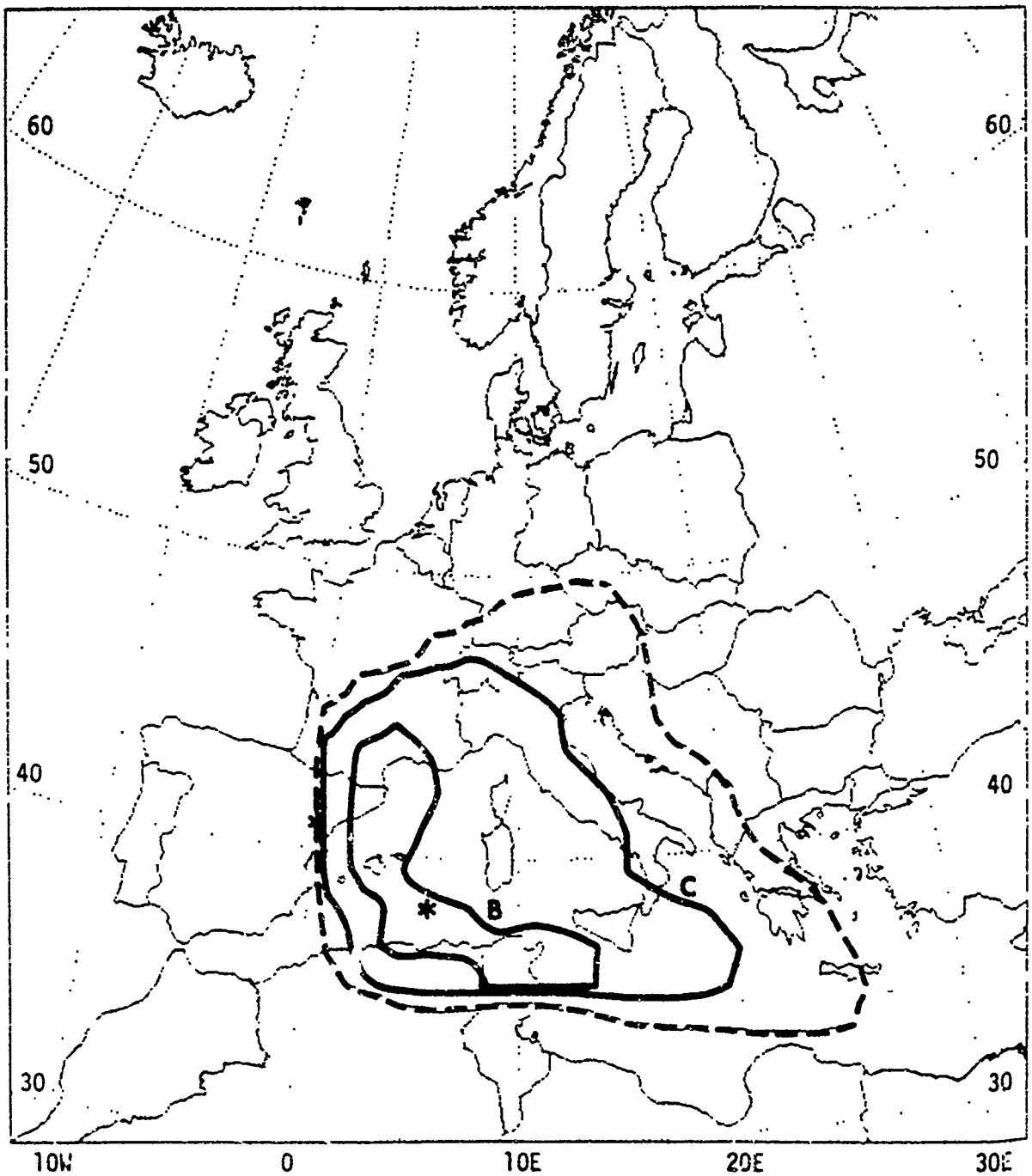

Contour values: B = 0.1, C = 0.3 seconds.

Figure 3-16. Extent of intense, Rayleigh scintillation and contours of correlation time at one hour.

[redacted]

[redacted]

Signal correlation length ℓ_o is shown as a function of phase standard deviation, σ_ϕ, in Figure 3-17. The signal intensity correlation length ℓ_I is also shown on Figure 3-17. The intensity correlation length is the e^{-1} point of the spatial autocovariance function of signal intensity, ($I = EE^*$) and provides a direct measure of the amplitude fading rate. In Rayleigh scintillation conditions the intensity autocovariance function is equal to the square of the autocorrelation function of the complex electric field. Therefore, for the autocorrelation function $R_E(x)$ in Equation 3-7, and Rayleigh statistics, the intensity correlation length is just a square root of two smaller than the electric field correlation length ℓ_o.

Examination of the results in Figures 3-14 through 3-16 shows that the Rayleigh fading regions are very large, particularly at the late calculation times. In this scenario, intense scintillation effects are predicted in an area approaching about 4 million square kilometers in Southern Europe and the Mediterranean region at an hour after detonation. Note that Landstuhl lies within the Rayleigh "footprint" at 20 and 30 minutes after detonation, but by 60 minutes the region of intense scintillation has moved south of Landstuhl (49.25 °N Lat, 7.35 °E Lon). The southward motion at late times reflects the action of gravitational forces on the high altitude plume.

Overall, values of τ_o vary from about 0.75 seconds to somewhat less than 0.1 sec for a stationary observer, with regions of shorter decorrelation time more widespread at later times when the striation structure is more fully developed. Again we caution the reader that ambient winds are not included in the calculation of effective velocities and hence correlation times. If ambient winds were included the values of τ_o shown could be reduced by a factor of two to three. The range of signal correlation lengths calculated in this scenario is from the order of 10 meters to about 75 meters. A reasonable range of velocities to consider including natural wind motion is from a few tens of meters per second to

[redacted]

[redacted]

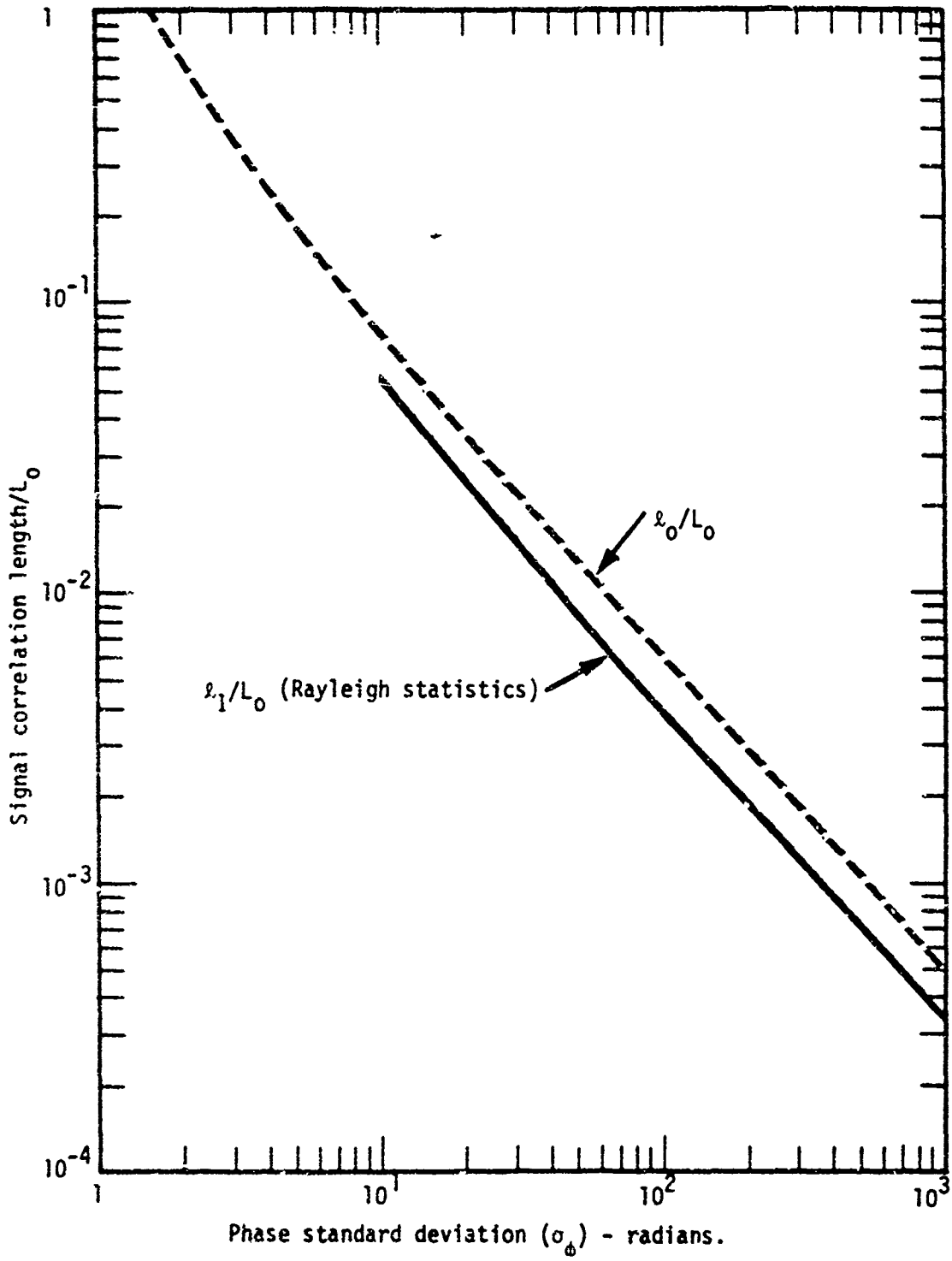

Figure 3-17. Signal correlation length versus phase standard deviation.

[redacted]

several hundred meters per second. Thus a likely range of signal correlation times for fixed links in this scenario is from a few hundredths of a second to several seconds. For airborne receivers, fading rates could be even faster with correlation times of about 0.01 seconds or less.

Figure 3-18 contains a Rayleigh footprint and signal correlation time contours calculated at 60 minutes after detonation with the ad hoc assumption that all the plume ionization is contained in striations; i.e., $\Delta N_e = \langle N_e \rangle$ where ΔN_e is the electron density fluctuation due to striations (see Section 2.2.1) and $\langle N_e \rangle$ is the mean plume electron density calculated in the MELT simulation. Comparison of Figure 3-18 with Figure 3-16, which is based on the linear striation analysis, illustrates potential effects of nonlinear striation formation on the previous results.* The fully striated example in Figure 3-18 is in some sense a "worst case" estimate of scintillation effects at this time. The Rayleigh footprint is somewhat larger in this example and the minimum signal correlation time is about a factor of 3 smaller.

---

* Striation evolution at very late times (several hours) is very uncertain. Nonlinear processes are generally believed to result in striation bifurcation which may cause a cascade to extremely small striation sizes. It is not clear if the fine scale striations rapidly diffuse away thereby reducing the electron density variance, or if they persist, keeping the variance high, reducing the outer scale size, and generally increasing scintillation effects (Reference 3-18).

[redacted]

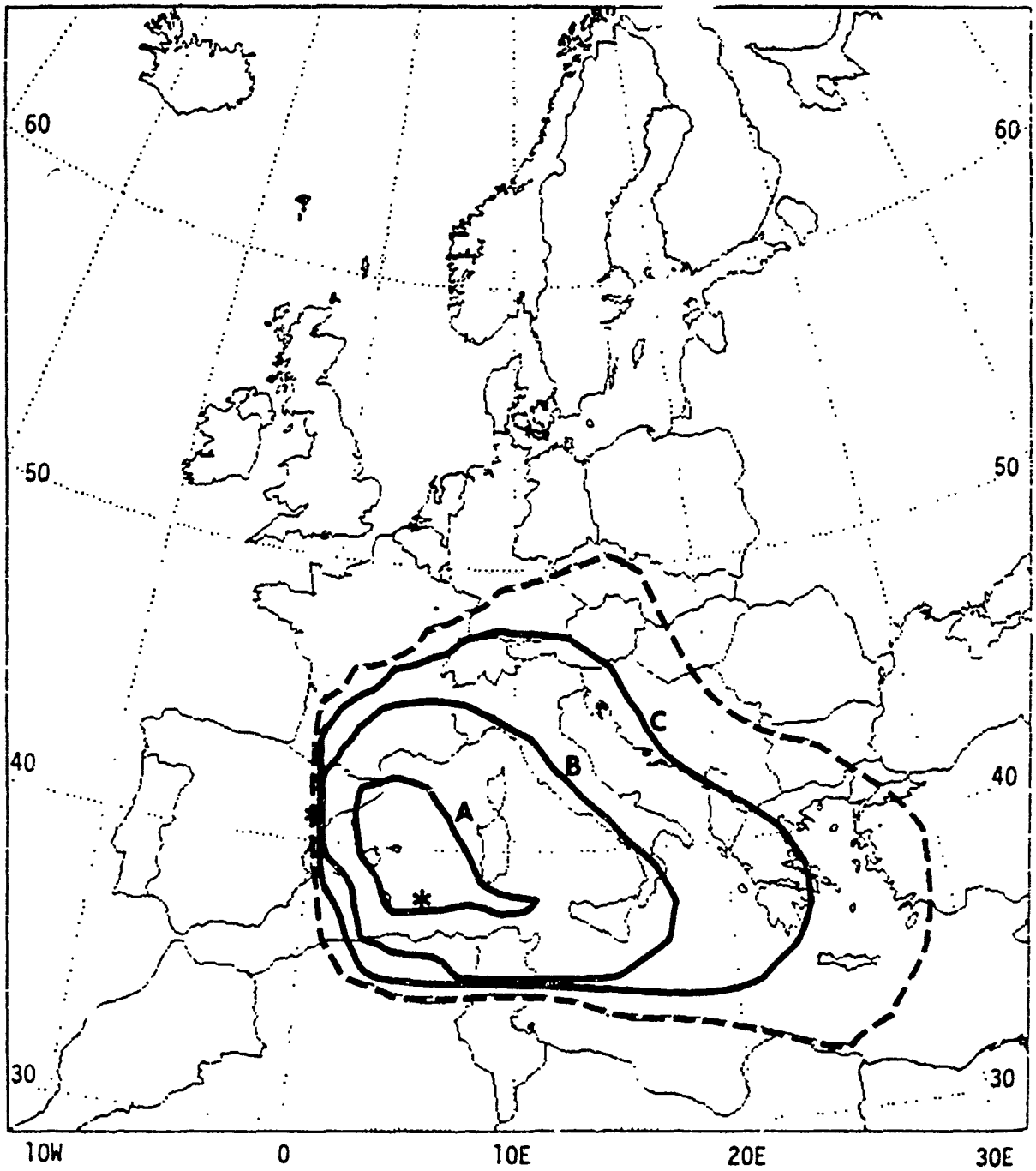

Contour values: A = 0.03, B = 0.1, C = 0.3 seconds.

Figure 3-18. Extent of intense Rayleigh scintillation and contours of correlation time at one hour for a fully striated plume.

[redacted]

[redacted]

SECTION 4
LINK PERFORMANCE ANALYSIS

In this section, the multiple phase screen (MPS) propagation calculations described in Section 3 are used as input to a digital simulation of the AN/USC-28 spread spectrum modem to obtain link performance characteristics for the dual burst scenario. General results are presented as plots of binary error rates as a function of the mean bit energy-to-noise density ratio (E_t/N_o) with the signal correlation time, τ_o, treated parametrically. This treatment allows calculation of contours of binary error rate superimposed on a map of Europe to clearly delineate regions where link degradation occurs.

Also presented are examples of demodulator operation as a function of time, including phase and frequency tracking errors and conditional binary error probabilities to graphically illustrate the effects of signal scintillation on receiver performance.

4.1 DSCS II AN/USC-28 MODEM SIMULATION

For this work, the general digital simulation developed at MRC (Reference 4-1) to model several types of phase-shift keyed modems was utilized to model the AN/USC-28 modem.

The modem simulation used here is a direct sampled-data digital implementation of the AN/USC-28 modem and includes implementation of the Costas phase tracking loop, the AGC circuit, coherent data demodulation and differential encoding and decoding. This digital simulation approach

[redacted]

is the only practical method of correctly treating the nonlinearities inherent in coherent PSK demodulators. For example, the phase-lock loop (PLL), which is the heart of these demodulators, can be described mathematically by a nonlinear stochastic integrodifferential equation. This equation cannot be solved by conventional analytical techniques except for a very few simplified limiting situations. However, the nonlinear operation of the PLL can be represented to a high degree of precision by straightforward finite difference techniques. Similarly, the nonlinear operation of the AGC and other receiver elements can be readily simulated numerically.

Figure 4-1 shows a schematic diagram of the BPSK demodulator configuration which represents the basic modulation technique of the AN/USC-28 modem.* The basic element of this demodulator is a modified Costas (I-Q) phase-lock loop.

As illustrated in Figure 4-1, the input signal plus noise is passed through an intermediate frequency (IF) bandpass filter preceding the phase-lock loop demodulator. (In practice there are several RF and IF stages in a receiver, and the bandpass filter shown in Figure 4-1 represents their combined effect.) The input is then amplified in a voltage-controlled amplifier whose gain is controlled by the output of an automatic gain control (AGC) circuit. The AGC circuit, not explicitly shown in Figure 4-1, is required to hold the signal level near its design value at the demodulator input. It should be noted that AGC operation becomes increasingly important in the presence of signal amplitude and phase scintillation.

---

* In the AN/USC-28 modem, two binary data channels may be combined in phase quadrature to form quadriphase-shift keyed (QPSK) modulation.

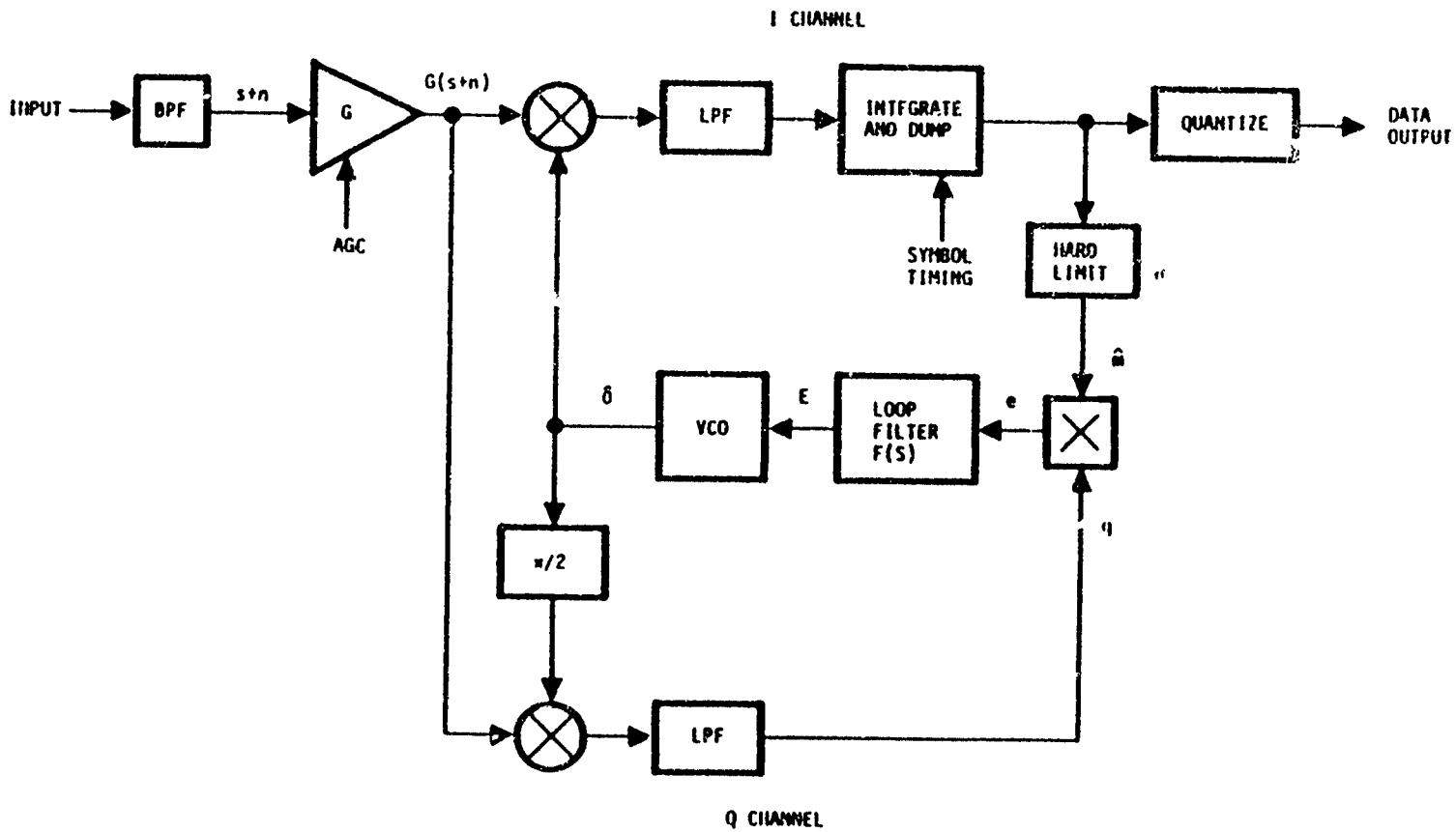

Figure 4-1. Functional diagram of the AN/USC-28 BPSK demodulator with modified Costas phase-lock loop.

The AGC-modified signal plus noise voltage is fed into two mixers, which produce inphase (I) and quadrature (Q) channels with respect to the local carrier reference from the voltage-controlled oscillator (VCO). The I and Q channel voltages are lowpass-filtered to remove double-frequency components and are then multiplied to remove the BPSK modulation and produce an error voltage at the Costas loop filter input. In the modified Costas loop shown in Figure 4-1, the inphase channel is passed through an integrate-and-dump data filter and then hard limited before multiplication with the quadrature channel.

The nonlinear operation of multiplication of the quadrature channel with the hard-limited inphase channel produces a voltage that ideally is proportional to the sine of the phase error between the incoming signal carrier and the locally generated reference carrier from the VCO. This error voltage is contaminated by noise and is smoothed by the Costas loop filter. The loop filter output drives the VCO, thereby providing the feedback path that closes the phase-lock loop.

The VCO output frequency is proportional to the smoothed input error voltage from the loop filter. The error voltage is positive when the VCO phase lags the incoming carrier phase, and vice versa. Thus, the loop causes the VCO frequency and phase to change in the direction required to drive the error toward zero. If the signal-to-noise ratio is sufficiently large, and if the signal carrier phase is not varying too rapidly, the loop will pull into phase lock.

Under favorable conditions when the loop has acquired phase lock, the VCO frequency and phase closely track the incoming signal carrier frequency and phase within some tolerance determined by loop design parameters and signal properties. The biphase data modulation then appears at the output of the integrate-and-dump circuit, with the polarity of this output providing the estimate of the binary symbol or data bit.

There are several known simplifications in the demodulator simulation model, of which the reader should be aware. These are listed below:

1. Pseudonoise (PN) direct-sequence spread spectrum code acquisition and tracking loops are not included in the receiver model presented here. Thus, perfect PN code tracking is assumed.

2. Bit timing synchronization and tracking loops are not included. Thus, perfect bit synchronization is assumed.

3. Frequency acquisition aiding of the carrier tracking loop is not included here.

The most potentially significant omission concerns PN code tracking, as it can affect the performance of the AN/USC-28 spread spectrum modem. Code correlation losses can be estimated externally to the simulation models, and the effect approximated by reducing the mean carrier power-to-noise density ratio (C/N_o) in the simulation (provided the code correlation function is relatively undistorted). However, accurate treatment of the effect of code tracking in a severe frequency selective environment would require implementation of the code tracking loop and reacquisition procedure in the simulation model. This is beyond the scope of the work reported here. Frequency selective effects are being investigated under other contracts. It is not expected that inclusion of these effects would substantially alter the results presented here.

Table 4-1 lists the simulation input parameters required to model the AN/USC-28 BPSK modem. The low data rate (75 bps) is important because all DSCS II links using spread spectrum modems will, as a minimum, support a 75 bps data rate (Reference 4-2). The AGC nominal carrier power-to-noise density ratio (C/N_o) is adjusted to be equal to the mean received value of C/N_o in each simulation. This is done here to reduce the AGC transient that occurs at the beginning of each simulation run. The range of mean received C/N_o and the corresponding mean bit energy-to-noise density (E_b/N_o) are chosen to give a wide range of data points applicable to many of the possible DSCS II link configurations as well as to correspond to

Table 4-1. AN/USC-28 modem design parameters.

Data bit rate	75 bps
Simulation sampling rate	300 sec^{-1}
IF bandwidth	300 Hz
PLL type	Modified Costas
PLL order	Third
PLL bandwidth	21 Hz
AGC type	Envelope
AGC time constants	0.1 sec
Mean received E_b/N_o	16-51 dB
Mean received C/N_o	35-70 dB-Hz

limitations imposed by phase tracking thresholds and reliable data demodulation thresholds.

4.2 MODEM PERFORMANCE EXAMPLES

Before presenting more general summaries of link performance results, two specific examples of the BPSK AN/USC-28 modem operation are described in this section. These examples graphically illustrate some of the characteristics of phase-lock loop demodulator operation under signal scintillation conditions.

Both examples utilize the same MPS realization (described in Section 3.2.1) of signal amplitude and phase. The first example, with a signal correlation time, τ_o, of 1.0 sec is an amplitude dominated case where phase tracking errors are caused by signal fades below the phase tracking threshold. The second example, with a factor of 10 faster signal correlation time, describes a situation where both amplitude and phase scintillations are important.

4.2.1 Example 1: Amplitude Dominated Situation

Figures 4-2 and 4-3 show the signal amplitude and phase from an MPS realization calculated for a power-law K^{-3} phase PSD with an outer scale size of 1 km and a phase standard deviation (σ_ϕ) of 30 radians. The signal correlation time is 1.0 sec, which is determined from the signal correlation distance (measured as 23.7 m) divided by the effective velocity (chosen as 23.7 m/sec). A total simulation time of 120 seconds was used for this example; only 60 sec of data is shown on plots in this section to keep the figures readable. The measured S_4 scintillation index for the entire 120 sec interval is 0.87 and the signal phase standard deviation is 11.8 radians. The signal amplitude scale in Figure 4-2 is decibels relative to the mean value. The signal phase scale in Figure 4-3 extends from -2π to 2π radians. In plotting Figure 4-3, 2π was added to or subtracted from all succeeding phase values whenever the plotted phase otherwise would have been outside the -2π to 2π plotting boundary. The sharp discontinuities shown in Figure 4-3 are the result of the addition of these 2π shifts and affect only the plotted phase, not the simulation.

The mean value of the carrier power-to-noise density ratio (C/N_o) in this (and the next) example is 45 dB-Hz, which at the 75 bps data rate corresponds to a mean bit energy-to-noise density (E_b/N_o) of 26.25 dB.

The modified Costas loop BPSK demodulator of this example is analyzed and described in detail in Section 3.3 of Reference 4-1. Simulation results there show that the phase tracking threshold for this type of demodulator with a 21 Hz PLL bandwidth is around 25 to 26 dB-Hz. This is the value of C/N_o at which the loop begins to exhibit phase slipping with undisturbed steady (constant) signal plus noise conditions. This phase tracking threshold is about 19 dB below the mean level of C/N_o in this example, as indicated by the dashed line in Figure 4-2.

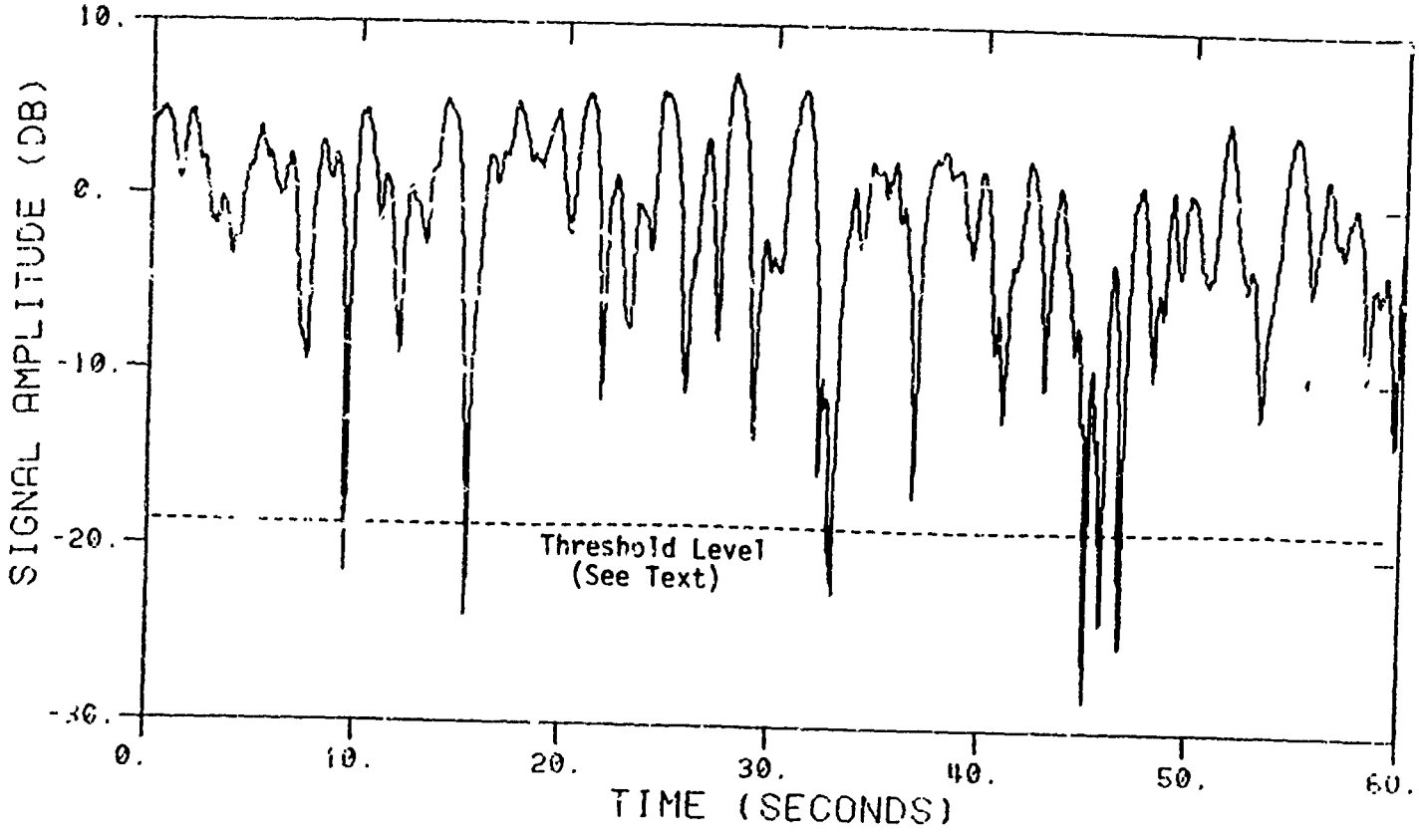

Figure 4-2. Example 1: Signal amplitude versus time, τ_0 = 1.0 sec.

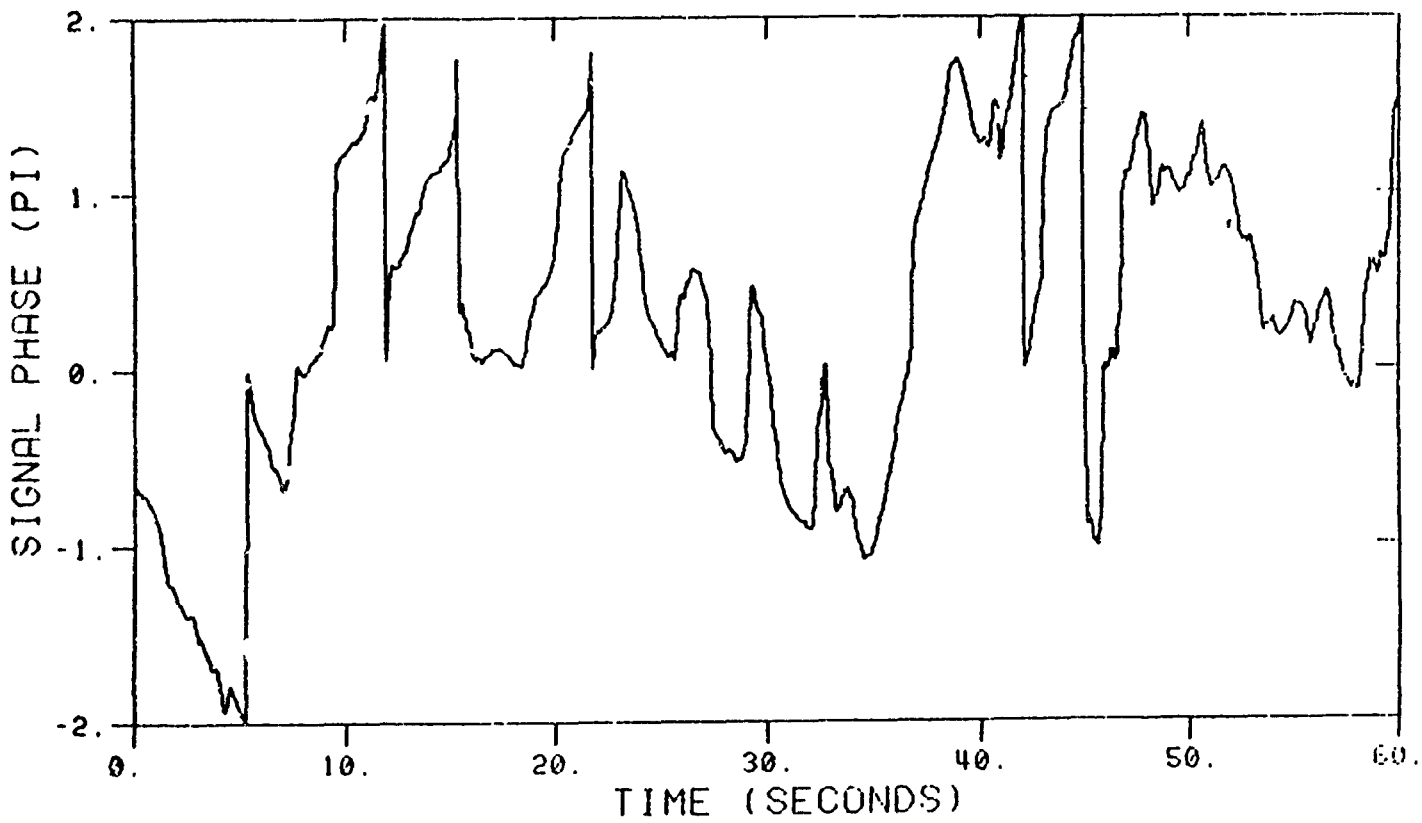

Figure 4-3. Example 1: Signal phase versus time, τ_0 = 1.0 sec.

[redacted]

Following Reference 4-1, define the data demodulation threshold as the signal-to-noise ratio for which the conditional binary error probability is 10^{-3}. From Figure 3-5 of Reference 4-1, this error probability occurs at $E_b/N_o = 7.33$ dB for differentially encoded coherent BPSK. This value corresponds to $C/N_o = 26$ dB-Hz at the 75 bps data rate. Thus the data demodulation threshold and the phase tracking threshold occur at essentially the same input signal level for the AN/USC-28 modem operating at 75 bps.

From Figure 4-2 it is seen that the signal amplitude drops near or below the threshold line only a few times during the 60 second interval shown. From Figure 4-3 it is also apparent that the signal phase variations are slow, and it will be seen that the PLL can track the phase quite well.

Figure 4-4 shows the phase tracking error time history for this example. The ordinate scale extends from -6 to 6 radians to include three adjacent equilibrium phase tracking states at 0 and $\pm\pi$ radians. It is seen that the 24 dB fade at 15 seconds and the 29 dB fade at 45 seconds both cause temporary loss of phase lock. The phase slips to adjacent phase tracking states shown in Figure 4-4 correlate quite well with signal fades in Figure 4-2 which approach close to or fall below the phase tracking threshold. The excellent correlation of signal fades with periods of noisy track and phase slips, or loss of lock, is indicative of an amplitude-dominated case, with amplitude fades presenting the only significant problem to the phase-lock loop in this slow fading example.

[redacted]

DCA (6)(1)

[redacted]

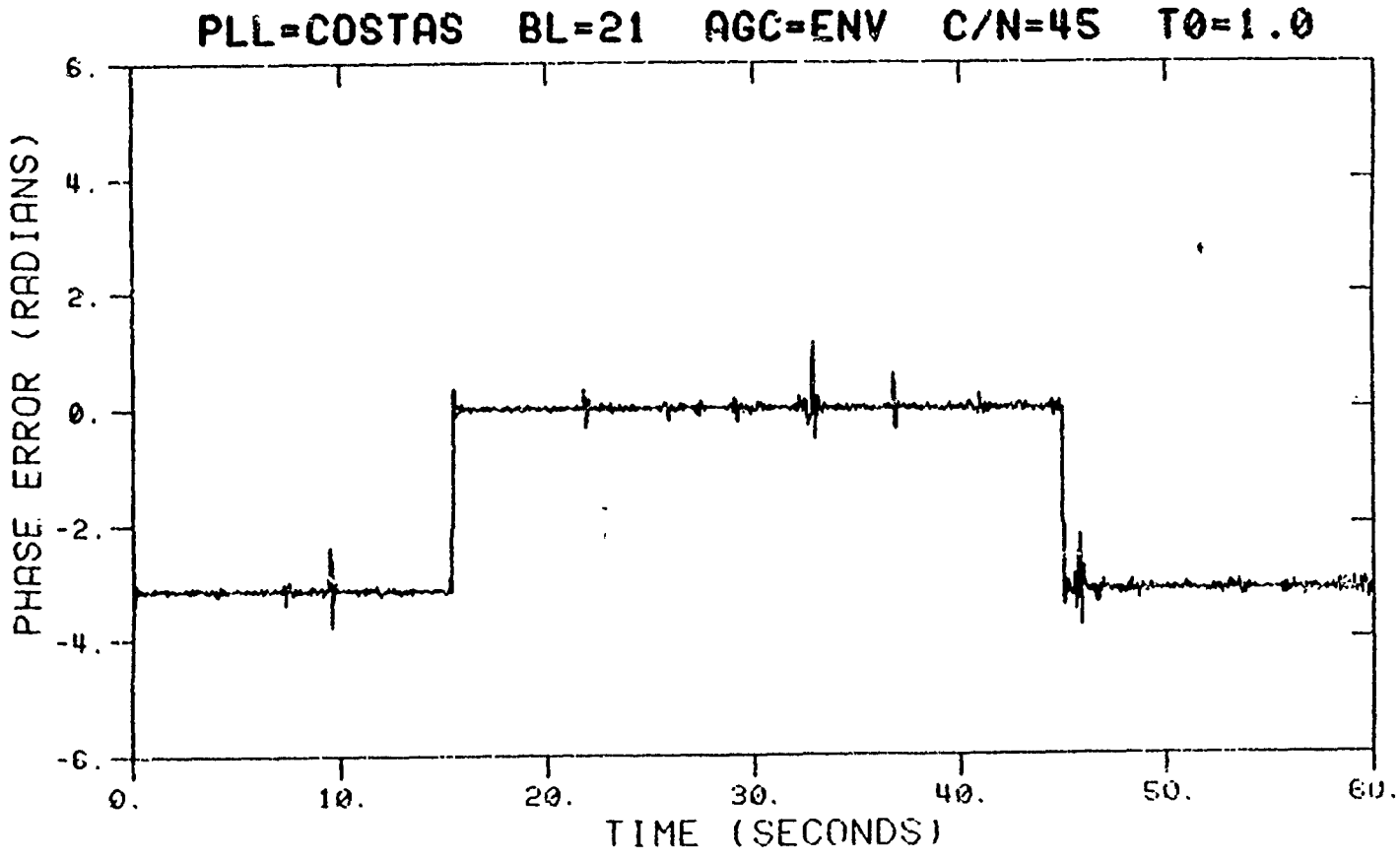

Figure 4-4. Example 1: Phase tracking error history, C/N_0 = 45 dB-Hz, τ_0 = 1.0 sec.

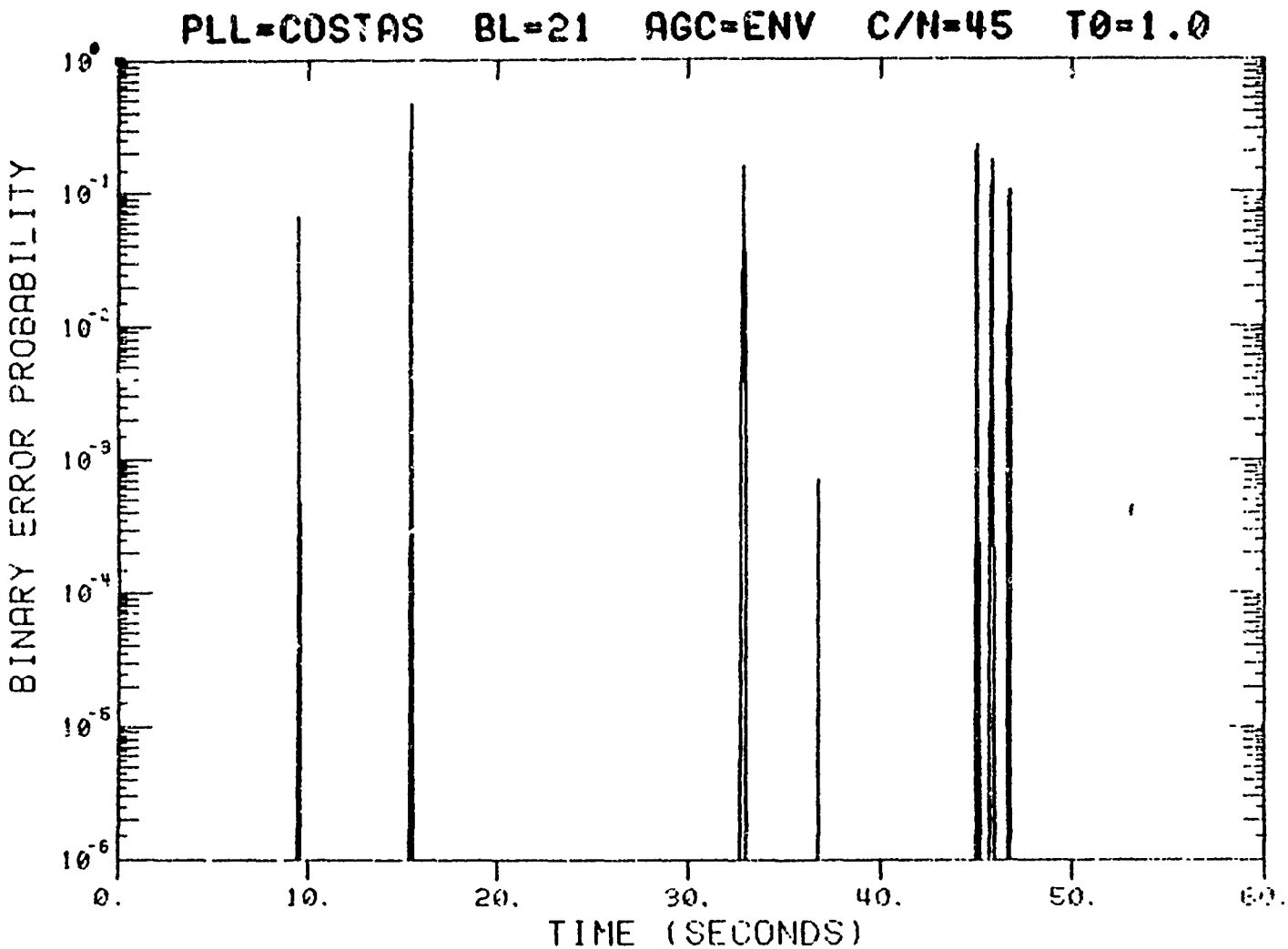

Figure 4-5. Example 1: Conditional binary error time history, C/N_0 = 45 dB-Hz, τ_0 = 1.0 sec.

[redacted]

[redacted]

DCA (b)(1)

[redacted]

[redacted]

Figure 4-6 illustrates the frequency tracking error history for this case. Again the occurrences of deep signal amplitude fades coincide with large transient frequency errors. Note the "spiky" appearance of the frequency error time history, typical of intense scintillation conditions. The very rough frequency track from 45 to 47 seconds in the figure coincides with three deep fades of the input signal.

[redacted]

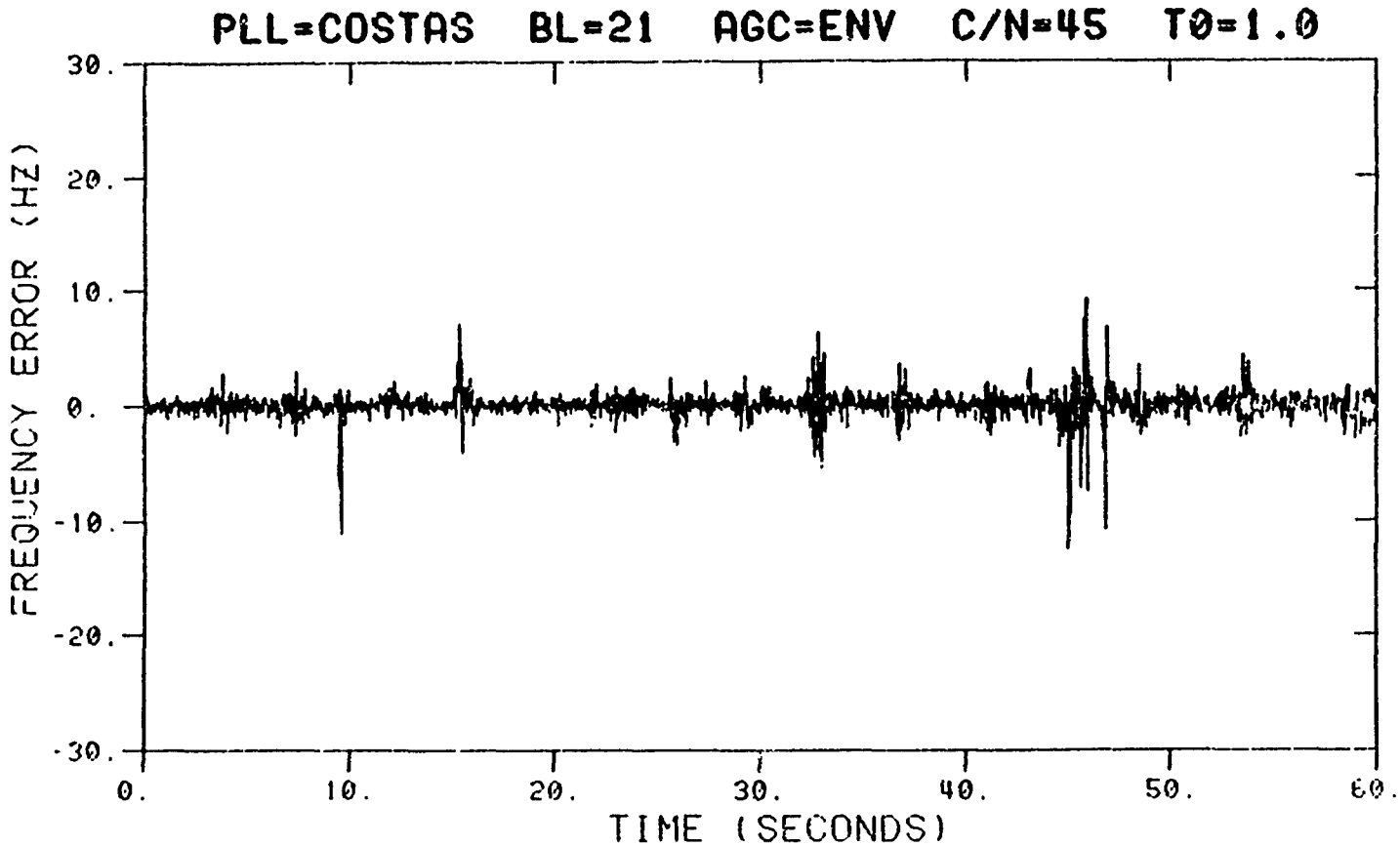

Figure 4-6. Example 1: Frequency tracking error time history, C/N_0 = 45 dB-Hz, τ_0 = 1.0 sec.

Figure 4-7 shows the AGC gain versus time for this example. Ideally, the AGC gain should look just like the input signal amplitude plotted upside down. Except for the inability to follow the very deep fades and some smoothing of the more rapid amplitude variations, this is the case here. Note that the failure of the AGC to track the very deep fades is not a result of dynamic range limiting or noise clipping. Rather, because of the very short duration of the deepest signal fades, the 0.1 second time constant AGC can never quite compensate for them. The AGC response necessarily lags the signal amplitude fluctuations, and in the deepest fades the signal level begins to recover before the AGC gain reaches the peak value it was approaching.

An interesting simulation output is the demodulated received message. In this example, the transmitted message is simply a repetition of the following line of text:

3RD-ORDER MODIFIED COSTAS PLL DEMODULATOR, OPERATION DURING SIGNAL SCINTILLATION

Each character of the transmitted message is converted to binary form using the 7-bit ASCII character code, then differentially encoded and biphase-modulated onto the signal carrier. During the 120-second time period of this example, the above message line was repetitively transmitted at the 75 bps modulation rate until the simulation run was terminated near the end of the seventeenth repetition. A carriage return and line feed character, not shown above, was also transmitted at the end of each line. The received message, after coherent demodulation, differential decoding, and reformatting into ASCII characters, is shown in Figure 4-8 for this 120-second simulation example.

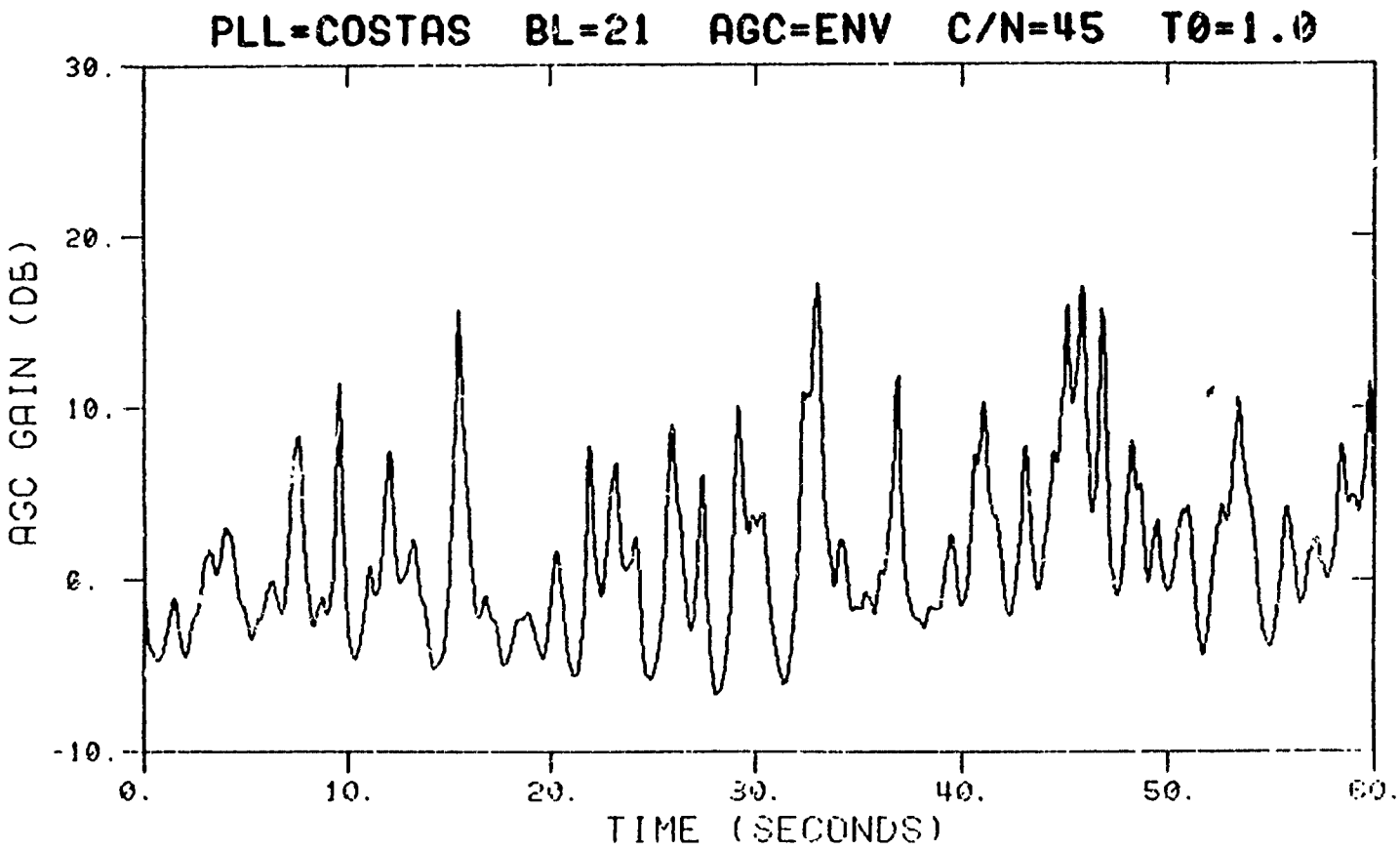

Figure 4-7. Example 1: AGC gain versus time, C/N_0 = 45 dB-Hz, τ_0 = 1.0 sec.

DCA (b)(1)

[redacted]

Figure 4-8. Example 1: Simulated received message for AN/USC-28 modem, τ_0 = 1.0 sec, C/N_0 = 45 dB-Hz.

DCA (b)(1)

[redacted]

4.2.2 Example 2: Amplitude and Phase Both Important

The second example presented here involves the same MPS signal as the preceding example, except that the signal correlation time, τ_0, is smaller. The signal correlation time is reduced from 1.0 sec in the previous example to 0.1 second in this example. Thus the duration of all amplitude fades is shortened, and both amplitude and phase scintillation are important disturbances to demodulator operation.

Figures 4-2 and 4-3 again show the input signal amplitude and phase, but the abscissa scale has to be reduced by a factor of 10. Thus the plotted time for this example only extends to 6 sec rather than 60 sec

[redacted]

[redacted]

as shown in Figures 4-2 and 4-3. The mean C/N_o as well as the first order signal amplitude and phase statistics are identical to Example 1; only the second order signal statistics have changed.

Figure 4-9 shows the phase tracking error history for this example. Comparison of this figure with Figure 4-4 shows two major differences in phase tracking performance for the different scintillation rates. First, much larger phase errors occur in the presence of rapid scintillation than in the previous case, even when the signal amplitude is well above the PLL phase tracking threshold. Second, in contrast to the first example where only isolated phase slips occur during very deep fades, Figure 4-9 exhibits many additional phase slips during minor signal fades. These additional phase slips and noisier phase tracking are caused by signal phase fluctuations which are too rapid for the 21 Hz bandwidth PLL to track.

Figure 4-10 shows the corresponding frequency error time history for this case. Comparison with Figure 4-6 shows that frequency tracking is characterized by large transient errors and exhibits a spikier appearance for the shorter signal correlation time (faster scintillation).

The effect of a shorter signal correlation time on the AGC operation is illustrated by the AGC gain time history plotted in Figure 4-11. For this example, the AGC circuit with 0.1 sec time constant is unable to respond quickly enough to compensate for the more rapid signal amplitude fluctuations. Thus the AGC gain in Figure 4-11 is a low-pass filtered version of the input signal amplitude.

[redacted]

[redacted]

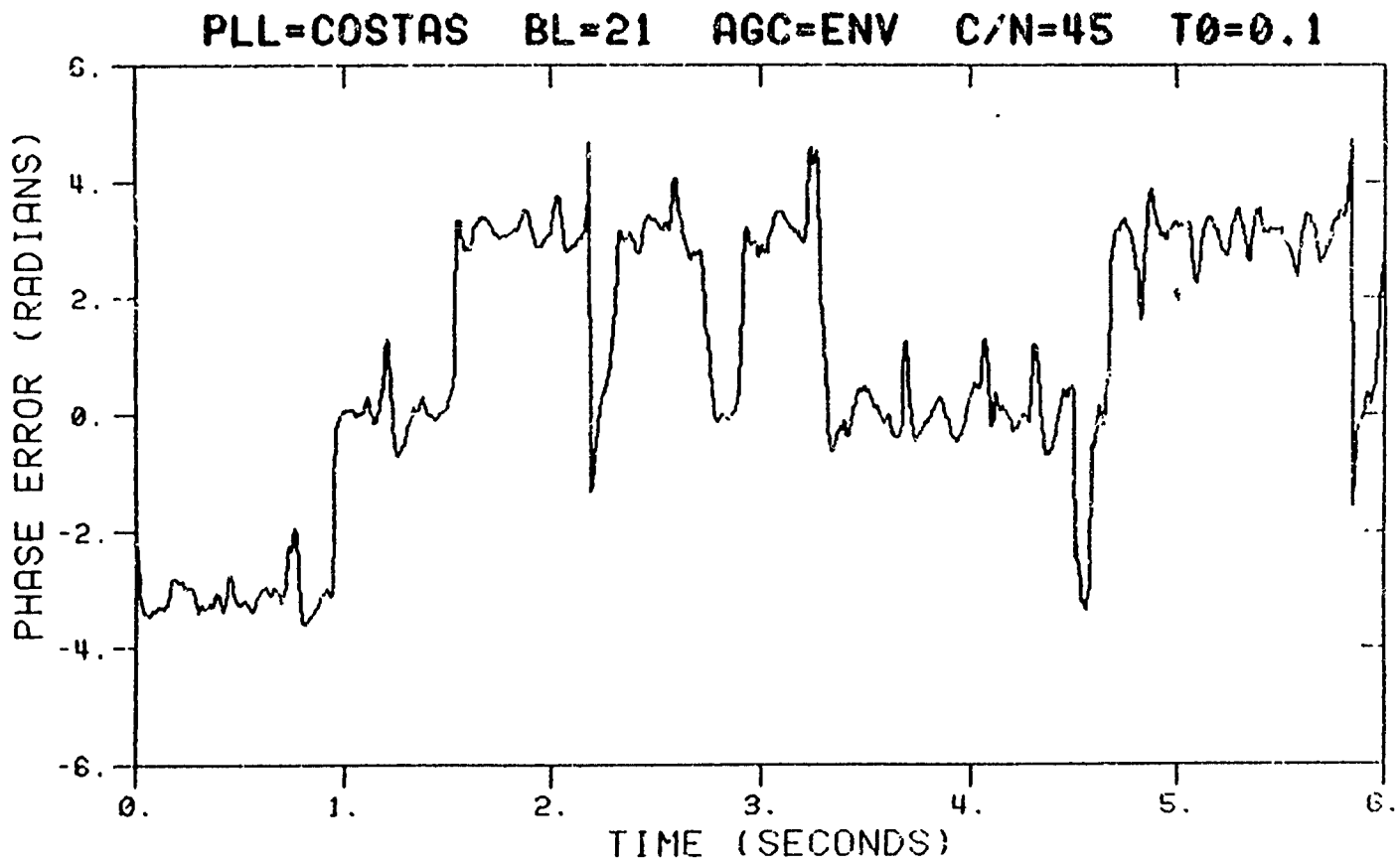

Figure 4-9. Example 2: Phase tracking error history, C/N_0 = 45 dB-Hz, τ_0 = 0.1 sec.

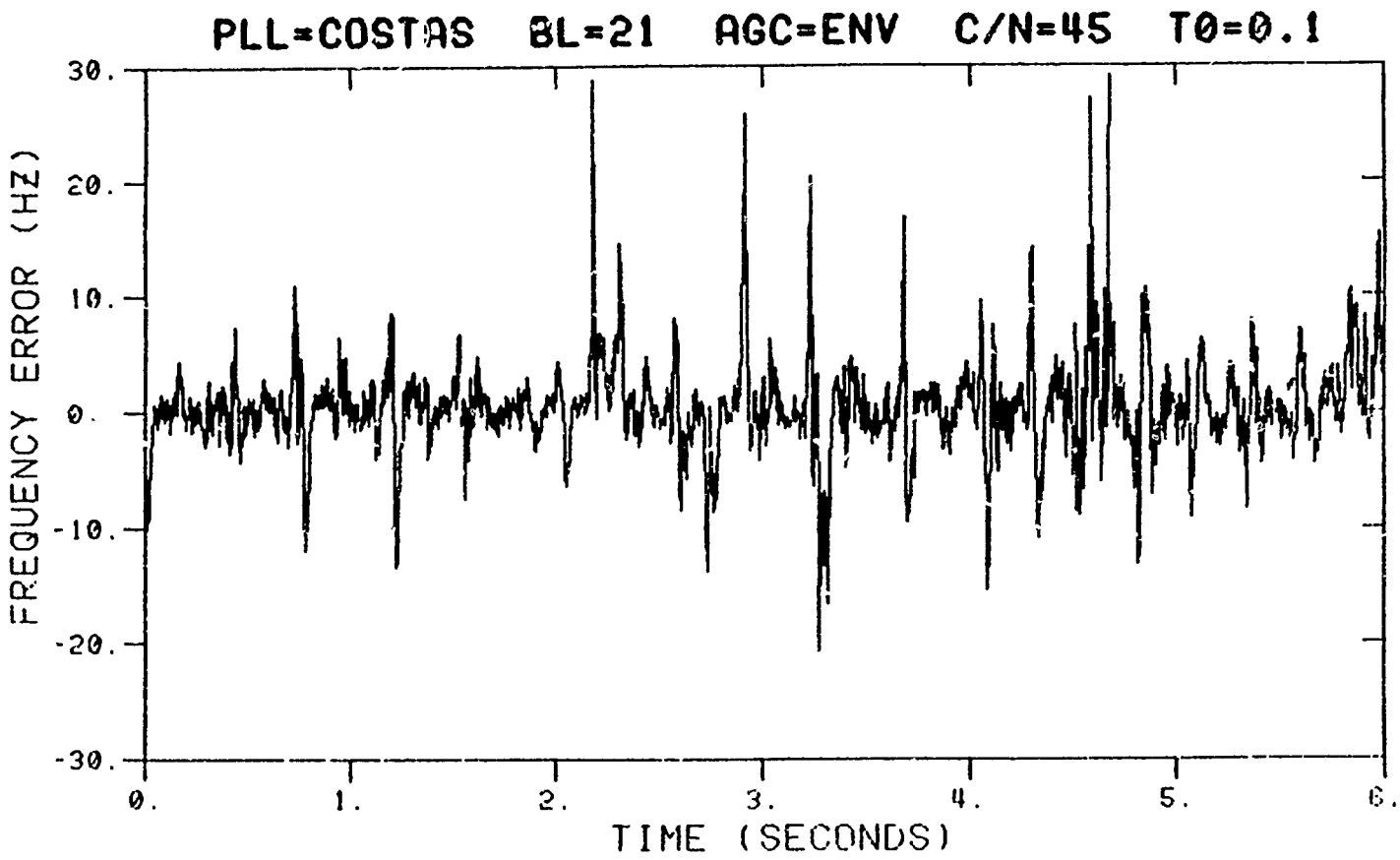

Figure 4-10. Example 2: Frequency tracking error time history, C/N_0 = 45 dB-Hz, τ_0 = 0.1 sec.

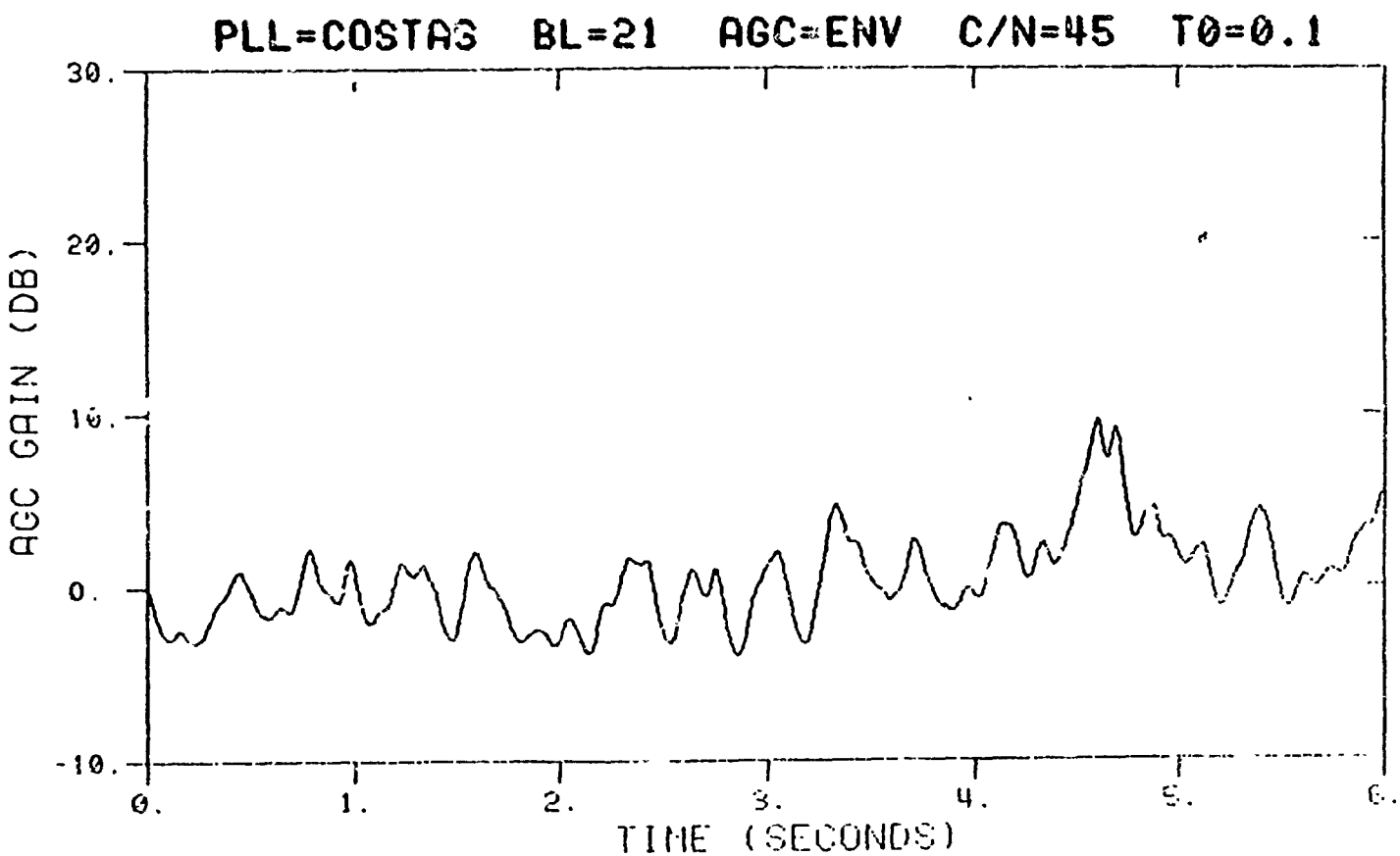

Figure 4-11. Example 2: AGC gain versus time, C/N_0 = 45 dB-Hz. τ_0 = 0.1 sec.

[redacted]

[redacted]

DCA (b)(1)

[redacted]

DCA (b)(1)

Figure 4-12. Example 2. Simulated received message for AN/USC-28 modem, τ_0 = 0.1 sec, C/N_0 = 45 dB-Hz.

4.3 LANDSTUHL LINK ANALYSIS

The preceding graphical examples illustrate some of the detailed interactions of signal scintillation on the DSCS II AN/USC-28 PSK modem. Additional simulations were performed for the different propagation conditions shown by the MPS calculations in Section 3.2.1 for a number of different values of the mean carrier power-to-noise density ratio (C/N_0). These simulation results are succinctly summarized in this section in terms of average binary error rates. While average error rates are a common and convenient method of summarizing communications link performance, the reader should note that such averages require careful interpretation in signal scintillation. For amplitude dominated conditions, errors almost always tend to occur in clumps or bursts and thus the error distribution is different than for normal signal plus noise conditions.

Figure 4-13 shows the average bit error rate expected on the link from the DSCS II Atlantic satellite to a fixed ground station at

[redacted]

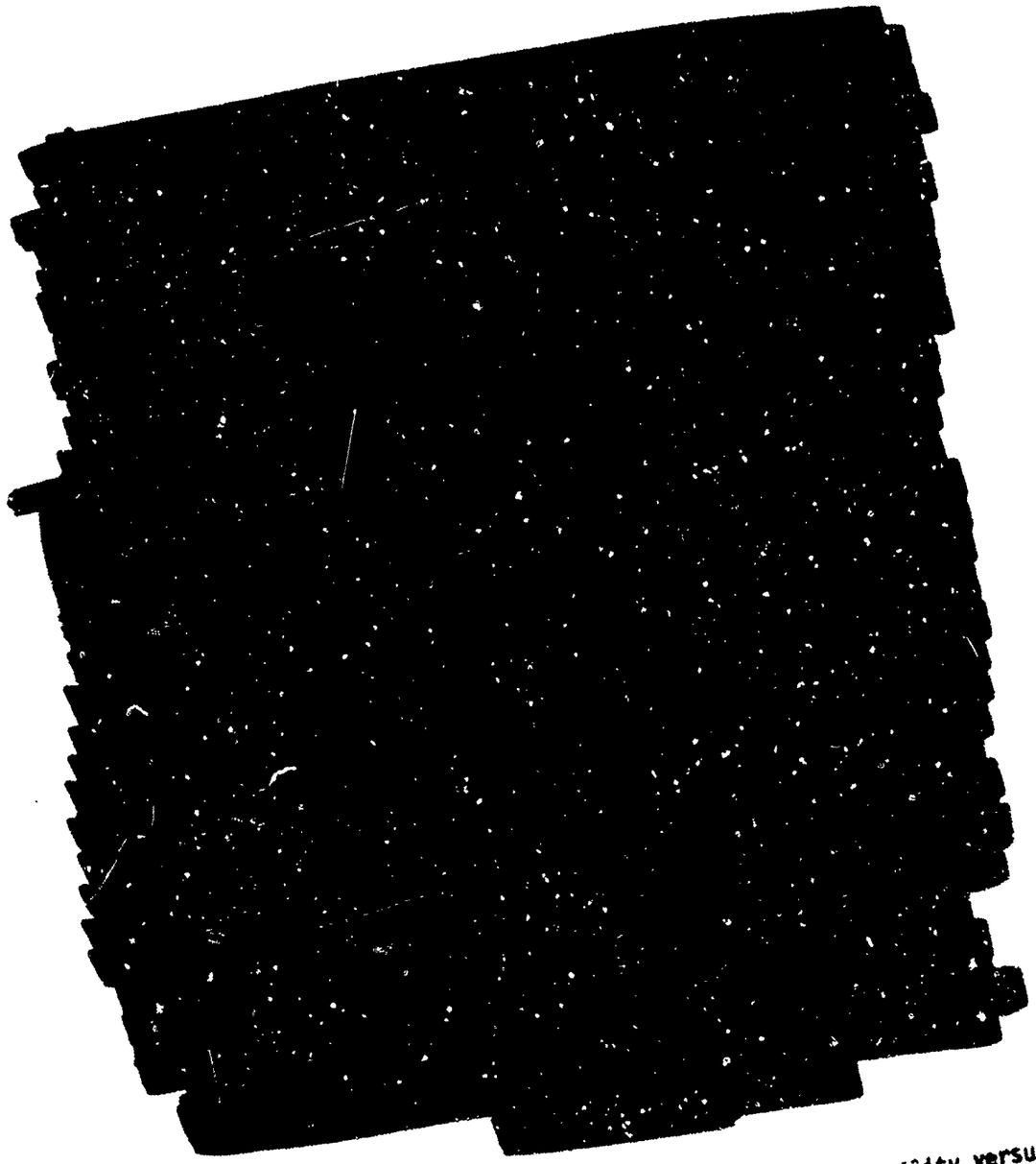

Figure 4-13. Landstuhl link: Average binary error probability versus mean C/N_0 and mean E_b/N_0.

Landstuhl. For the sake of simplicity, no uplink scintillation is considered. Two abscissa scales are shown: mean carrier power-to-noise density (C/N_o) and mean bit energy-to-noise density (E_b/N_o) for a 75 bps data rate.

These results were obtained by bit-by-bit simulations utilizing two input signal realizations at each of the four times. (Figures 3-9 to 3-12 show a portion of the first MPS realization used at each of the four times.) For each C/N_o considered, the simulation results for the two MPS cases were averaged and are shown on the figure connected by dashed lines. The vertical bars extend between the results of each of the two simulations.

[redacted]

[redacted]

DCA (b)

[redacted]

4.4 MODEM PERFORMANCE SUMMARY - SATURATED SCINTILLATION

[redacted]

DCA (b)

[redacted]

[redacted]

Figure 4-14 summarizes the results for the demodulation performance of the AN/USC-28 modem operating in a Rayleigh fading environment. Average binary error rate is shown as a function of mean carrier-power-to-noise density ratio (C/N_o) and corresponding mean bit energy-to-noise density ratio (E_b/N_o) for a 75 bps data rate. To obtain these results, bit-by-bit receiver simulations were performed using two signal realizations from the MPS calculation discussed in Section 3.2.1 as direct input to the AN/USC-28 simulation. The vertical bars on the figure show the range of the results for both realizations. The dashed line connects the vertical bars at the location of the average error rate for both signal realizations. Four values of correlation time, τ_o, of 1.0, 0.3, 0.1, and 0.03 sec are shown. These values correspond to effective velocities,* V_{eff}, of 24, 72, 240, and 720 m/sec. (The measured signal correlation length is 24 m.) Since the MPS sampling interval is 1.0 m (17 km ÷ 16384 samples), the Nyquist frequencies corresponding to the four values of τ_o given by $F_n = \frac{1}{2\Delta t}$ are 12, 34.7, 116 and 347 Hz, respectively. These values are important since previous simulations have shown the necessity of adequately sampling the input signal data to insure spectral representation out to the bandwidth of the phase-lock loop, especially when the loop is in a phase-dominated situation. Thus the bottom curve for a 1 sec signal correlation time is slightly optimistic regarding receiver performance for C/N_o values greater than 55 dB-Hz, since scintillation spectral components higher than 12 Hz are not represented in the input signal. All the other curves shown here represent adequately sampled conditions and are true estimates of the demodulator performance.

[redacted]

DCA (b)(1)

*Since the modem performance results are being summarized here in terms of fading rate or signal correlation time, the actual numerical value of V_{eff} is unimportant except as regards sampling considerations. V_{eff} as used here is simply a parameter to allow conversion from the spatial domain to the time domain.

[redacted]

[redacted]

[redacted]

[redacted]

Figure 4-14. Rayleigh fading links: Average binary error probability versus mean C/N_o and mean E_b/N_o.

DCA (6X1)

[redacted]

[redacted]

[redacted]

DCA (b)(1)

[redacted]

DCA (b)(1)

The results of Figure 4-14 for mean binary error rate in a Rayleigh environment may be considered with any of the signal correlation time contours shown in Section 3.2.2 to obtain contours of binary error rate for severe fading conditions. Given the appropriate value of C/N_o or E_b/N_o

[redacted]

the relationship between the mean binary error rate and the signal correlation time may be determined from Figure 4-14 and the contour plots of τ_o may be interpreted in terms of binary error rate. Thus, the τ_o contours within the Rayleigh footprints shown in Figures 3-14 to 3-16 and Figure 3-18 may be converted to binary error rate contours for values of E_b/N_o corresponding to specific 75 bps link configurations.

As an example, consider a (hypothetical) undisturbed uplink from an AN/FSC-78 ground terminal outside the disturbed region for the DSCS-II Atlantic satellite, then down to another AN/FSC-78 terminal stationed at Landstuhl. Assume that the narrow coverage (NC) DSCS satellite antenna is used on the uplink and that the DSCS earth coverage (EC) antenna is used on the downlink to obtain the link margin calculations shown in Table 4-2. From the table the effective link C/N_o is calculated as 68.5 dB-Hz corresponding to a value of bit energy-to-noise density of about 50 dB. Using the results in Figure 4-14 for AN/USC-28 modem performance, contours of binary error rate have been prepared and are presented in Figures 4-15 to 4-18.

Figure 4-15. Contours of binary error rate at 20 minutes. Dashed contour shows Rayleigh footprint.

Figure 4-16. Contours of binary error rate at 30 minutes. Dashed contour shows Rayleigh footprint.

DCA (b)(1)

[redacted]

Figure 4-17. Contours of binary error rate at one hour. Dashed contour shows Rayleigh footprint.

DCA (b)(1)

[redacted]

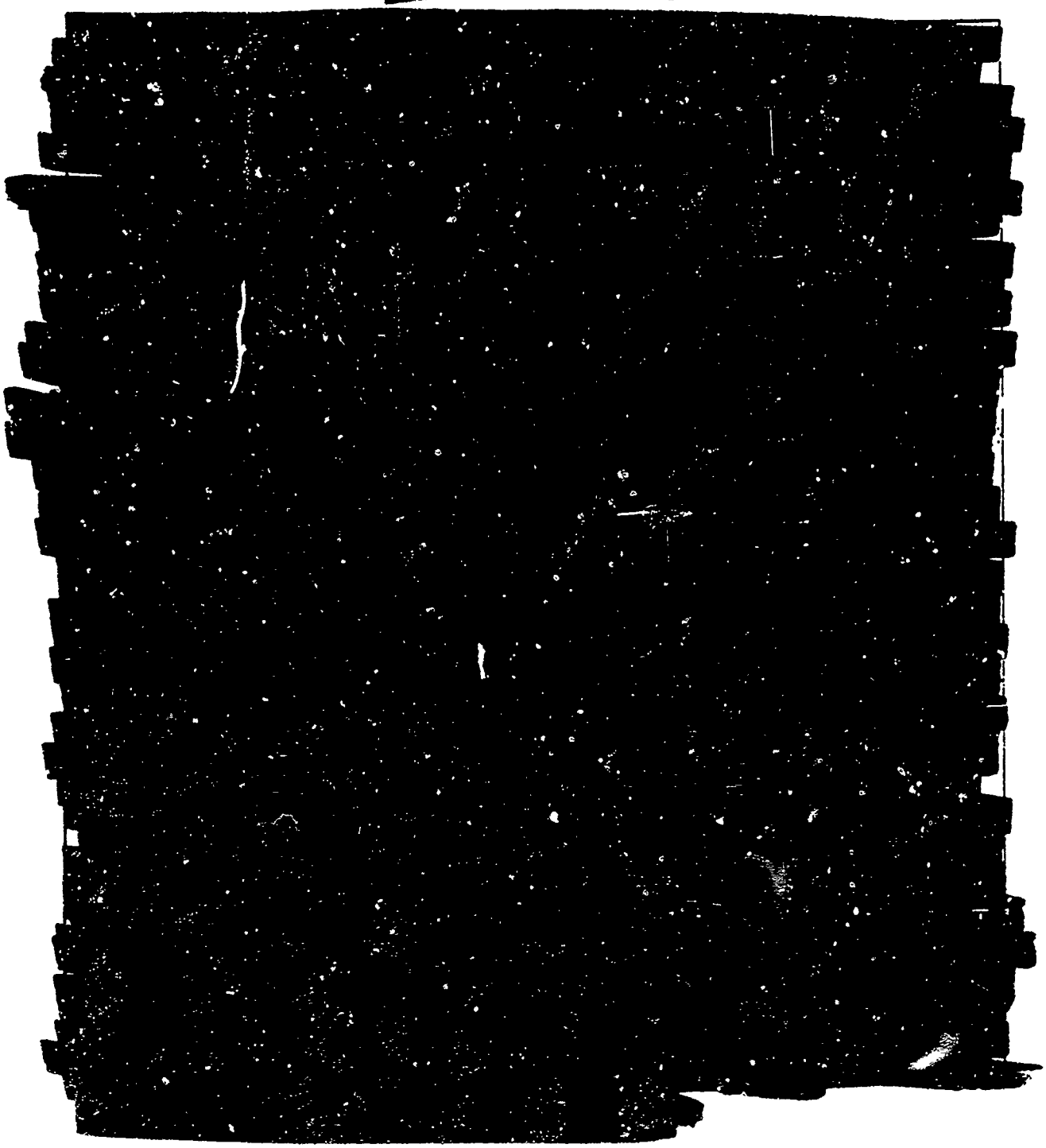

Figure 4-18. Contours of binary error rate at one hour for a fully striated plume. Dashed contour shows Rayleigh footprint.

Table 4-2. Hypothetical link calculation.

Transmitter EIRP	97	dBW (AN/FSC-78)
Receiver G/T (NC)	- 0.8	dB/°K
Free Space Loss	203	dB
Boltzmann's Constant	- 228.6	dB/°K/Hz

Uplink C/N_o = EIRP + G/T - Loss - Constant = 121.8 dB-Hz

Satellite EIRP (EC)	29.4	dB/W (20-watt TWTA)
Receiver G/T	39	dB/°K (AN/FSC-78)
Free Space Loss	202	dB
Boltzmann's Constant	- 228.6	dB/°K/Hz

Downlink C/N_o = EIRP + G/T - Loss - Constant = 95.0 dB-Hz

Assume seven other equal-power users are sharing the 50 MHz spread spectrum multiple access channels. The effective uplink C/N_o is given by:

$$\frac{1}{(C/N_o)_{eff\text{-}up}} = \frac{1}{(C/N_o)_{up}} + \frac{7}{50\times10^6} \quad \text{or}$$

$$(C/N_o)_{eff\text{-}up} = 68.5 \text{ dB-Hz}$$

Effective Link C/N_o:

$$\frac{1}{(C/N_o)} = \frac{1}{(C/N_o)_{eff\text{-}up}} + \frac{1}{(C/N_o)_{down}}$$

$$\therefore C/N_o = 68.5 \text{ dB-Hz}$$

$$E_b/N_o = 49.8 \text{ dB (75 bps)}$$

[redacted]

[redacted]

DCA (b)(1)

---

*In intense scintillation conditions signal attenuation can occur due to beamspread loss (i.e., energy scattered out of the antenna main lobe). In the dual burst scenario this loss is less than 2-3 dB for a 60 foot receiving antenna. Since the links being considered are phase scintillation dominated in intense scintillation conditions this is not an important factor in the results.

[redacted]

THIS PAGE IS INTENTIONALLY LEFT BLANK.

[redacted]

[redacted]REFERENCES

1-1. Fajen, F. E., D. H. Sowle, and D. R. Smith, Two Fluid MICE [redacted], MRC-R-71, Mission Research Corporation, May 1973 [redacted].

1-2. McDonald, B. E., "The MRHYDE Two-Fluid 3-D MHD Code [redacted]," In Proceedings of the DNA 1973 Atmospheric Effects Symposium [redacted], p. 339, DNA 3131P-7, June 1973 [redacted].

1-3. Old, T. E., Plasma Stability Analysis of a MICE Code Simulation of a High Altitude, High Yield Burst [redacted], DNA 3848T, (MRC-R-222), Mission Research Corporation, October 1975 [redacted]

1-4. Fischer, S., J. Pierre, and T. Coffey, Atmospheric Heave from a 200 km Spartan Detonation as Predicted by the NRL MRHYDE Code [redacted] Memorandum Report 3278, Naval Research Laboratory, December 1975 [redacted].

1-5. Stagat, R. W., R. W. Kilb, and R. E. Stoeckly, Field-Line-Averaged Striation Amplification After Nuclear Bursts [redacted], DNA 3837F, (MRC-R-232), Mission Research Corporation, October 1976 [redacted]

1-6. White, W. W., and F. E. Fajen, MELT: Very Late Time Nuclear Phenomenology [redacted], DNA 4067T, (MRC-R-229), Mission Research Corporation, January 1977 [redacted].

1-7. Kilb, R. W., and S. Chavin, Late-Time Striation Drift and Decay [redacted] DNA 4242T, (MRC-R-304), Mission Research Corporation, February 1977 [redacted]

1-8. Stagat, R. W., and R. W. Kilb, Striations in 3-D Single and Multiple Nuclear Bursts [redacted], DNA 4247F, (MRC-R-303), Mission Research Corporation, February 1977 [redacted]

1-9. Kilb, R. W., and S. Chavin, Striation Growth, PSD's, and Neutral Winds After a Multimegaton Burst at 200 km, DNA 4573T, (MRC-R-385), Mission Research Corporation, March 1978 [redacted].

1-10. Knepp, D. L., Multiple Phase-Screen Propagation Analysis for Defense Satellite Communications System, DNA 4424T, (MRC-R-332), Mission Research Corporation, September 1977 [redacted].

[redacted]

[redacted]

1-11. Wittwer, L. A., et al., UHF Propagation Effects in Scintillated Environments, AFWL-TR-76-304, Air Force Weapons Laboratory, August 1977 [redacted]

1-12. Defense Satellite Communications System Program/Plan 1977-1982 [redacted], Defense Communications Agency, 8 March 1976 [redacted]

1-13. Annex C to the DSCS Program/Plan 1977-1982 [redacted], Defense Communications Agency, 8 March 1976 [redacted].

1-14. System Performance Specification for the Stage 1c Phase II Defense Satellite Communications System [redacted], Defense Communications Agency, June 1975 [redacted].

1-15. Adams, B., et al., DSCS II Performance in a Nuclear Burst Propagation Environment [redacted], DNA 3632T, Computer Sciences Corporation, 19 May 1975 [redacted].

1-16. Bogusch, R. L., F. W. Guigliano, D. L. Knepp, A. H. Michelet, and B. E. Sawyer, Propagation Effects on DSCS II Links [redacted], DNA 4478T, (MRC-R-333), Mission Research Corporation, December 1977 [redacted]

1-17. Marshall, J., ESL, Incorporated, Private Communication, May 1978.

2-1. Leonard, L., W. Schlueter, J. Michael, and J. Buckner, Starfish Picture Book [redacted], Technical Report B-4299, EGG 1183-550 (2 Volumes), Prepared for the Los Alamos Scientific Laboratory by EG&G, Inc., March 1971 [redacted]

2-2. Chesnut, W. G., Spatial-Frequency Analysis of Striated Nuclear Phenomena [redacted] DNA 2575T, Stanford REsearch Institute, April 1972 [redacted]

2-3. Fajen, F. E., D. H. Sowle, and D. R. Smith, Two Fluid MICE [redacted] MRC-R-71, Mission Research Corporation, May 1973 [redacted].

2-4. McDonald, B. E., "The MRHYDE Two-Field 3-D MHD Code [redacted]," In Proceedings of the DNA 1973 Atmospheric Effects Symposium [redacted], p. 339, DNA 3131P-7, June 1973 [redacted].

2-5. Old, T. E., Plasma Stability Analysis of a MICE Code Simulation of a High Altitude, High Yield Burst [redacted] DNA 3848 T, (MRC-R-222), Mission Research Corporation, October 197[redacted].

[redacted]

[redacted]

2-6. Fisher, S., J. Pierre, and T. Coffey, Atmospheric Heave from a 200 km Spartan Detonation as Predicted by the NRL MRHYDE Code [redacted] Memorandum Report 3278, Naval Research Laboratory, December 1975[redacted].

2-7. Stagat, R. W., R. W. Kilb, and R. E. Stoeckly, Field-Line-Averaged Striation Amplification After Nuclear Bursts [redacted], DNA 3837F, (MRC-R-232), Mission Research Corporation, October 1976[redacted].

2-8. White, W. W., and F. E. Fajen, MELT: Very Late Time Nuclear Phenomenology [redacted] DNA 4067T, (MRC-R-299), Mission Research Corporation, January 1977 [redacted].

2-9. Kilb, R. W., and S. Chavin, Late-time Striation Drift and Decay [redacted] DNA 4242T, (MRC-R-304), Mission Research Corporation, February 1977 [redacted]

2-10. Stagat, R. W., and R. W. Kilb, Striations in 3-D Single and Multiple Nuclear Bursts [redacted], DNA 4247F, (MRC-R-303), Mission Research Corporation, February 1977 [redacted].

2-11. Longmire, C. L., R. W. Kilb, and W. F. Crevier, The CMHD Approach to High-Altitude Blast Waves [redacted], DNA 3313T (MRC-R-123), Mission Research Corporation, July 1974[redacted].

2-12. Kilb, R. W., and S. Chavin, Striation Growth, PSD's, and Neutral Winds After a Multimegaton Burst at 200 km [redacted], DNA 4573T, (MRC-R-385), Mission Research Corporation, March 1978[redacted].

2-13. Jordano, R. J., et. al., RANC IV, Modification 3 Revised Nuclear Phenomenology and Radar Propagation Models for RANC IV [redacted], Vol. 1, Model Formulations, DNA 3635F-1, General Electric Co., - TEMPO, January 1975[redacted].

2-14. Fajen, F. E., R. E. Stoeckly, and W. W. White, A MICE/MELT Simulation of a Multiburst Scenario [redacted], DNA 4485T (MRC-R-359), Mission Research Corporation, December 1977[redacted].

2-15. Kilb, R. W., Mission Research Corporation, Private Communication, September 1978[redacted].

[redacted]

[redacted]

3-1. Chesnut, W. G., Spatial-Frequency Analysis of Striated Nuclear Phenomena [redacted], DNA 2757T, Stanford Research Institute, April 1972 [redacted]

3-2. Dyson, P. L., J. P. McClure, and W. B. Hanson, "In Situ Measurements of the Spectral Characteristics of F Region Ionospheric Irregularities," J. Geophys. Res., Vol. 79, No. 10, pp. 1497-1502, 1 April 1974.

3-3. Phelps, A. D. R., and R. C. Sagalyn, "Plasma Density Irregularities in the High-Latitude Top Side Ionosphere," J. Geophys. Res., Vol. 81, No. 4, pp. 512-523, 1 February 1976.

3-4. Scannapieco, A. J., S. L. Ossakow, S. R. Goldman, and J. M. Pierre, "Late-Time Striation Spectra," J. Geophys. Res., Vol. 81, No. 34, pp. 6037-6045, 1 December 1976.

3-5. Briggs, B. H., and I. A. Parkin, "On the Variation of Radio Star and Satellite Scintillations with Zenith Angle," J. Atmos. Terr. Phys., Vol. 25, No. 6, pp. 339-366, 1963.

3-6. Crane, R. K., "Ionospheric Scintillation," Proc. IEEE, Vol. 65, No. 2, pp. 180-199, February 1977.

3-7. Jordano, R. J. et. al., RANC IV, Modification 3 Revised Nuclear Phenomenology and Radar Propagation Models for RANC IV [redacted], Vol. I, Model Formulations, DNA 3635F-1, General Electric Co.-TEMPO, January 1975 [redacted]

3-8. Ibaraki, R. and J. Marshall, Transatlantic Satellite Link Survivability - Propagation Path Analysis [redacted], DNA 4353T-1C, ESL, Incorporated, August 1977.

3-9. Marshall, J., ESL, Incorporated, Private Communication, September 1978 [redacted]

3-10. Knepp, D. L., Multiple Phase-Screen Propagation Analysis for Defense Satellite Communications System, DNA 4424T, (MRC-R-332), Mission Research Corporation, September 1977 [redacted]

3-11. ESL, Incorporated, ESL Presentation, 10th INCA Coordination Meeting (Section 3) [redacted], DNA-78-04323, 1978 [redacted]

3-12. Bogusch, R. L., F. W. Guigliano, D. L. Knepp, A. H. Michelet, and B. E. Sawyer, Propagation Effects on DSCS II Links [redacted], DNA 4578T, (MRC-R-333), Mission Research Corporation, December 1977 [redacted]

[redacted]

[redacted]

3-13. Hernandez, G., and R. G. Roble, "Direct Measurements of Nighttime Thermospheric Winds and Temperatures, Part 1 and 2," Journal of Geophysical Research; Part 1, Vol. 81, No. 13, pp. 2065-2074; Part 2, Vol. 81, No. 28, pp. 5173-5181, May 1, 1976.

3-14. Kilb, R. W., and S. Chavin, Late-Time Striation Drift and Decay [redacted] DNA 4242T, (MRC-R-304), Mission Research Corporation, January 1977 [redacted]

3-15. Ratcliffe, J. A., "Some Aspects of Diffraction Theory and Their Application to the Ionosphere," in Reports on Progress in Physics, Vol. 19, The Physical Society: London, England, pp. 188-267, 1956.

3-16. Tatarskii, V. I., The Effects of the Turbulent Atmosphere on Wave Propagation, IPST Catalog No. 5319, National Technical Information Service, Springfield, VA. 1971.

3-17. Abramowitz, M. and I. A. Stegun, Handbook of Mathematical Functions, Dover: New York, 1970.

3-18. Kilb, R. W., and W. R. Wortman, The Relation Between PSDs and Striation Properties [redacted] DNA 4753F, (MRC-R-425), Mission Research Corporation, November 1978 [redacted].

4-1. Bogusch, R. L., F. W. Guigliano, D. L. Knepp, A. H. Michelet, and B. E. Sawyer, Propagation Effects on DSCS II Links [redacted], DNA 4578T, (MRC-R-333), Mission Research Corporation, December 1977 [redacted]

4-2. System Performance Specification for the Stage 1c Phase II Defense Satellite Communications System [redacted], Defense Communications Agency, June 1975 [redacted]

4-3. Bogusch, R. L., M. J. Barrett, D. L. Knepp, and B. E. Sawyer, Signal Propagation Effects on Selected Satellite Systems [redacted], AFWL-TR-78-170, (MRC-R-405), Mission Research Corporation, July 197[redacted].

4-4. Bogusch, R. L., and F. W. Guigliano, DSP Link Survivability Techniques [redacted] DNA 4914F, (MRC-R-439), Mission Research Corporation, January 1979 [redacted]

[redacted]

THIS PAGE IS INTENTIONALLY LEFT BLANK.

[redacted]

DISTRIBUTION LIST

DEPARTMENT OF DEFENSE

AFSOUTH
ATTN: U.S. Documents Officer

Armed Forces Staff College
ATTN: Reference & Technical Services Branch
ATTN: Dept. of Command Control & Communications

Assistant Secretary of Defense
Comm., Cmd., Cont. & Intell.
ATTN: Surveillance & Warning Systems
ATTN: Strat. & Theater C&C System
ATTN: Assistant for NATO C3

Assistant Secretary of Defense
Program Analysis & Evaluation
ATTN: General Purpose Programs

Assistant to the Secretary of Defense
Atomic Energy
ATTN: Executive Assistant
ATTN: B. Adams

Command & Control Technical Center
ATTN: C-330
ATTN: C-650
ATTN: C-610
ATTN: C-300

Commander-in-Chief
U.S. European Command
ATTN: J-3
ATTN: ECJ-6-OJ
ATTN: J-5NPG
ATTN: J-6
ATTN: ECJ6-OP
ATTN: J-LW
ATTN: J-2-FTD
ATTN: J-2

Commander-in-Chief, Pacific
ATTN: J-2
ATTN: J-54
ATTN: J-3
ATTN: J-6

Defense Advanced Rsch. Proj. Agency
ATTN: TIO

Defense Communications Agency
ATTN: Code 530
ATTN: Code 101B
ATTN: Code 410
ATTN: Code 205
ATTN: Code 520
ATTN: Code 510
ATTN: WSE

Defense Communications Engineer Center
ATTN: Code R123
ATTN: Code R400
ATTN: Code R720

Defense Intelligence Agency
ATTN: RDS-3A
ATTN: DT-4B
6 cy ATTN: DT-1B

DEPARTMENT OF DEFENSE (Continued)

Defense Nuclear Agency
ATTN: STSS
ATTN: OASO
ATTN: STRA
ATTN: STNA
ATTN: DDST
ATTN: STSP
ATTN: VLIS
ATTN: STVL
4 cy ATTN: TITL

Defense Technical Information Center
2 cy ATTN: DD

Field Command
Defense Nuclear Agency
ATTN: FCPR
ATTN: FCP-FCPRK

Field Command
Defense Nuclear Agency
Livermore Division
ATTN: FCPRL

Interservice Nuclear Weapons School
ATTN: TTV

Joint Chiefs of Staff
ATTN: J-3, Nuclear Contingency Branch
ATTN: J-3, WWMCCS Evaluation Office
ATTN: J-3, WWMCCS Council Support Office
ATTN: J-5, Nuclear Division
ATTN: J-3, NMCC
ATTN: SAGA
ATTN: J-3

Joint Strat. Tgt. Planning Staff
ATTN: JSAS
ATTN: NRI-STINFO Library
ATTN: JLTW-2
2 cy ATTN: JL
ATTN: JPST

Joint Tactical Communications Ofc.
ATTN: TT-E-SS

National Communications System
ATTN: NCS-TS

National Security Agency
ATTN: TDL
ATTN: R 52, O. Van Gunten

Director
Net Assessment
ATTN: Military Assistants

U.S. Forces, Korea
ATTN: DJ-AM-SM
ATTN: CJ-P-E

U.S. National Military Representative
SHAPE
ATTN: U.S. Documents Officer

[redacted]

DEPARTMENT OF DEFENSE (Continued)

Undersecretary of Defense for Rsch. & Engrg.
ATTN: Strategic & Space Systems (OS)
ATTN: Research & Adv. Tech.
ATTN: Tactical Warfare Programs

DEPARTMENT OF THE ARMY

Asst. Chief of Staff for Intelligence
Department of the Army
ATTN: DAMI-FI

Atmospheric Sciences Laboratory
U.S. Army Electronics R&D Command
ATTN: DELAS-AS

Deputy Chief of Staff for Ops. & Plans
Department of the Army
ATTN: DAMO-RQC
ATTN: DAMO-ZD
ATTN: DAMO-[illegible]
ATTN: DAMO-S[illegible]

Deputy Chief of Staff for Rsch. Dev. & Acq.
Department of the Army
ATTN: Advisor for RDA Analysis (M. Gale)
ATTN: DAMA-CSS-A

Harry Diamond Laboratories
Department of the Army
ATTN: DELHD-N-P
ATTN: DELHD-N-CO
ATTN: DELHD-N-RBH
ATTN: DELHD-I-TL
ATTN: DELHD-N-RBA
2 cy ATTN: DELHD-N-EM

Multi Service Communications Systems
Department of the Army
ATTN: DRCPM-MSCS-APB, M. Francis

U.S. Army Ballistic Research Labs
ATTN: DRDAR-VL
ATTN: CAL
ATTN: TBL

U.S. Army Comb. Arms Combat Dev. Acty.
ATTN: ATCA-CO
ATTN: ATCA-CFT
ATTN: ATCA-CA

U.S. Army Comd. & General Staff College
ATTN: ATSW-TA-D

U.S. Army Comm.-Elec. Engrg. Instal. Agency
ATTN: CCC-EPEO-PED
ATTN: CCC-SEO
ATTN: CCC-PRSO

U.S. Army Communications Command
ATTN: CC-OPS-WR
ATTN: CC-OPS-SM

U.S. Army Communications Sys. Agency
ATTN: CCM-AD-LB

U.S. Army Concepts Analysis Agency
ATTN: Code 605/606

DEPARTMENT OF THE ARMY (Continued)

U.S. Army Electronics Rsch. & Dev. Command
ATTN: DRCPM-ATC
ATTN: DRCPM-TDS-SO

Commander-in-Chief
U.S. Army Europe and Seventh Army
ATTN: DCSOPS-AEAGC-O
ATTN: DCSOPS-AEAGD-MM
ATTN: DCSOPS-AEAGC-DSW
ATTN: ODCSC-E AEAGE
ATTN: DCSOPS-AEAGB

U.S. Army Materiel Sys. Analysis Activity
ATTN: DRXSY-DS
ATTN: DRXSY-S

U.S. Army Missile R&D Command
ATTN: DRSMI-YDR

U.S. Army Nuclear & Chemical Agency
ATTN: Library for MONA-WED
ATTN: Library
ATTN: Library for MONA-SAL

U.S. Army Satellite Comm. Agency
ATTN: DRCPM-SC-11
ATTN: TACSAT Office

U.S. Army TRADOC Systems Analysis Activity
ATTN: ATAA-TAC

U.S. Army Training and Doctrine Command
ATTN: ATCD-Z
ATTN: Technical Library

U.S. Army War College
ATTN: Library

V Corps
Department of the Army
ATTN: AETVGC
ATTN: AETVCE
ATTN: AETVGB

VII Corps
Department of the Army
ATTN: AETSGB-O
ATTN: AETSGC
ATTN: AETSCE

DEPARTMENT OF THE NAVY

Command & Control Programs
Department of the Navy
ATTN: OP 941

Naval Ocean Systems Center
ATTN: Research Library

Naval Surface Weapons Center
ATTN: Code F31

Office of the Chief of Naval Operations
ATTN: OP 604 E/F
ATTN: OP 94
ATTN: OP 96

This document is being sent to the below listed contractors for the use of the individuals listed. Recipient contractors are requested to validate individuals' clearances before forwarding document to same.

DEPARTMENT OF THE NAVY (Continued)

Commander-in-Chief
U.S. Atlantic Fleet
Department of the Navy
ATTN: Code J54
ATTN: Code J-611A

Commander-in-Chief
U.S. Naval Forces, Europe
ATTN: N2262, Nuclear Surety Officer

DEPARTMENT OF THE AIR FORCE

Air Force Geophysics Laboratory
ATTN: SULL

Air Force Weapons Laboratory, AFSC
ATTN: DYC
ATTN: SUL

Assistant Chief of Staff
Intelligence
Department of the Air Force
ATTN: INAK

Assistant Chief of Staff
Studies & Analyses
Department of the Air Force
ATTN: AF/SAGF
ATTN: AF/SASC

Deputy Chief of Staff
Operations Plans and Readiness
Department of the Air Force
ATTN: AFXOK
ATTN: AFXOXFM

Deputy Chief of Staff
Research, Development, & Acq.
Department of the Air Force
ATTN: AFRDQSM

Electronic Systems Division
Department of the Air Force
ATTN: XRC

Foreign Technology Division
Air Force Systems Command
ATTN: NIIS Library

Headquarters Space Division
Air Force Systems Command
ATTN: SKA

Headquarters Space Division
Air Force Systems Command
ATTN: YCPC

Strategic Air Command
Department of the Air Force
ATTN: DCXT
ATTN: XPFS
ATTN: NRT

Tactical Air Command
Department of the Air Force
ATTN: DRA

DEPARTMENT OF THE AIR FORCE (Continued)

Commander-in-Chief
U.S. Air Forces in Europe
ATTN: XPXX
ATTN: DOC

OTHER GOVERNMENT AGENCY

Central Intelligence Agency
ATTN: OSR/SEC
ATTN: OSI/LSD, R. Hart
ATTN: OSR/SF, R. Virgo

DEPARTMENT OF DEFENSE CONTRACTORS

BDM Corp.
ATTN: Corporate Library
ATTN: W. Sweeney

Boeing Co.
ATTN: R. Scheppe

66th MI Group
ATTN: RDA/Munich

Computer Sciences Corp.
ATTN: Security Officer for Library
ATTN: Security Officer for H. Blank

ESL, Inc.
ATTN: J. Marshall
ATTN: Library

General Electric Company-TEMPO
ATTN: DASIAC

General Electric Company-TEMPO
ATTN: DASIAC

Institute for Defense Analyses
ATTN: Classified Library
ATTN: D. Signori

Kaman Sciences Corp.
ATTN: W. Long

Mission Research Corp.
ATTN: F. Guigliano
ATTN: D. Knepp
5 cy ATTN: Document Control

R&D Associates
ATTN: A. Cicolani
ATTN: L. Delaney

RCA Corp.
ATTN: E. Van Keuren

SRI International
ATTN: C. Shoens
ATTN: W. Jaye

TRW Defense & Space Sys. Group
ATTN: R. Webb

TRW Defense & Space Sys. Group
ATTN: J. Dyche

This document is being sent to the below listed contractors for the use of the individuals listed. Recipient contractors are requested to validate individuals' clearances before forwarding document to same.

DEPARTMENT OF DEFENSE CONTRACTORS (Continued)

R&D Associates
ATTN: Technical Information Center
ATTN: R. Schaefer
ATTN: R. Poll
ATTN: R. Letter
ATTN: C. MacDonald